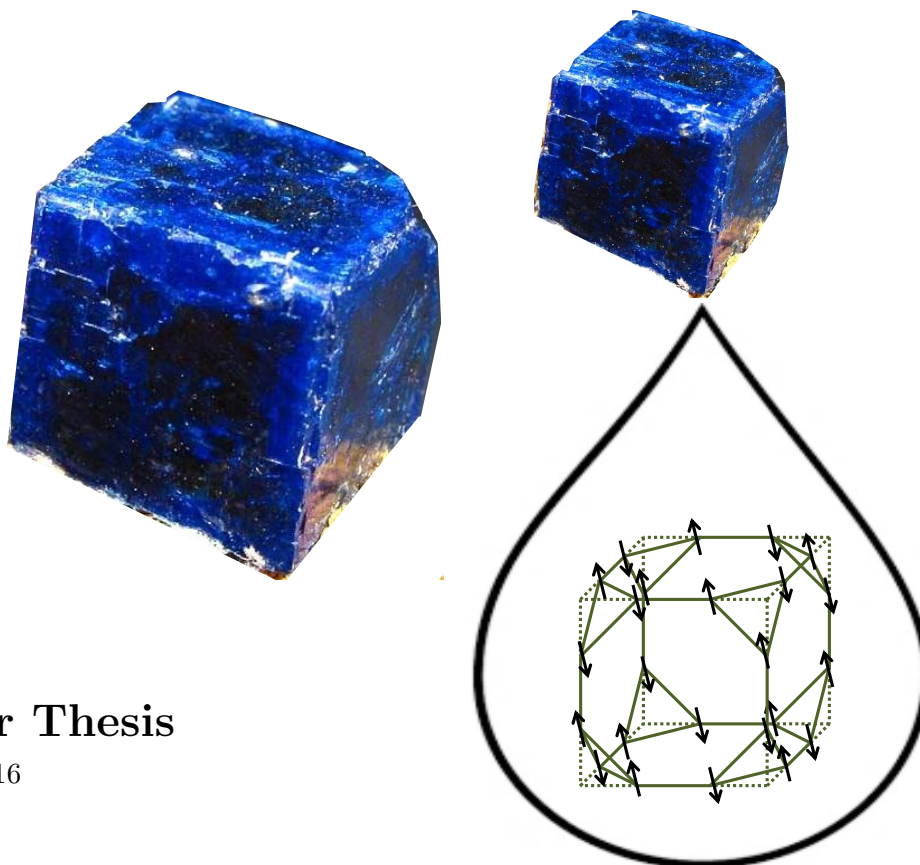




Boleite

A Quantum Spin Droplet



Master Thesis

April 8, 2016

Erik Dreier Christensen

Nano-Science Center
Niels Bohr Institute
University of Copenhagen

Supervisor:

Prof. Dr. Kim Lefmann

External collaborator:

Dr. Tom Fennell



The blue crystals on the front page are boleite crystals. The picture is taken from reference [1].

Abstract

Magnetic frustration often leads to interesting quantum mechanical phenomena, where the magnetic spins are incapable of relaxing into a unique, well ordered ground state even at 0 K. Small frustrated spin systems, like the equilateral triangle, are easily modeled, and the physics that controls them are well understood. In the extended magnetically frustrated spin lattice, exotic phenomena, like the quantum spin liquid, are theorized to exist. Quantum spin liquids are difficult to identify directly from experiments, and exact theoretical models of large frustrated systems are often difficult to make.

The natural mineral boleite ($\text{KPb}_{26}\text{Ag}_9\text{Cu}_{24}\text{Cl}_{62}(\text{OH})_{48}$) is studied in this thesis. Boleite's magnetic unit cell consists of 24 Cu^{2+} copper ions placed in a truncated cube with its corners replaced by triangles. The distance between the magnetic unit cells in boleite is so large that interaction between them can be neglected. Boleite's magnetic unit cell is therefore a possible middle ground between large frustrated magnetic systems, which may show phenomenas like quantum spin liquids, and the small solvable magnetic systems.

Boleite crystals were measured with a range of bulk experiments, and the boleite system was modeled with approximate Heisenberg spin models of the 24 spin system. The models assume a difference in exchange interaction between the magnetic ions in the triangles, J_1 , and the exchange coupling between copper ions on different triangles, J_2 . This thesis shows that it is possible to describe the magnetic susceptibility's behavior with the 24 spin model if a small paramagnetic contribution is subtracted from the raw susceptibility data. The model is best fitted to the data when $J_1 = 19.4 \pm 0.4$ meV and $J_2 = 3.4 \pm 0.1$ meV. From the model, we are able describe the magnetic structure of boleite: At temperatures of ~ 130 K, the triangles are frozen into their 4 $S = 1/2$ ground states, enabling the three spins in a triangle to collectively show paramagnetic behavior, as a sort of cooperative paramagnet. A second transition occurs near ~ 10 K where all the 8 triangles in the copper cube begin to interact and order into a unique singlet ground state.

The data shows that another type of boleite crystals exist. In this type, a suppression of the interaction between the 24 spins is seen. From estimates of the paramagnetic contribution, it is believed that this type arises due to a larger paramagnetic contribution from crystal impurities. It is in this thesis estimated that if more than 9 ± 2 % of the spins are paramagnetic, the ordering of the 24 spin system is suppressed in bulk measurements by a paramagnetic contribution.

The large amount of hydrogen in the boleite crystals prohibits us from identifying any magnetic structures in the neutron scattering signal, and our understanding of the system therefore relies solely on bulk measurements.

The Heisenberg spin models of the boleite system predicts a unique singlet ground state, and a small energy gap to a pseudo-continuum of excited states. This resembles the definition of the quantum spin liquid like behavior, called a gapped spin liquid. We therefore characterize the small 24 spin boleite system as a quantum spin droplet.

Contents

1	Introduction	1
1.1	Acknowledgments	2
2	Basic magnetism	3
2.1	The magnetic moment	3
2.2	The magnetization of solids	4
2.3	Magnetism and quantum mechanics	4
2.3.1	Hunds rule and the magnetic moment of atoms	5
2.3.2	Atoms in magnetic fields	6
2.4	Ordering of magnetic systems	8
2.4.1	Interacting spin particles	8
2.4.2	Direct exchange	10
2.4.3	Superexchange	11
3	Magnetic frustration	12
3.1	The simplest frustration - a triangle of spins	12
3.1.1	Solving the Heisenberg Hamiltonian	13
3.1.2	Solving the frustrated triangle	13
3.2	Quantum spin liquids	14
3.3	Numerical solutions - solving large spin systems	17
3.3.1	Lanczos algorithm and RLexact	17
3.3.2	Complete diagonalization	18
4	An introduction to bulk measurements	19
4.1	The magnetisation of a solid	19
4.2	The susceptibility from a solid	19
4.2.1	Curie Weiss Law	20
4.2.2	Calculating the susceptibility	21
4.3	The heat capacity of a solid	21
4.4	Bulk measurement techniques	22
4.4.1	Measuring the magnetisation and susceptibility	22
4.4.2	Measuring the heat capacity.	23
5	Introduction to Neutron Scattering	25
5.1	Properties of the neutron	25
5.2	Basic scattering	26
5.2.1	The Scattering Cross Section	26
5.2.2	The neutron as a wave	27

5.3	The nuclear neutron scattering cross section	29
5.3.1	Nuclear scattering cross section of a single crystal	29
5.3.2	Bragg's law and the Laue Condition	30
5.3.3	Bragg Peaks	31
5.4	Inelastic neutron scattering cross section	31
5.4.1	Phonon cross section	32
5.4.2	Magnetic cross section	33
5.5	Polarization analysis	35
5.6	Neutron instruments	37
5.6.1	Triple axis spectrometers	37
5.6.2	Time of flight spectrometer	38
5.6.3	The polarized neutron diffractometer	41
6	Boliete	43
6.1	Properties of boleite	43
6.1.1	Identifying proper Boleite crystals	44
6.2	The magnetic susceptibility	45
7	Modeling the susceptibility	49
7.1	Simple models	49
7.2	Mexact	51
7.3	The variational model	52
7.3.1	Variational method	52
7.3.2	Notation and basic concept	53
7.3.3	Calculation the spin 6 system	55
7.3.4	Comparison to complete diagonalization	57
7.4	The variational model and 24 spin boleite system	57
7.4.1	The result	60
7.5	Adjusting for the paramagnetic contribution	63
7.5.1	Fitting the CVT model to the adjusted data	65
7.6	The flaws of the Curie Weiss model	69
8	Other bulk experiments	71
8.1	The heat capacity	71
8.2	The magnetization as function of field	72
8.3	The AC-susceptibility.	73
9	Neutron scattering results	77
9.1	The expected magnitude of the neutron signal	77
9.2	Neutron experiments	77
9.2.1	Constructing the sample	78

9.3	The elastic structure and low energy excitations	79
9.4	Polarization analysis	81
9.4.1	Applying an external field	83
9.5	The search for high energy excitations	85
10	Discussion	87
10.1	The offset in the susceptibility data	87
10.2	The two boleite types and the paramagnetic spins	88
10.3	The neutron result	89
10.4	Boleite - A quantum spin droplet	90
11	Conclusion	92
11.1	Outlook	92
	Appendices	97
A	Complete solution to the 6 spin system	98
B	Calculating the $m = 0$ subspace	99
C	Subtracting the paramagnetic contribution.	101
D	Acoustic phonon dispersion.	104

CHAPTER 1

Introduction

Spontaneous ordering is a fundamental phenomenon in condensed matter physics, but sometimes it is when this ordering is suppressed that really interesting phenomena arise. In crystals, magnetic ordering is seen when the magnetic moments of the ions suddenly orders, for example into a so-called antiferromagnet where all magnetic moments are antiparallel to their neighbors. However, the crystal structure can sometimes prohibit such orderings in a crystal. The best example of this is in a geometrically frustrated system, where the geometry of magnetic ions results in competing interactions that suppress the magnetic ordering [2].

The physics of small magnetically frustrated quantum systems, like a antiferromagnetic triangle of spins, is well understood and can easily be modeled [3]. In large magnetically frustrated spin systems, the competing exchange interaction can give rise to exotic quantum mechanical phenomena, like the so-called quantum spin liquids. Such phenomena are difficult to measure, and numerical models are often required to properly identify them [4]. Unfortunately, it is impossible to make exact numerical models of these large systems, and so quantum spin liquids and other of such phenomena are difficult to study fully.

In this thesis, we study the natural mineral boleite ($\text{KPb}_{26}\text{Ag}_9\text{Cu}_{24}\text{Cl}_{62}(\text{OH})_{48}$). Boleite has 24 magnetic Cu^{2+} copper ions [5] placed in a truncated cube with triangles in the corners. This truncated cube forms the magnetic unit cell in boleite and is found in the center of boleite's large unit cell. The interaction between the copper ions in boleite is believed to be antiferromagnetic, and the triangles in the boleite system is thought to make boleite a magnetically frustrated system. The distance between magnetic unit cells is so large that magnetic interaction between them can be ignored, at least down to $T \sim 1.5$ K. The 24 isolated magnetic ions inside boleite's unit cell are therefore thought to be a middle ground between the small spin systems, showing discrete states which can easily be modeled, and the large spin systems with the interesting quantum phenomena.

Previous to this projects start, Kenneth Lønbæk's bachelor thesis from 2014 [6] is the only known study of the magnetism in boleite. Kenneth Lønbæk investigated the magnetic susceptibility measured from some boleite crystals and tried to model the magnetic susceptibility as a system of 6 spins forming two interacting spin triangles. The interaction between spins in the triangles was believed to be much stronger than the interaction between spins on neighboring triangles. This thesis expands the work of Kenneth Lønbæk and looks into more advanced models of the entire spin system, as well as examining the results from other experimental techniques than magnetic susceptibility.

The boleite crystals used in this project were identified and bought on Ebay by Sonja

Lindhölm. A range of experiments were carried out before the start of this project by Sonja Lindahl Holm, Kenneth Lønbæk, and others, but all neutron experiments and some of the bulk experiments have been part of this thesis project.

The major results of this thesis are in progress of being published, see reference [7].

This thesis is structured as follows. The background knowledge required to understand the work done in this thesis is presented in chapter 2 to 5. The basic background knowledge on magnetism is presented in chapter 2. In chapter 3, some of the exotic properties of large magnetically frustrated systems are presented, together with methods to numerically model large magnetic systems. Chapter 4 is devoted to a short presentation of the bulk measurement techniques used to measure *boleite*, and neutron scattering is explained in chapter 5.

In chapter 6, an introduction to the *boleite* crystal structure is given, as well as a presentation of the identification of the *boleite* crystals and magnetic susceptibility measurements. The largest part of this thesis involves the modeling of the susceptibility. An introduction to the models and the results of the models are given in chapter 7. Experimental results from other bulk techniques are presented in chapter 8, and the results from neutron experiments are presented in chapter 9. Some of the observed results from chapter 6 to 9 are discussed in chapter 10, and the final conclusions and outlook is given in chapter 11.

1.1 Acknowledgments

I would first and foremost like to thank my supervisor Kim Lefmann for letting me work with this project, and for always having time to answer my questions. A thanks is also given to Tom Fennell, who invented the project, and has shared his ideas and knowledge throughout the whole project.

The project would not have been possible without the large effort from Sonja Lindahl Holm and Kenneth Lønbæk, who did an enormous work with all the initial experimental and modeling. Sonja Lindahl Holm also deserves thanks for supervising me during the project, and for useful discussions on how to present this project.

I would also like to thank all my fellow students, and the lunch club members on the third floor of the D-building at HCØ for fruitful discussions, and needed breaks from the thesis. Especially, I would like to thank Henrik Jacobsen for helpful discussions during the writing process, and Ursula Bengaard Hansen for measuring the *boleite* crystals at the EPFL. A thanks is likewise given to all the instrument-responsible at the instruments used to measure *boleite*, their help were greatly appreciated.

Finally, I would like to thank friends and family for encouragement and support, and my girlfriend Nanna for her bearing with my distracted mind and long working days.

CHAPTER 2

Basic magnetism

The study of magnetism and magnetic materials is today a large and active scientific field. The field is driven by an interest in a wide range of topics stretching from computer hard disc drives and permanent magnets in engines and generators, to the quantum physical nature of magnetism and its link to superconductivity and quantum computing. This chapter will introduce the basic concepts of magnetism. The chapter is largely based on the first 4 chapters of Blundell [2], with some details added from other references.

2.1 The magnetic moment

Classical electrodynamics [8] tells us that a steady electric current (moving charges) will produce a magnetic field which is constant in time. A current loop will generate a magnetic field, with all field lines going through the center of the loop normal to the loop plane. In classical electrodynamics, the force that a charged particle experiences when an external magnetic and electric field is applied, is the Lorentz force

$$\mathbf{F} = q(\mathbf{E} + \mathbf{v} \times \mathbf{B}), \quad (2.1)$$

where q is the electric charge of the particle, \mathbf{E} is the electric field, \mathbf{v} is the velocity of the particle, and \mathbf{B} is the applied magnetic field. The magnetic force will try to align the magnetic field generated by the current loop with the external field. The result is that the external magnetic field will apply a torque $\boldsymbol{\tau} = \boldsymbol{\mu} \times \mathbf{B}$, where $\boldsymbol{\mu}$ is called the magnetic moment*. Any magnetic object can be described by its magnetic moment. In classical mechanics the magnetic moment $d\boldsymbol{\mu}$ is associated with a current I around an elementary (vanishingly small) oriented loop of area $|d\mathbf{A}|$ through

$$d\boldsymbol{\mu} = I d\mathbf{A}. \quad (2.2)$$

For a loop of finite size the moment can be calculated by integrating the magnetic moment across all the infinitesimal small and equal current loops which constitute the total current loop. Since all neighboring infinitesimal currents cancel, it is only the current running on the edge of the loop that contributes to the total magnetic moment

$$\boldsymbol{\mu} = \int d\boldsymbol{\mu} = I \int d\mathbf{A}. \quad (2.3)$$

*Sometimes it is called the magnetic dipole moment

The magnetic moment of an atom is proportional to its angular momentum \mathbf{L} by

$$\boldsymbol{\mu} = \gamma_g \mathbf{L}, \quad (2.4)$$

where $\gamma_g = \frac{-e}{2m_e}$ is the gyromagnetic ratio, with e and m_e being the charge and mass of the electron respectively.

The size of the magnetic moment of an atom is given in terms of the Bohr magneton μ_B . The magnitude of the Bohr magneton is defined as the absolute value of the magnetic moment of an electron in the ground state of hydrogen, so that

$$\mu_B = \frac{e\hbar}{2m_e}, \quad (2.5)$$

where \hbar is Planck's constant.

2.2 The magnetization of solids

In a magnetic solid the magnetic moment per unit volume is denoted the magnetization \mathbf{M} . In the continuum approximation one assumes that the unit volume is big enough for \mathbf{M} to be a uniform field within the solid. The magnetic field can be described by the two vector fields \mathbf{B} and \mathbf{H} , which in vacuum are related by $\mathbf{B} = \mu_0 \mathbf{H}$, with $\mu_0 = 4\pi \times 10^{-7} \text{ Hm}^{-1}$ being the permeability of free space. \mathbf{B} has the units of Tesla (T) and \mathbf{H} has the units of Ampere per meter (Am^{-1}). In a solid the relation between the two fields becomes

$$\mathbf{B} = \mu_0(\mathbf{H} + \mathbf{M}). \quad (2.6)$$

In a so-called linear material the magnetization and the \mathbf{H} -field are related through

$$\mathbf{M} = \chi \mathbf{H}, \quad (2.7)$$

where χ is a dimensionless quantity called the magnetic susceptibility.

2.3 Magnetism and quantum mechanics

It can be shown from classical statistical mechanics that the thermally averaged magnetization of a solid must be zero. This is known as the *Bohr-Van Leeuwen theorem*[†]. A conceptual explanation of the theorem is given in figure 2.1.

Real materials experience a magnetization when an external field is applied, and due to the failure of classical mechanics, quantum mechanics is needed in order to explain this. As in classical mechanics, the magnetic moment of a solid in quantum mechanics is also

[†]It was originally proposed by Niels Bohr in his doctoral dissertation from 1911 [9], but rediscovered by Van Leeuwen in 1919 [10]. It later came to be known as Bohr-Van Leeuwen theorem.

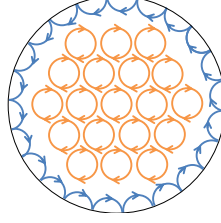


Figure 2.1: The Bohr-Van Leeuwen theorem. Classical mechanics predicts that when an external field is applied, the electrons in a bulk material will undergo cyclic motion (orange clockwise rotating arrows). On the edges, the electrons will have skipping orbits along the surface creating a counter rotating motion (counter clockwise blue arrows). It can be shown that the two contributions will exactly cancel, leaving no net magnetic moment from the material.

connected with the angular momentum of the electrons. The electron has two different types of angular momentum; the *orbital angular momentum*, related to the orbit of the electron around the nucleus of the atom, and the *spin angular momentum*. The *spin angular momentum* is a property of all particles (both elementary and composite particles) [11]. Traditionally the *spin angular momentum* of a particle is just called the *spin* of the particle.

In quantum mechanics the angular momentum is quantized in discrete steps [11]. The magnitude of the total magnetic moment of an electron's spin is in quantum mechanics given by $\mu_s = \sqrt{s(s+1)}g_s\mu_B$, and the magnetic moment along a given direction (by convention defined as \hat{z} -direction) is given by $-m_s g_s \mu_B$. $g_s \approx 2$ and is the electron's g-factor. s is the quantum number for the total spin, and m_s is the quantum number for the spin along the \hat{z} -direction. The orbital angular momentum will also contribute to the magnetic moment of the electron. Similar to the spin magnetic moment, the orbital angular momentum is described by the quantum numbers l and m_l .

The total angular momentum is the combined contribution from the spin and orbital angular momentum of the electrons and is described by the quantum number $j = l + s$.

2.3.1 Hunds rule and the magnetic moment of atoms

An atom or ion has a magnetic moment if it has non-zero angular momentum. The angular momentum is primarily determined by the electrons orbiting the nucleus. The nucleus itself also has a spin, but since the magnetic moment scales with the inverse of the mass, the heavy nucleus plays a very small part in the total angular momentum.

Electrons are spin half, $s = 1/2$, particles and thereby fermions. Two identical fermions are not allowed to be in the same quantum state, according to the *Pauli exclusion principle*

[11][‡]. The electron's quantum state can be separated into a spin state and a spatial state. When bound in an atom, the electron's spatial states are the quantized atomic shells. The electron only has two different spin states, denoted with $m_s = \pm\frac{1}{2}$, and so there is only room for two electrons in an atomic shell. In some atoms, the quantum ground state has electrons in partially filled shells. It is only the electrons in the partially filled shells that contribute to the atom's total angular momentum, and therefore it is only atoms with partially filled shells in the atomic ground state which are magnetic.

The sum of the combined orbital angular momentum \mathbf{L} (quantum numbers L and m_L) and spin \mathbf{S} (quantum numbers S and m_S) of all electrons in unfilled spatial states, will give the total angular momentum $\mathbf{J} = \mathbf{L} + \mathbf{S}$. \mathbf{L} and \mathbf{S} are coupled to each other through the spin-orbit interaction. The spin-orbit interaction affect the quantum states and will split them into a number of different energy levels, which are labeled using the quantum numbers of \mathbf{J} , J and m_J . J takes values from $|L - S|$ to $|L + S|$. Each energy level has a degeneracy of $2J + 1$, where each state is labeled by m_J , which takes the value $-J$ to J . The ground state of an atom with a large number of electrons and a net angular momentum can be determined by the help of Hund's rules for partially filled shells:

- Maximize S . To minimize the Coulomb repulsion[§] between the electrons by taking advantage of the Pauli exclusion principle that prohibits electrons with the same spin state to be in the same spatial state.
- Maximize L . To minimize the Coulomb repulsion by making the electrons rotate in the same direction, and thereby minimize the time there the electrons are in proximity of each other.
- If the shell is less than half full $J = |L - S|$, and if the shell is more than half full $J = |L + S|$. This rule is made in an attempt to minimize the spin orbit energy, and it only applies when the spin orbit interaction energy is large compared to other effects, like for example the crystal field energy.

Hund's rules are empirical rules, and many systems do not behave as the Hund's rules predict they should.

2.3.2 Atoms in magnetic fields

When applying a magnetic field to an atom, it will be more favorable for the electron's spin to point along the magnetic field than against it. The atom's energy levels are split by an energy ΔE_z from the zero field energy. The effect is called the *Zeeman splitting*,

[‡]Pauli was in 1945 awarded the Nobel Prize in Physics for the discovery that two electrons could not have the same quantum state [12].

[§]Electrostatic repulsion between particles with the same charge sign.

and is given by

$$\Delta E_z = g_J \mu_B m_S B, \quad (2.8)$$

where m_S is the spin moment along the $\hat{\mathbf{z}}$ -direction of the atomic state. g_J is the Landé g-factor, which can be calculated from

$$g_J = g_L \frac{J(J+1) - S(S+1) + L(L+1)}{2J(J+1)} + g_S \frac{J(J+1) + S(S+1) - L(L+1)}{2J(J+1)}, \quad (2.9)$$

where g_S and g_L are the spin and orbital momentum g-factors. For $L = 0$ and $S = 1/2$, $g_J = g_S \approx 2$.

The orbital angular momentum also plays an important role for atoms in an external magnetic field. To explain the effect, I will first consider isolated magnetic ions. The behavior of a single atom in zero field is described by the Hamiltonian

$$\hat{\mathcal{H}}_0 = \sum_i^Z \left(\frac{p_i^2}{2m_e} + V_i \right), \quad (2.10)$$

which is the sum of the kinetic energy $\frac{p_i^2}{2m_e}$, and the potential energy V_i , of the i 'th electron, summed across all electrons in an atom Z .

If the external B -field is small enough, it can be treated as a perturbation to the original Hamiltonian $\hat{\mathcal{H}}_0$, and it can be shown that [2]

$$\hat{\mathcal{H}} = \hat{\mathcal{H}}_0 + \mu_B (\mathbf{L} + g\mathbf{S}) \cdot \mathbf{B} + \frac{e^2}{8m_e} \sum_i^Z (\mathbf{B} \times \mathbf{r}_i)^2. \quad (2.11)$$

The first perturbation term $\mu_B (\mathbf{L} + g\mathbf{S}) \cdot \mathbf{B}$ is called the paramagnetic term, and the second perturbation term $\frac{e^2}{8m_e} \sum_i^Z (\mathbf{B} \times \mathbf{r}_i)^2$ is the diamagnetic term. Of these two, the paramagnetic term is usually the largest.

The paramagnetic term describes the energy gain of an atom by aligning its total magnetic moment with an external field. Paramagnetism only exists when the atom has a net angular momentum, since it depends on \mathbf{L} and \mathbf{S} . In a solid filled with non coupled ions with unfilled shells, the paramagnetism will create a positive magnetization along the external magnetic field.

If there are no unfilled shells, the diamagnetic term begins to play a part. Diamagnetism is a purely quantum mechanical phenomena, where the external magnetic field generates a magnetic moment that points against the external field. Diamagnetism will not be explained further in this thesis.

According to equation (2.7), it is the susceptibility that determines the sign of magnetization when applying a magnetic field. So if a material is paramagnetic, $\chi > 0$ since the magnetisation is pointing along the external field. A diamagnetic material will have $\chi < 0$. A paramagnetic material will have $\chi \propto \frac{1}{T}$, in the limit $\mu_B B \ll k_B T$, where k_B is the Boltzmann constant.

2.4 Ordering of magnetic systems

For many magnetic solids there will be a coupling between the magnetic ions, which creates a long range ordering of the magnetic moment even without any applied field. In most cases long range order occurs when a material contains 3d transition metals or 4f lanthanides. Of these two, the transition metals are particular easy to work with, since often $L = 0$ due to crystal fields (quenching), and thereby $J = S$.

The simplest explanation of interaction between magnetic moments of the transition metals is the so called dipole-dipole interaction. Dipole-dipole interaction describes the effect seen when the field created by one magnetic dipole affects another magnetic dipole. The energy of two magnetic dipoles $\boldsymbol{\mu}_1$ and $\boldsymbol{\mu}_2$ separated by \mathbf{r} is

$$E = \frac{\mu_0}{4\pi r^3} \left(\boldsymbol{\mu}_1 \cdot \boldsymbol{\mu}_2 - \frac{3}{r^2} (\boldsymbol{\mu}_1 \cdot \mathbf{r})(\boldsymbol{\mu}_2 \cdot \mathbf{r}) \right). \quad (2.12)$$

The magnetic ions in a solid are usually separated by more than 1 Å, and so the dipole energy between two magnetic ions is typically smaller than 10^{-1} meV. This corresponds to the thermal energy at temperatures of around 1 K. This means that long range order at high T is typically not due to dipole-dipole interaction.

2.4.1 Interacting spin particles

The typical origin of long range magnetic order is exchange interactions. Since electrons are fermions, the combined spatial and spin state needs to be antisymmetric under exchange (Pauli exclusion principle). In order for the combined state to be antisymmetric, the spatial state needs to be symmetric while the spin state is antisymmetric, or vice versa. The antisymmetric spin state is called the singlet state χ_S , and the symmetric is called the triplet state χ_T . This means that for two electrons there are two possible state configurations

$$\begin{aligned} \Psi_S &= \frac{1}{\sqrt{2}} [\psi_a(\mathbf{r}_1)\psi_b(\mathbf{r}_2) + \psi_a(\mathbf{r}_2)\psi_b(\mathbf{r}_1)] \chi_S \\ \Psi_T &= \frac{1}{\sqrt{2}} [\psi_a(\mathbf{r}_1)\psi_b(\mathbf{r}_2) - \psi_a(\mathbf{r}_2)\psi_b(\mathbf{r}_1)] \chi_T. \end{aligned} \quad (2.13)$$

We will define the difference between the energy of the triplet state E_T and the singlet state E_S as the exchange constant J [¶]. Using this definition, it can be shown that

$$J = E_T - E_S = -2 \int \psi_a^*(\mathbf{r}_1)\psi_b^*(\mathbf{r}_2)\hat{\mathcal{H}}\psi_a(\mathbf{r}_2)\psi_b(\mathbf{r}_1)d\mathbf{r}_1d\mathbf{r}_2. \quad (2.14)$$

Two coupled spins, called a spin dimer, can be parametrized using the spin operators $\hat{\mathbf{S}}_1 \cdot \hat{\mathbf{S}}_2$, such that $\hat{\mathcal{H}}_s\chi_S = E_S\chi_S$ and $\hat{\mathcal{H}}_s\chi_T = E_T\chi_T$, where

$$\hat{\mathcal{H}}_s = J\hat{\mathbf{S}}_1 \cdot \hat{\mathbf{S}}_2. \quad (2.15)$$

[¶]Sometimes J is called the exchange integral.

Eigenstates	S	m_S	Energy	
$ \uparrow\uparrow\rangle$	1	1	$\frac{1}{4}J$	The triplet χ_T
$\frac{ \downarrow\uparrow\rangle + \uparrow\downarrow\rangle}{\sqrt{2}}$	1	0	$\frac{1}{4}J$	
$ \downarrow\downarrow\rangle$	1	-1	$\frac{1}{4}J$	
$\frac{ \downarrow\uparrow\rangle - \uparrow\downarrow\rangle}{\sqrt{2}}$	0	0	$-\frac{3}{4}J$	The singlet χ_S

Table 2.1: The eigenstates and energies of $\hat{\mathcal{H}}_s$ (equation (2.15)), for $S = 1/2$ spins. S is the total spin magnitude and m_S is the spin along the z-direction of the eigenstate.

The spin operator $\hat{\mathbf{S}}_i$ can be separated into its $\hat{\mathbf{x}}$, $\hat{\mathbf{y}}$, and $\hat{\mathbf{z}}$ components, so that $\hat{\mathbf{S}}_i = \hat{\mathbf{x}}\hat{S}_i^x + \hat{\mathbf{y}}\hat{S}_i^y + \hat{\mathbf{z}}\hat{S}_i^z$. The spins are typically quantized along the $\hat{\mathbf{z}}$ direction, and so

$$\begin{aligned}\hat{S}_i^y &= \frac{1}{2i}(\hat{S}_i^+ - \hat{S}_i^-), \\ \hat{S}_i^x &= \frac{1}{2}(\hat{S}_i^+ + \hat{S}_i^-),\end{aligned}\tag{2.16}$$

where \hat{S}_i^+ and \hat{S}_i^- are the raising and lowering operators. For a $S = 1/2$ spin

$$\begin{aligned}\hat{S}^z|\uparrow\rangle &= \frac{1}{2}|\uparrow\rangle & \hat{S}^+|\uparrow\rangle &= 0, & \hat{S}^-|\uparrow\rangle &= |\downarrow\rangle \\ \hat{S}^z|\downarrow\rangle &= -\frac{1}{2}|\downarrow\rangle & \hat{S}^+|\downarrow\rangle &= |\uparrow\rangle & \hat{S}^-|\downarrow\rangle &= 0,\end{aligned}\tag{2.17}$$

where $|\uparrow\rangle$ is the $m_S = 1/2$ spin state, and $|\downarrow\rangle$ is the $m_S = -1/2$ spin state.

A $S = 1/2$ spin dimer intuitively generates 4 different configurations of the spins. The 4 configuration can be written $|\uparrow\uparrow\rangle$, $|\downarrow\downarrow\rangle$, $|\uparrow\downarrow\rangle$, and $|\downarrow\uparrow\rangle$, where \uparrow labels that the spin is in its $m_S = 1/2$ state, and \downarrow labels that the spin is in its $m_S = -1/2$ state. These intuitive states, where the spins are quantized along the $\hat{\mathbf{z}}$ -direction, are also called the Ising basis. The Ising basis states are not all eigenstates of the $\hat{\mathcal{H}}_s$, but the eigenstates can be written as linear combinations of the Ising basis states.

By solving the Hamiltonian from equation (2.15) for $S = 1/2$, one finds that these 4 eigenstates will separate into two energy levels, a singlet state, where the spin anti align, and a 3 times degenerate triplet state, where the spins align. The full solution is shown in table 2.1. From the table it can be seen that it is J that determines whether it is the singlet or the triplet that is the ground state.

When the system becomes larger than 2 atoms, and an external magnetic field is applied, equation (2.15) can be extended to

$$\hat{\mathcal{H}} = \frac{1}{2} \sum_{i,j} J_{ij} \hat{\mathbf{S}}_i \cdot \hat{\mathbf{S}}_j + g\mu_B \mathbf{B} \cdot \sum_i \hat{\mathbf{S}}_i.\tag{2.18}$$

This Hamiltonian is called the Heisenberg Hamiltonian. The factor $\frac{1}{2}$ is introduced to account for double counting of neighbors.

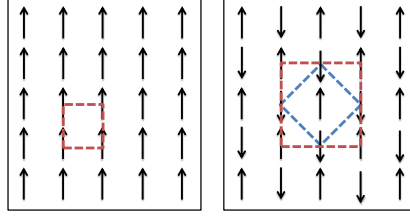


Figure 2.2: Ferromagnetic (**left**) and antiferromagnetic (**right**) ordering. The square magnetic unit cells are marked with dashed red lines. The primitive unit cell for the antiferromagnetic ordering is marked with a dashed blue line. Notice that the antiferromagnetic square unit cell has twice as large distance between the corners as the ferromagnetic.

The Heisenberg Hamiltonian $\hat{\mathcal{H}}$, from equation (2.18), is the sum of a spin interaction term $\hat{\mathcal{H}}_I$, and a Zeeman term $\hat{\mathcal{H}}_Z$ that accounts for the effect of an external magnetic field. When the magnetic field \mathbf{B} is applied along the $\hat{\mathbf{z}}$ -direction, $\hat{\mathcal{H}}_I$ and $\hat{\mathcal{H}}_Z$ can be written in terms of \hat{S}_i^z , \hat{S}_i^+ and \hat{S}_i^- :

$$\hat{\mathcal{H}}_I = \frac{1}{2} \sum_{i,j} J_{i,j} \hat{\mathbf{S}}_i \cdot \hat{\mathbf{S}}_j = \frac{1}{2} \sum_{i,j} J_{i,j} \hat{S}_i^z \hat{S}_j^z + \frac{J_1}{2} (\hat{S}_i^+ \hat{S}_j^- + \hat{S}_i^- \hat{S}_j^+), \quad (2.19)$$

$$\hat{\mathcal{H}}_Z = g\mu_B \mathbf{B} \cdot \sum_i \hat{\mathbf{S}}_i = g\mu_B B \sum_i \hat{S}_i^z. \quad (2.20)$$

There are a variety of different types of ordering of the spins in large spin systems. The two most simple types of ordering are where all spins align, called *ferromagnetism*, and where all spins anti-align, called *antiferromagnetism*. These two types of ordering are illustrated in figure 2.2. In a system where the Heisenberg Hamiltonian (equation (2.18)) applies, the exchange constant $J_{i,j}$ determines, which type of ordering that will occur.

For $J_{i,j} < 0$, it is favorable for the spin to be parallel, and so it results in ferromagnetic ordering. Due to the many-body behavior of large systems, the overall spin ground state with $J_{i,j} > 0$ is not easily determined. In transition metal oxides, where $J_{i,j} > 0$, the quantum ground state is typically antiferromagnetic, but system with different ions and configurations can have more exotic $J_{i,j} > 0$ ground states. A detailed calculation of the ground state of systems with $J_{i,j} > 0$ can be found in Yosida [13].

I will in the following sections show two different types of exchange interaction between transition metals.

2.4.2 Direct exchange

Direct exchange happens when the transition metals in a solid are close enough for the magnetic orbitals to overlap. When two orbitals overlap, it is energetically favorable for the atoms to form a bond. The bond creates what is called a molecular orbital, where the electrons can either have an anti-symmetric or symmetric spatial state as long as

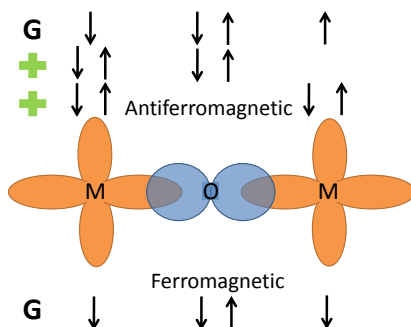


Figure 2.3: Superexchange in a magnetic oxide with 4 free electrons. The electrons are allowed to jump between the overlapping orbitals (colored ellipses) of the 2 transition metals (M) and the single oxygen (O). If the transition metals are antiferromagnetically coupled, it is possible for electrons (arrows showing spin) to jump between orbitals, by mixing the ground state (top G) with the excited states (green pluses). Due to the Pauli exclusion principle, ferromagnetic ordered electrons have to stay in their ground state (bottom G). Delocalization of the electrons across the entire M-O-M system lowers the kinetic energy, and so the antiferromagnetic configuration is energetically favorable.

the spin states ensure that the combined state is anti-symmetric under exchange. I will call the anti-symmetric state of the molecular orbital for the anti-bonding state, and the symmetric for the bonding state. It can be shown that the kinetic energy of the electrons in anti-bonding state is higher than that of the bonding state, and the bonding state is thereby most likely the ground state. This means that direct exchange often leads to an antiferromagnetic ordering since the bonding state has an anti-symmetric spin state. Direct exchange is unlikely to happen between most magnetic ions, since their magnetic orbitals are too localized compared to the distance between them, which makes an overlap between the orbitals very small.

2.4.3 Superexchange

When the distance between the transition metals is too large to form direct exchange bonds, they can bond through super exchange pathways, where the electrons can travel between transition metals through non-magnetic ions. An example is the Copper-ion's 3d orbital, which overlaps with the Oxygen-ion's 2p orbital. Depending on the geometry of the system, a strong antiferromagnetic coupling can be formed between the copper ions. The antiferromagnetic coupling will in this case allow the electrons to be further delocalized, by allowing them to be present on both copper and oxygen states. Superexchange between two transition metals through a single oxygen is illustrated in figure 2.3.

CHAPTER 3

Magnetic frustration

Magnetic frustration occurs in materials where competing exchange interaction between spins can not be simultaneously satisfied. The physical field of magnetic frustration has been of large interest for some time due to the interesting nature of its exotic quantum physical phenomenas, and the proposed connection between magnetically frustrated states and superconductivity states in doped La_2CuO_4 [15]. This chapter will introduce the concept of magnetic frustration and different ways of solving the Hamiltonian of large spin systems.

3.1 The simplest frustration - a triangle of spins

The simplest example of a system with magnetic frustration is an equilateral antiferromagnetic triangle of spins. If S is large, classical fluctuation will dominate a spin system. The equilateral antiferromagnetic triangle has multiple classical ground states, which enable the spins to reorient randomly between the states. As the thermal energy is lowered, the fluctuation will cease since the energy barrier between the ground states becomes too large, and the spins order into one of the ground states. Quantum fluctuations dominate for $S = 1/2$ spin systems. The quantized $S = 1/2$ spins can either point up ($m_S = 1/2$) or down ($m_S = -1/2$). In the equilateral antiferromagnetic $S = 1/2$ spin triangle, the quantum spins will not be able to point opposite to both their neighbors, and so a degenerate ground state arise. The degeneracy of the ground state cause the quantum spin triangle to be frustrated, since spin fluctuations are possible even at $T = 0$ K. Illustrations of the classical and quantum spin triangle can be seen in figure 3.1.

The $S = 1/2$ triangle system has $(2S + 1)^3 = 8$ different quantum states. To see how the exact eigenstates of the magnetic triangle look, the Heisenberg Hamiltonian $\hat{\mathcal{H}}$, from equation (2.18), needs to be solved.

The matrix elements of $\hat{\mathcal{H}}$ are $\hat{\mathcal{H}}_{i,j} = \langle \chi_i | \hat{\mathcal{H}} | \chi_j \rangle$, where $\hat{\mathcal{H}}_{i,j}$ is the i, j matrix element and χ_i is the i 'th basis state. Since there for the spin triangle are 8 basis states an (8×8) matrix needs to be diagonalized.



Figure 3.1: A geometrically frustrated antiferromagnetically coupled triangle. (a) Example of a classical ground state, where the three spins are turned 120 degrees compared to each other. (b) Example of quantum frustration. All three spins are not able to be antiparallel, and therefore frustration occurs.

3.1.1 Solving the Heisenberg Hamiltonian

To find the eigenvalues of an (8×8) matrix, $8^2 = 64$ matrix elements need to be calculated, and afterwards the full matrix needs to be diagonalized. Diagonalizing an (8×8) can easily be done using computational routines, but never the less, it is useful to introduce the concept of block diagonalization, as it is a necessity when solving large spin systems. $\hat{\mathcal{H}}_I$ and $\hat{\mathcal{H}}_Z$, from equation (2.19) and (2.20), do not affect the total magnetization of a state along the $\hat{\mathbf{z}}$ -direction m_S , since \hat{S}_j^z , and pairs like $\hat{S}_i^+ \hat{S}_j^-$ can not change m_S . The Ising basis consists of spins quantized along the z -direction, and so $\langle \chi_i | \hat{\mathcal{H}} | \chi_j \rangle = 0$ if the Ising states $|\chi_j\rangle$ and $|\chi_i\rangle$ do not have the same total magnetization. It is therefore possible to separate the Hamiltonian into m -subspaces, and diagonalize them separately. This is called block diagonalization, and we call m_S a good quantum number as it can be used to block diagonalize the Heisenberg Hamiltonian.

Other good quantum numbers exist, and they can be used to further block diagonalize the m_S -subspaces. An example is the use of geometrical symmetries in a spin system. Further details of other ways of using block diagonalization is outside the scope of this thesis.

For a $S = 1/2$ system with N spins, there are $N + 1$ different values of m_S , with m_S taking the values $m = -N/2, -N/2 + 1, \dots, N/2 - 1, N/2$. The Ising states are combinations of spins pointing up or down, and so the number of different states with a given m_S are given by the binomial coefficient $\binom{N}{U} = \frac{N!}{U!(N-U)!}$, where U is the number of spins pointing up.

$\hat{\mathcal{H}}_Z$ is independent of how the spins are arranged individually, since it is only dependent on the quantum states' total magnetization $m = \sum_i \hat{S}_i^z$. One can therefore write $\hat{\mathcal{H}}|\chi_i\rangle = E|\chi_i\rangle$, where $|\chi_i\rangle$ is both the eigenstate of $\hat{\mathcal{H}}$ and $\hat{\mathcal{H}}_I$, and $E = E_I + \Delta E_Z$. E_I is the eigenenergy of $\hat{\mathcal{H}}_I$, and ΔE_Z is the Zeeman splitting of the eigenenergies given by $\Delta E_Z = g\mu_B B m$. The implication of this is that in order to solve $\hat{\mathcal{H}}$, only the eigenstates of $\hat{\mathcal{H}}_I$ needs to be found, and ΔE_Z can then afterwards be added to E_I .

$\hat{\mathcal{H}}_I$ has no preferred spatial direction and so $\hat{\mathcal{H}}_I$ must be symmetric around $m = 0$. This is called time reversal symmetry, and as a result subspaces with equal $|m_s|$ will have identical solutions. This can be used to almost half the amount of subspaces that need to be solved.

3.1.2 Solving the frustrated triangle

3 coupled spins will, as already mentioned, have 8 different Ising states. The first two states are all spins down $|\downarrow\downarrow\downarrow\rangle$ with magnetization $m_S = -3/2$, and all spins up $|\uparrow\uparrow\uparrow\rangle$ with $m_S = +3/2$. One of the spins for both of these two states can be flipped, which in total gives 6 more states

$$\begin{aligned} m = -1/2: \quad & |1, \downarrow\rangle = |\uparrow\downarrow\downarrow\rangle, \quad |2, \downarrow\rangle = |\downarrow\uparrow\downarrow\rangle, \quad \text{and} \quad |3, \downarrow\rangle = |\downarrow\downarrow\uparrow\rangle, \\ m = +1/2: \quad & |1, \uparrow\rangle = |\downarrow\uparrow\uparrow\rangle, \quad |2, \uparrow\rangle = |\uparrow\downarrow\uparrow\rangle, \quad \text{and} \quad |3, \uparrow\rangle = |\uparrow\uparrow\downarrow\rangle. \end{aligned} \quad (3.1)$$

Eigenstates	S	m_S	Energy	
$ \uparrow\uparrow\uparrow\rangle$	$\frac{3}{2}$	$-\frac{3}{2}$	$\frac{3}{4}J_1$	} Quadruplet
$\frac{1}{\sqrt{3}}(1,\downarrow\rangle + 2,\downarrow\rangle + 3,\downarrow\rangle)$	$\frac{3}{2}$	$-\frac{1}{2}$	$\frac{3}{4}J_1$	
$\frac{1}{\sqrt{3}}(1,\uparrow\rangle + 2,\uparrow\rangle + 3,\uparrow\rangle)$	$\frac{3}{2}$	$\frac{1}{2}$	$\frac{3}{4}J_1$	
$ \downarrow\downarrow\downarrow\rangle$	$\frac{3}{2}$	$\frac{3}{2}$	$\frac{3}{4}J_1$	
$\frac{1}{\sqrt{3}}(1,\downarrow\rangle + e^- 2,\downarrow\rangle + e^+ 3,\downarrow\rangle)$	$\frac{1}{2}$	$-\frac{1}{2}$	$-\frac{3}{4}J_1$	} Doublet
$\frac{1}{\sqrt{3}}(1,\uparrow\rangle + e^- 2,\uparrow\rangle + e^+ 3,\uparrow\rangle)$	$\frac{1}{2}$	$\frac{1}{2}$	$-\frac{3}{4}J_1$	
$\frac{1}{\sqrt{3}}(1,\downarrow\rangle + e^+ 2,\downarrow\rangle + e^- 3,\downarrow\rangle)$	$\frac{1}{2}$	$-\frac{1}{2}$	$-\frac{3}{4}J_1$	} Doublet
$\frac{1}{\sqrt{3}}(1,\uparrow\rangle + e^+ 2,\uparrow\rangle + e^- 3,\uparrow\rangle)$	$\frac{1}{2}$	$\frac{1}{2}$	$-\frac{3}{4}J_1$	

Table 3.1: The eigenstates and energies of the Hamiltonian from equation (2.19) in the triangle system. The complex phases are $e^+ = e^{i\frac{3\pi}{2}}$ and $e^- = e^{-i\frac{3\pi}{2}}$.

$\hat{\mathcal{H}}_I$, from equation (2.19), can now be block diagonalized. For simplicity, I define that all $J_{i,j} = J_1$, and so $\hat{\mathcal{H}}_I|\uparrow\uparrow\uparrow\rangle = \frac{3}{4}J_1|\uparrow\uparrow\uparrow\rangle$, and hence $|\uparrow\uparrow\uparrow\rangle$ is an eigenstate of $\hat{\mathcal{H}}_I$ with energy $\frac{3}{4}J_1$. Due to time reversal symmetry $|\downarrow\downarrow\downarrow\rangle$ must also be an eigenstate of $\hat{\mathcal{H}}_I$ with energy $\frac{3}{4}J_1$.

To get the energies and eigenstates for the $|m_S| = 1/2$ subspaces, the following matrix needs to be solved

$$\hat{\mathcal{H}}_I(m = \frac{1}{2}) = \begin{pmatrix} \langle 1,\uparrow|\hat{\mathcal{H}}_I|1,\uparrow\rangle & \langle 1,\uparrow|\hat{\mathcal{H}}_I|2,\uparrow\rangle & \langle 1,\uparrow|\hat{\mathcal{H}}_I|3,\uparrow\rangle \\ \langle 2,\uparrow|\hat{\mathcal{H}}_I|1,\uparrow\rangle & \langle 2,\uparrow|\hat{\mathcal{H}}_I|2,\uparrow\rangle & \langle 2,\uparrow|\hat{\mathcal{H}}_I|3,\uparrow\rangle \\ \langle 3,\uparrow|\hat{\mathcal{H}}_I|1,\uparrow\rangle & \langle 3,\uparrow|\hat{\mathcal{H}}_I|2,\uparrow\rangle & \langle 3,\uparrow|\hat{\mathcal{H}}_I|3,\uparrow\rangle \end{pmatrix} = J_1 \begin{pmatrix} -1/4 & 1/2 & 1/2 \\ 1/2 & -1/4 & 1/2 \\ 1/2 & 1/2 & -1/4 \end{pmatrix}. \quad (3.2)$$

The above matrix has 2 eigenstates with energy $-\frac{3}{4}J_1$ and one eigenstate with energy $\frac{3}{4}J_1$. One way of representing the degenerate ground states to the $|m_S| = 1/2$ subspaces is with the two complex phases shown in table 3.1. Another way of representing the ground states can be seen in reference [3].

If the triangle spins are antiferromagnetically coupled ($J_1 > 0$) the system will have a 4 times degenerate groundstate consisting of two degenerate doublets, with an energy gap of $\frac{3}{2}J_1$ to the excited quadruplet. If a magnetic field is applied the Zeeman splitting, depending on m_S , will split the ground states in two levels, and the excited quadruplet in four.

3.2 Quantum spin liquids

The following section is based on the review of Quantum Spin Liquids (QSL) in reference [4].

The ground state of the triangle system is highly degenerate with 4 different ground states, as shown above. At low temperatures, the magnetic spins of the triangle will therefore

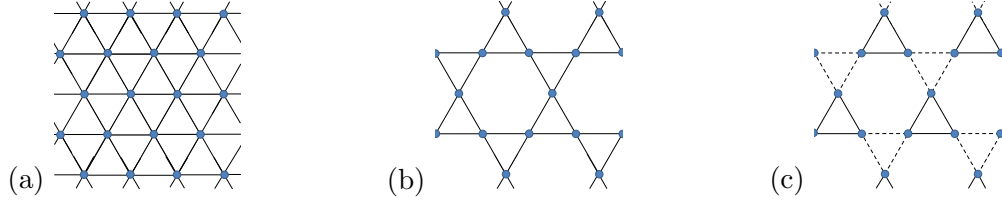


Figure 3.2: 2D projection of lattices that in real systems have been shown to host QSL like behavior. The blue circles represents the spin position and the lines between them represents the exchange interaction. (a) shows the triangular lattice and (b) Shows the kagomé lattice. (c) Shows the hyperkagomé lattice, which has two different coupling strengths between neighboring lattice sites (dashed and solid lines). In the real lattices, the triangles are rotated compared to each other, to form 3D structures.

fluctuate in a correlated manner and behave like a cooperative paramagnet. This type of correlated motion is also sometimes called spin liquid states, as an analogy to the correlated motion of molecules in real liquids.

A QSL is defined as a system with long range correlated quantum spin fluctuations all the way down to $T = 0$ K, with no long range ordering of the spins. In larger frustrated $S = 1/2$ antiferromagnetic spin systems, QSL behavior is caused by degenerate ground states that enables the spins to simultaneously point in many different directions even at the lowest temperature, much like the frustrated triangle. Since all spins behave according to a combined quantum ground states, they are strongly correlated.

A measure for the frustration in the system is the frustration parameter f , defined by

$$f = \frac{|\Theta_{CW}|}{T_O}, \quad (3.3)$$

where Θ_{CW} is the Curie Weiss temperature, and T_O is the temperature, where the magnetic system freezes into a single ordered magnetic ground state. In chapter 4 the Curie Weiss temperature and ordering temperature are further explained. If $f \approx 10$ magnetic frustration is strongly suppressing magnetic order. Magnetic order can per definition not occur in a QSL, and so a true QSL should in principle have $f = \infty$. A series of complications can make it difficult to get sure proof of absent magnetic order in real world materials, and $f > 100 - 1000$ is typically seen as a strong indication of a QSL. Measuring the frustration parameter is not the only way of identifying a QSL. A series of techniques can be used to identify QSL behavior, but none of them can identify a QSL alone. The entire problem with a sure proof of QSL states, is that one have to show that order in a magnetic system is not happening, and so we look for a non-broken symmetry.

Even with the experimental difficulties, a series of different systems have been found to be candidates for QSL states. In general, lattices which show QSL states usually consist of connected triangles in more or less exotic forms. Examples of lattices that have shown signs of hosting QSL are shown in figure 3.2.

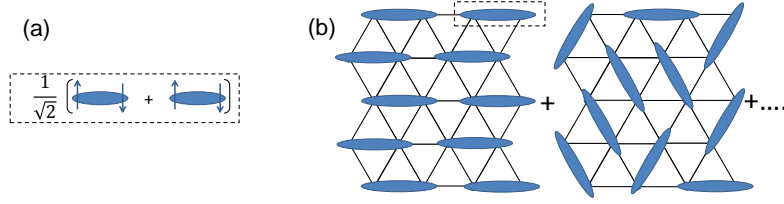


Figure 3.3: RVB states of the frustrated triangular lattice. (a) In RVB states, the spins are arranged in pairs forming dimer singlet states. (b) A RVB state is a superposition of different pairing of spins (A pairing is illustrated with a blue ellipse). The figure is based on reference [4].

It is usually difficult to find a QSL candidate theoretical ground state(s). The problem arises due to the size of lattice planes, and so exact solutions, like the one found for the triangle above, are difficult. There are numerous ways of constructing ground states to the Hamiltonian for such large systems, of which the most famous is the Resonating Valence Bond (RVB) state. The RVB states are created by making superposition of spin dimer singlet states, as illustrated in figure 3.3. The two spins in a pair can be separated over great distances or be right next to each other. RVB states have in this way highly entangled and fluctuating spins, even at $T = 0$ K. The problem with the RVB states is that there is an almost infinite way of constructing them for every lattice, and finding the right QSL ground state is therefore close to impossible [4].

A true QSL would have a degenerate ground state, but even systems with non-degenerate ground states can show QSL behavior. In reference [16], Normand proposes a definition of different types of spin liquid behaviors:

- Type 1 gapped spin liquid: The system has a non-degenerate singlet ground state, but with a small energy gap between both the low energy singlet states, as well as the lowest energy triplet states.
- Type 2 gapped spin liquid: The system has a continuum of low energy singlet states with no gap to the ground state. There is still an energy gap to the triplet states.
- Gapless spin liquid: The system has a continuum of singlet, triplet and even higher spin states, with practically zero energy gap to the groundstate.

The type 1 gapped spin liquid will at very low temperatures freeze into its ground state, whereas the type 2 will be able to experience gapless excitations into other singlet states. The gapless spin liquid is the most interesting case as it enables zero energy excitations, and has in principle a degenerate ground state. All the different spin liquid behaviors have a common feature which is that magnetic order is close to impossible, since very small thermal energies can excite the system into a manifold of low energy states.

3.3 Numerical solutions - solving large spin systems

It is impossible to find the exact ground state of a spin lattice of practically infinite size by brute force diagonalizing the full corresponding Heisenberg Hamiltonian. The spin lattice is therefore approximated by a small resembling spin lattice with periodic boundary conditions to reduce the system size. Numerical methods are required to find the ground state of the approximated lattice system.

Two of the most common methods of numerical calculations are Exact Diagonalization (ED) and Quantum Monte Carlo (QMC).

QMC uses stochastic algorithms to determine the eigenstates of rather large lattices to minimize finite system size effects. The application of QMC on frustrated spin systems has severe restrictions [17], and it has therefore not been used on the frustrated boelite system. QMC will not be elaborated further.

ED diagonalizes the Hamiltonian matrix to find some or all of the eigenstates of the system. How the eigenstates of the magnetically frustrated triangle were found above is an example of ED. The problem with ED is that the size of the Hamiltonian increases exponentially with the number of spins. The system size therefore needs to be reduced in order to do ED. I will in this thesis use two different types of ED. Both methods have their advantages and disadvantages, as will become apparent in the following subsections.

3.3.1 Lanczos algorithm and RLexact

A useful algorithm to find the eigenstates of a known Hamiltonian matrix, is the Lanczos algorithm. The description of Lanczos algorithm is based on [18]. The Lanczos algorithm transforms a matrix $\hat{\mathcal{H}}$ of $(N \times N)$ size into the tridiagonal matrix* $\hat{\mathbf{T}}$ of $(M \times M)$ size after M iterations of the algorithm. The algorithm uses an iterative method, which generates $\hat{\mathbf{T}}$ by constructing orthogonal Lanczos vectors \mathbf{v}_i

$$\hat{\mathcal{H}}\mathbf{v}_i = b_{i+1}\mathbf{v}_{i+1} + a_i\mathbf{v}_i + b_i\mathbf{v}_{i-1}, \quad (3.4)$$

where $i = 1 \dots M$. $b_{i+1}\mathbf{v}_{i+1}$, $a_i\mathbf{v}_i$, and $b_i\mathbf{v}_{i-1}$ are projection of $\hat{\mathcal{H}}\mathbf{v}_i$ along the two previous orthogonal Lanczos vectors \mathbf{v}_{i-1} and \mathbf{v}_i , and along a third Lanczos vector \mathbf{v}_{i+1} which is orthogonal to both \mathbf{v}_{i-1} and \mathbf{v}_i .

The values of a and b can easily be calculated as shown in reference [18]. The first Lanczos vector \mathbf{v}_0 is a random normalized vector of dimension $(M \times 1)$. For $i = 0$ the resulting vector is only projected along itself and one orthogonal vector.

The tridiagonal matrix $\hat{\mathbf{T}}$ is constructed by placing $a_1 \dots a_M$ in $\hat{\mathbf{T}}$'s diagonal and $b_1 \dots b_M$ in its off-diagonals. Diagonalizing $\hat{\mathbf{T}}$ is easily done, and it has the eigenvalues e_j and eigenvectors \mathbf{s}_j . If M is very large, the eigenvalues e_j are to a good approximation eigenvalues of

*A matrix with only non zero elements in its main diagonal, and in the first diagonal above and below the main diagonal.

$\hat{\mathcal{H}}$. A measure of the quality of the approximation is needed in order to minimize computational time. From the Lanczos vectors, a matrix $\mathbf{Q} = [\mathbf{v}_0, \mathbf{v}_1 \dots \mathbf{v}_M]$ can be constructed, and from \mathbf{Q} , the Ritz-vector is define by

$$\mathbf{r}_j = \mathbf{Q}\mathbf{s}_j. \quad (3.5)$$

The last element of \mathbf{r}_j is called the Ritz-measure and is a good measure of the quality of the approximation. e_j and r_j are to a good approximation eigenvalues and eigenvectors of $\hat{\mathcal{H}}$ if the last element in \mathbf{r}_j is sufficiently small.

As M is increased more and more e_j will converge towards the true eigenvalues of $\hat{\mathcal{H}}$. The eigenvalues with the largest absolute size will converge the fastest, and hence have a larger chance of being found with the Lanczos algorithm.

The major advantage of Lanczos algorithm is that the eigenvalues with the largest absolute size is found very quickly. M does not need to be very large. At the same time the Lanczos algorithm can be used with a sparse $\hat{\mathcal{H}}$ matrix, which reduces the required computer memory. Unfortunately a standard Lanczos algorithm can not find degenerate states, and it is not feasible to try to find eigenvalues with a small magnitude. The program RLexact [19] was used to ED the Boleite system with the help of Lanczos algorithm. RLexact usually has a Ritz-measure of around 10^{-9} , and is capable of finding the ground state of a 2D triangular Heisenberg $S = 1/2$ spin lattice as large as 6×6 spins [20].

RLexact can also be used to find the neutron cross section of an eigenstate, but this will not be elaborated further in this thesis.

3.3.2 Complete diagonalization

The second ED method is the Complete Diagonalization (CD), which could also be known as brute-force diagonalization. With CD all eigenstates are found. The major advantage of this is that degenerate states are identified, and thermodynamic properties of bulk system can be calculated, since it requires all eigenstates, as shown in chapter 4. Closely related to the advantages of CD are the disadvantages. Since all eigenstates are found, the full Hamiltonian needs to be diagonalized, and so sparse matrix techniques are not necessarily feasible. This reduces the size of the system which can be solved compared to the Lanczos algorithm, since the amount of memory required to find a Hamiltonian to a system with N spins scales with $(2^N)^2$.

The CD used in this thesis is primarily done with the *eig* function in MATLAB [21].

RLexact can also do CD. The CD implemented in RLexact use the complex householder algorithm, explained in reference [22], to transform a $(N \times N)$ matrix into its tridiagonal form of similar size. The tridiagonal matrix can now, as done for the Lanczos algorithm, be diagonalized. With CD it is only possible to solve system of around 18 spins with RLexact.

CHAPTER 4

An introduction to bulk measurements

Bulk measurement techniques are essential in investigating the magnetic properties of a solid. The techniques do not require a large sample mass, and magnetic ordering is often easily identified. In this chapter I will introduce some basic theory behind the magnetic susceptibility, the magnetization as a function of field, and the heat capacity of a magnetic solid. The chapter will also include a brief introduction to the experimental instruments that were used.

4.1 The magnetisation of a solid

The magnitude of the total magnetization \mathbf{M} of a solid is given by $M = g\mu_B N \langle m \rangle$, where $\langle m \rangle$ is the average magnetic moment along the $\hat{\mathbf{z}}$ -direction. If an external magnetic field with a magnitude H is applied along the $\hat{\mathbf{z}}$ -direction the total magnetization can be written as [24]

$$M = g\mu_B N \langle m \rangle = \frac{g\mu_B N}{Z} \sum_{i=1}^N m_i \exp \left(-\frac{E_i - m_i g\mu_B \mu_0 H}{k_B T} \right). \quad (4.1)$$

N is the total number of states, m_i and E_i are the magnetization and the energy of the state i respectively, $k_B T$ is the thermal energy at temperature T , and Z is the partition function which is given by

$$Z = \sum_{i=1}^N \exp \left(-\frac{E_i - m_i g\mu_B \mu_0 H}{k_B T} \right). \quad (4.2)$$

4.2 The susceptibility from a solid

Any magnetic system with exchange interaction can be seen as free spins above a certain critical temperature, where the thermal energy is large enough to excite the system into all its excited states. Below this critical temperature, the system will experience a symmetry break and order into its low-energy states. For a ferromagnet the critical temperature is called the Curie temperature T_C , and for an antiferromagnet it is known as the Néel temperature T_N . These critical temperatures can be identified as kinks in the inverse susceptibility.

A completely paramagnetic system will not have a critical temperature, as the spins behave freely all the way to $T = 0$ K. The result is that the inverse susceptibility of a paramagnet

will follow a straight line, with $1/\chi \rightarrow 0$ for $T \rightarrow 0$ K. Below the Néel temperature, an antiferromagnetic system can either have an increasing or decreasing susceptibility depending on whether the system's spins freeze into a degenerate or non-degenerate ground state. If an antiferromagnet orders into a single frozen ground state $\chi \rightarrow 0$ for $T \rightarrow 0$ K, when the external field is applied parallel to the external field. T_N is in this case the critical temperature for ordering. If the ground state is degenerate, like the magnetic triangle described in chapter 3, the system will behave like a paramagnet below the Néel temperature, and so it will have $1/\chi \rightarrow 0$ for $T \rightarrow 0$ K.

The exchange interaction parameter of a magnetic system can classically be calculated directly from the critical temperature. For an antiferromagnet (with $S = 1/2$ and $L = 0$) the result is [14]

$$\sum_i J_i = 4k_B T_N, \quad (4.3)$$

where $\sum_i J_i$ is the sum across the exchange constants per magnetic ion. For a magnetic triangle with exchange coupling J between the spins, equation 4.3 reduces to $J = 2k_B T_N$.

4.2.1 Curie Weiss Law

A model of the inverse susceptibility at high temperature can be found from a classical mean field approximation. In this approximation, the interaction with neighboring ions is seen as a molecular field B_{mf} . In the limit where $k_B T \gg \mu_B(B + B_{mf})$, which is somewhere above the critical temperature, the susceptibility can be approximated to have a paramagnetic behavior following the Curie Weiss Law*

$$\chi = \frac{C}{T - \Theta_{CW}}. \quad (4.4)$$

The Curie Constant, when expressed in SI-unit, is given by

$$C = \frac{N\mu_B^2\mu_0 N_A}{k_B}, \quad (4.5)$$

for $S = 1/2$ and $L = 0$, where N is the number of magnetic moments per unit volume and N_A is Avogadro's number. Θ_{CW} is the Curie Weiss temperature. For an antiferromagnet $\Theta_{CW} < 0$, for a ferromagnet $\Theta_{CW} > 0$, and for a paramagnet $\Theta_{CW} = 0$ [2]. According to the Curie-Weiss Law, the inverse susceptibility will be linear above a certain temperature

$$\frac{1}{\chi} = \frac{T - \Theta_{CW}}{C}. \quad (4.6)$$

If the Curie Weiss model is fitted to the susceptibility curve at temperatures T larger than the ordering temperature of the system, a ferromagnet will have $T_C = \Theta_{CW}$, and

*The approximation is described in more detail in Blundell [2].

an antiferromagnet $-T_N = \Theta_{\text{CW}}$. If the model is fitted to the susceptibility curve at temperatures too close to the ordering temperature, the mean field approximation breaks down and $|\Theta_{\text{CW}}|$ begins to diverge from the true critical temperatures.

4.2.2 Calculating the susceptibility

The susceptibility of a given quantum system can be solved numerically using [23]

$$\chi = \left(\frac{\partial M}{\partial H} \right)_{H=0}. \quad (4.7)$$

In the limit where $m_i g \mu_B \mu_0 H \ll E_i$, the Zeeman term in equation (4.1) can be neglected. The susceptibility is found by combining equation (4.7) and (4.1)

$$\begin{aligned} \chi &= \frac{g^2 \mu_B^2 \mu_0 N}{k_B T} \left(\frac{1}{Z} \sum_{i=1}^N m_i^2 \exp \left(-\frac{E_i}{k_B T} \right) - \left(\frac{1}{Z} \sum_{i=1}^N m_i \exp \left(-\frac{E_i}{k_B T} \right) \right)^2 \right) \\ &= \frac{g^2 \mu_B^2 N \mu_0}{k_B T} (\langle m^2 \rangle - \langle m \rangle^2). \end{aligned} \quad (4.8)$$

In an antiferromagnet $\langle m \rangle = 0$ when $m_i g \mu_B \mu_0 H \ll E_i$, so for an antiferromagnetic system equation (4.8) reduces to

$$\chi = \frac{g^2 \mu_B^2 N \mu_0}{k_B T Z} \left(\sum_{i=1}^N m_i^2 \exp \left(-\frac{E_i}{k_B T} \right) \right). \quad (4.9)$$

4.3 The heat capacity of a solid

The heat capacity of an insulating, magnetic sample can be separated into two contributions

$$C_V = C_{\text{lat}} + C_{\text{Mag}}, \quad (4.10)$$

where C_{lat} is the contribution from thermal lattice vibrations, which in quantum mechanics are quantized and called phonons, and C_{Mag} is the magnetic contribution.

The C_{lat} can be described by the Debye model. The Debye model will not be described in detail, but its basic assumptions are that the phonons can be viewed as standing waves in a box, the heat capacity is measured at constant volume V , and that the speed of sound v is constant in the solid. Using this, the Debye model predicts that C_{Lat} for a solid consisting of N atoms is given by [14]

$$C_{\text{Lat}} = 9Nk_B \left(\frac{T}{\theta_D} \right)^3 \int_0^{\theta_D/T} \frac{x^4 e^x}{(e^x - 1)^2}, \quad (4.11)$$

where $x_D = \frac{\theta_D}{T}$, with $\theta_D = \frac{\hbar v}{k_B} \left(\frac{6\pi^2 N}{V} \right)^{1/3}$ being the Debye temperature and $x = \frac{\hbar \omega}{k_B T}$. ω is given by the dispersion relation $\omega = vK$, where K is the length of the phonon wave vector.

In the limit $T \ll \theta_D$, equation (4.11) reduces to [14]

$$C_{\text{Lat}} \approx 218Nk_B \left(\frac{T}{\theta_D} \right)^3, \quad (4.12)$$

which is called the Debye T^3 approximation.

At high temperature the lattice heat capacity will normally be the by far largest contribution to the total heat capacity. As $T \rightarrow 0$, $C_{\text{Lat}} \rightarrow 0$ according to equation (4.12), and here C_{Mag} begins to play an important part.

From statistical quantum mechanics [23] it is known that $C_{\text{Mag}} = \left(\frac{\partial U}{\partial T} \right)_{H,V}$, where the total energy U can be rewritten in terms of the average energy of a magnetic system $\langle E \rangle$ and the number of individual, isolated magnetic systems per unit cell N . This can be used to numerically calculate the magnetic heat capacity with

$$C_{\text{Mag}} = N \left(\frac{\partial \langle E \rangle}{\partial T} \right)_{H,V}, \quad (4.13)$$

where the expectation value of the energy is given by

$$\langle E \rangle = \frac{1}{Z} \sum_i E_i \exp \left(\frac{-E_i}{k_B T} \right). \quad (4.14)$$

By combining equation (4.13) and (4.14) the result is

$$\begin{aligned} C_{\text{Mag}} &= \frac{N}{k_B T^2} \left[\frac{-1}{Z^2} \cdot \left(\sum_i E_i \exp \left(\frac{-E_i}{k_B T} \right) \right)^2 + \frac{1}{Z} \sum_i E_i^2 \exp \left(\frac{-E_i}{k_B T} \right) \right] \\ &= \frac{N}{k_B T^2} [\langle E^2 \rangle - \langle E \rangle^2]. \end{aligned} \quad (4.15)$$

4.4 Bulk measurement techniques

4.4.1 Measuring the magnetisation and susceptibility

A series of instruments located at a range of facilities were used to measure the susceptibility and magnetization. Two of the instruments are located at Paul Scherrer Institute (PSI), two at École polytechnique fédérale de Lausanne (EPFL), and one at Aarhus University (AU). The instruments at AU and the first of the instruments at PSI are Physical Property Measurement System (PPMS) from Quantum Design. The second instrument at PSI and one of the EPFL instruments are Magnetic Property Measurement Systems (MPMS), also from Quantum Design. The last instrument at EPFL is an AC-susceptometer.

Both PPMS and MPMS instruments are using the Vibrating Sample Magnetometer (VSM) technique. In the VSM technique, the sample is mechanically oscillated around the center of two superconducting pickup coils, and an external field is applied in the direction of the of the samples motion as illustrated in figure 4.1. The principle is that a moving, magnetic sample, which is slightly magnetized due to an applied external magnetic field, will generate an AC electromotive force in the pickup coils placed around the sample. Two counter-wound superconducting compensation coils are placed far from the pickup coils to compensate for external fields with a linear

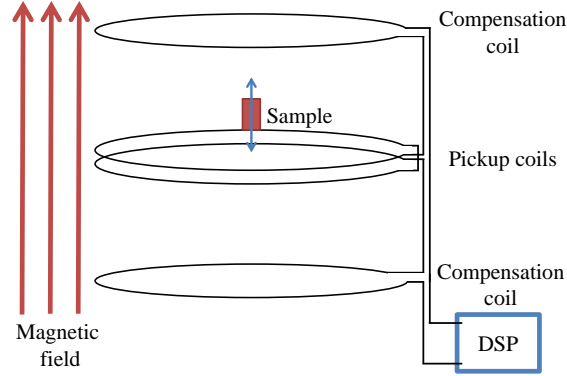


Figure 4.1: Illustration of the VSM technique as used in the PPMS instrument. A sample is placed between two pickup coils and vibrated along an external magnetic field. Two counter wound outer compensation coils minimize the impact from linear field gradients and external magnetic fields. The AC electromotive force generated in the coils are in the PPMS registered with a DSP [25].

gradient or non uniform external fields [25]. Combined, the pick-up coils and compensation coils are called the detection coils.

In the PPMS, the induced AC voltage in the detection coils is directly recorded by a Digital Signal Processor (DSP) [25], whereas the MPMS use the more accurate Superconducting QUantum Interference Device (SQUID) measurement technique [26]. The SQUID measurement technique consists of a complex electronic circuit which includes two so called Josephson junctions, combined with a DSP. Josephson junctions use Josephson tunneling between two superconducting materials separated by a non superconducting materials[†]. The effect of the SQUID circuit is that its feedback nulls the current in the detection coils while the feedback current can be recorded by the DSP for further analyses. In this way, the noise in the detection coils can be reduced by a factor of 10. The recorded voltage can then be translated into the systems total magnetization M [26]. By using the linear approximation, the susceptibility can be calculated from $\chi = \frac{M}{H}$.

An AC-susceptometer, like the one used at EPFL, uses a fixed sample in a changing field instead of changing the sample position in a constant DC-field. The changing field is created by superimposing an AC field on top of the DC-field. With a changing field the susceptibility is no longer linearly dependent on the absolute value of M , but instead $\chi = \frac{dM}{dH}$. The advantage of the technique is that small magnetic shifts can be detected even at large absolute magnetization [27].

4.4.2 Measuring the heat capacity.

The heat capacity of our Boleite samples have been measured by a PPMS in AU. When the PPMS is used for heat capacity measurements, the samples are mounted on a sample stage which is suspended by 8 thin wires inside a heat puck. The heat puck is a metal container used for heat reference and the electronic connections to the PPMS instrument. The 8 wires between the heat puck and the sample stage work as leads for the embedded heater and sample stage thermometer.

[†]More explanation on the effects of two Josephson junction can be found in [28].

The 8 wires also enable thermal conduction between sample stage and the heat puck. The heat puck's temperature is monitored with a thermometer as well.

A measurement of the heat capacity is done in 3 steps. First, the sample temperature is stabilized to the puck temperature. Secondly, the power to the sample stage heater is turned on for a short period while the sample stage and puck temperatures are measured. After turning off the power to the sample stage, the sample and sample stage are allowed to cool down to the puck temperature while measuring the temperature of both. The two temperature measurements and the heating power are the raw data of the instrument.

Afterwards, instrument software uses two different models to estimate the heat capacity from the raw data. One model assumes a bad thermal connection between the sample and the sample stage, and the other model assumes a perfect connection between the sample and the sample stage. The software then determines the heat capacity from the model which was best able to account for the raw data [29].

CHAPTER 5

Introduction to Neutron Scattering

The neutron was discovered by James Chadwick in 1932. Already in the middle of the 1930's, the first neutron scattering experiments were conducted, and with the introduction of nuclear reactors after World War II, neutron scattering techniques evolved dramatically [30]. Neutron scattering is today a key technique in investigating magnetic samples where it can be used as a probe to measure both the magnetic structures and dynamics inside materials. In this chapter, I will introduce the basic theory of neutron scattering before moving on to introducing the neutron instruments that were used in the boleite experiments.

5.1 Properties of the neutron

The neutron is a charge neutral, spin 1/2 particle consisting of two spin-down quarks and one spin-up quark. The neutron is only stable inside the nucleus, and when it is in its free state it will decay with a decay time of 886 s [31]. Luckily, the decay time of the neutron is of minor importance to neutron scattering experiments which take a fraction of a second.

The neutron can interact with the lattice by either being absorbed or scattered. The de Broglie wavelength* λ of cold and thermal neutron is of the length scale of inter atomic distances, which results in wave interference effects when the neutrons interact with the crystal lattices. The neutron's zero charge ensures that the neutron will not feel any Coulomb repulsion from the electron clouds of the atoms, and so the neutron is scattered by the atom's nuclei due to the strong nuclear force. The neutron's spin gives it a magnetic moment, and it will therefore also interact with magnetic structures inside a material. This makes the neutron very attractive as a supplement probe to photons (used in light and x-ray scattering). Photons do not have a net spin and are interacting with the electron clouds of the atoms, making photon scattering increase with the atomic number [32]. The intensity of scattering is usually given in terms of the scattering cross section, which will be described in the following section. The difference in the scattering cross section of neutrons and x-rays through the periodic table is illustrated in figure 5.1.

The mass m_n , speed v , wave vector k , magnetic moment μ_n , and energy E of the neutron are given by [32]

$$m_n = 1.674927 \cdot 10^{-27} \text{ kg}, \quad (5.1)$$

$$v = \frac{\lambda h}{m_n}, \quad (5.2)$$

$$E = \frac{m_n v^2}{2}, \quad (5.3)$$

$$k = \frac{2\pi}{\lambda}, \quad (5.4)$$

$$\mu_n = -1.04188 \cdot 10^{-3} \mu_B. \quad (5.5)$$

*Wavelength of matter waves.

5.2 Basic scattering

The following section is based on reference [32] and [33], with a few additional references mentioned in the text.

5.2.1 The Scattering Cross Section

A key concept of neutron scattering is

$$\text{the neutron flux} \equiv \Psi \equiv \frac{I_A}{A}, \quad (5.6)$$

where I_A is the rate of neutrons through the area A . The neutron scattering cross section of a material defines the ability of the material to scatter neutrons. The number of neutrons scattered per second I_s will naturally dependent on the flux upon the material, and therefore it is defined that

$$\text{the neutron scattering cross section} \equiv \sigma \equiv \frac{I_s}{\Psi}. \quad (5.7)$$

A single nucleus' cross section can be seen as the area of the nucleus. A similar cross section is defined for the absorption of the neutrons. The Born approximation can be used for thin samples. In the Born approximation, it is assumed that there is zero attenuation through the sample; hence, the scattering cross section should be proportional to the sample volume.

The detectors placed around a sample only cover a limited solid angle $d\Omega$. The rate of neutrons being scattered into that solid angle from the sample is given by dI_s , and per definition

$$\text{the differential scattering cross section} \equiv \frac{d\sigma}{d\Omega} \equiv \frac{1}{\Psi} \frac{dI_s}{d\Omega}. \quad (5.8)$$

The total neutron scattering cross section can be found by integrating the differential scattering cross section across all scattering angles

$$\sigma = \frac{1}{\Psi} \int \frac{d\sigma}{d\Omega} d\Omega. \quad (5.9)$$

Neutron scattering can involve change in the neutrons' kinetic energy. The neutron will before scattering of a sample have an incident energy E_i , and a final energy E_f after the scattering process. The neutron can both scatter without changing its kinetic energy, $E_i = E_f$, known as elastic neutron scattering, or scatter with a loss or gain of kinetic energy, $\Delta E = E_f - E_i$, which is known as inelastic scattering. Since there is also an energy change involved in the scattering, it is useful to define

$$\text{the partial differential scattering cross section} \equiv \frac{d^2\sigma}{d\Omega dE} \equiv \frac{1}{\Psi} \frac{dI_{s,dE}}{d\Omega}, \quad (5.10)$$

where $dI_{s,dE}$ is defined as the scattering rate of neutrons with energy of $[\Delta E, \Delta E + dE]$ into solid angle $d\Omega$.

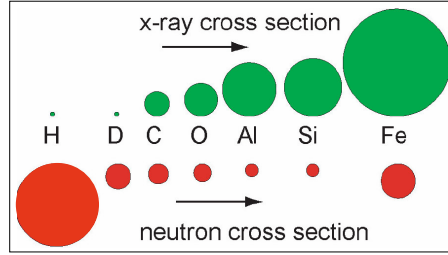


Figure 5.1: X-ray and neutron scattering cross section for specific elements. The X-ray scattering cross section depends on the amount of electrons in the atoms and thereby the atomic number, whereas the neutron scattering cross section varies randomly with atomic number and isotope. The figure is borrowed from John R.D. Copley's presentation [34].

5.2.2 The neutron as a wave

The direction of the scattered neutron beam has its roots in constructive interference of the neutron's wave function, due to the atomic lattice. Figure 5.2 illustrates how the neutron wave will make constructive interference with itself when scattering off two nuclei. A materials composition can be deduced from the scattering pattern, but a little math is needed in order to describe how. The incoming neutrons can be described by a plane wave

$$|\psi_i\rangle = |\mathbf{k}_i\rangle|\sigma_i\rangle = \frac{1}{\sqrt{Y}} e^{i\mathbf{k}_i \cdot \mathbf{r}} e^{i\omega t} |\sigma_i\rangle, \quad (5.11)$$

where $Y = L^3$ is a normalization volume assuming that $|\psi_i\rangle$ is enclosed in a box with sides L , and $|\sigma_i\rangle$ is the initial spin state of the neutron. The time dependent term of equation (5.11) is only important for inelastic scattering, and it will therefore be omitted in the following.

The incoming flux, defined in equation (5.6), can be written in terms of the incoming wave function as

$$\Psi_i = |\psi_i|v = \frac{1}{Y} \frac{\hbar k_i}{m_n}. \quad (5.12)$$

When the neutron interacts with the sample, it will be scattered. The wave function of the neutron after scattering will be expressed by

$$|\psi_f\rangle = |\mathbf{k}_f\rangle|\sigma_f\rangle = \frac{1}{\sqrt{Y}} e^{i\mathbf{k}_f \cdot \mathbf{r}} |\sigma_f\rangle. \quad (5.13)$$

The summed rate of change between the neutron incoming state, $|\psi_i\rangle$, and the continuum of possible final states $|\psi_f\rangle$, is described by *Fermi's Golden Rule*

$$\sum_f W_{i \rightarrow f} = \frac{2\pi}{\hbar} \frac{dn}{dE_f} |\langle \psi_i | \hat{V} | \psi_f \rangle|^2, \quad (5.14)$$

where $\frac{dn}{dE_f}$ is the density of final states, and \hat{V} is the operator responsible for the description of the interaction. In the case of neutron nuclei interaction, \hat{V} is called *the Fermi pseudopotential*.

The density of final states into the direction $d\Omega$ can be written $\left. \frac{dn}{dE_f} \right|_{d\Omega} = \frac{Y k_f m_n}{\hbar^2 (2\pi)^3} d\Omega$, and therefore

$$\sum_f W_{i \rightarrow f, d\Omega} = \frac{Y k_f m_n}{\hbar^3 (2\pi)^2} d\Omega |\langle \psi_i | \hat{V} | \psi_f \rangle|^2. \quad (5.15)$$

$\sum_f W_{i \rightarrow f, d\Omega}$ is the number of neutrons scattering in the direction of $d\Omega$, and so it can be used to calculate the differential scattering cross section by $\frac{d\sigma}{d\Omega} = \frac{1}{\Psi} \frac{\sum_f W_{i \rightarrow f, d\Omega}}{d\Omega}$. The energy dependence of the neutrons can also be included, and the partial differential scattering cross section is then given by

$$\left. \frac{d^2\sigma}{d\Omega dE} \right|_{\phi_i \rightarrow \phi_f} = \frac{k_f}{k_i} \left(\frac{Y m_n}{\hbar^2 (2\pi)} \right)^2 |\langle \psi_i | \phi_i | \hat{V} | \psi_f \phi_f \rangle|^2 \delta(E'_i - E'_f + \Delta E), \quad (5.16)$$

where ϕ_i and ϕ_f denotes the quantum state of the scattering sample, with energy E'_i and E'_f respectively. ΔE is the change in neutron energy. Equation (5.16) explicitly introduced energy conservation with the delta function.

The Fermi pseudopotential \hat{V} depends on which atoms that are in the scattering system, and how they are distributed. For a single nucleus, labeled j , the Fermi pseudopotential will be

$$\hat{V}_j = \frac{2\pi\hbar^2}{m_n} b_j \delta(\mathbf{r} - \mathbf{r}_j). \quad (5.17)$$

b_j is ion-dependent, and it is usually called the scattering length due to its unit of length. Assuming that the interaction between nuclei and neutron does not affect the spin state of the neutron $\langle \sigma_f | \sigma_i \rangle = 1$, one can write

$$\langle \psi_f | \hat{V}_j | \psi_i \rangle = \frac{2\pi\hbar^2}{Y m_n} b_j e^{i\mathbf{q} \cdot \mathbf{r}_j}, \quad (5.18)$$

where \mathbf{q} is called the scattering vector given by

$$\mathbf{q} = \mathbf{k}_i - \mathbf{k}_f. \quad (5.19)$$

Equation (5.18) could be extended to two nuclei by writing the Fermi pseudopotential as $\hat{V} = \hat{V}_j + \hat{V}_{j'}$, and thereby get

$$\langle \psi_f | \hat{V} | \psi_i \rangle = \frac{2\pi\hbar^2}{Y m_n} (b_j e^{i\mathbf{q} \cdot \mathbf{r}_j} + b_{j'} e^{i\mathbf{q} \cdot \mathbf{r}_{j'}}). \quad (5.20)$$

It is clear that expanding the system to more atoms would result in the Fermi pseudopotential being the sum across all the atoms' scattering lengths. Before moving on to look at the case of a the scattering from an entire single crystal, I will first introduce the concept of incoherent scattering. Equation (5.16) can be separated into two terms

$$\frac{d^2\sigma}{d\Omega dE} = \left. \frac{d^2\sigma}{d\Omega dE, \text{el}} \right|_{\text{coh}} + \left. \frac{d^2\sigma}{d\Omega dE} \right|_{\text{inc}}. \quad (5.21)$$

The label coh and inc stand for coherent and incoherent respectively. Coherent and incoherent scattering have their roots in variation of neutron scattering length of each ion. Even though the ions can be set to have an average scattering length $\langle b_j \rangle$, there are local deviations making the

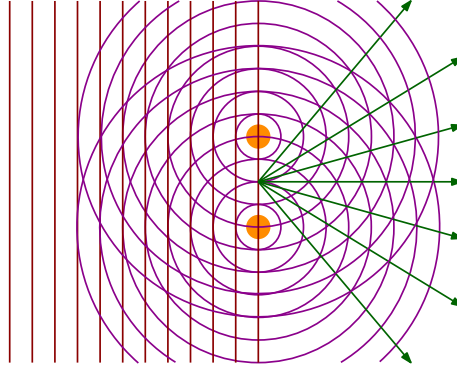


Figure 5.2: A plane neutron wave (vertical red lines) scattering of two nuclei (yellow discs) will create two spherical waves (purple circles), which will have constructive interference along the green arrows.

scattering length different between every ion. The variation can both be dynamic or static and can either be due to variations in the nuclear isotopes or the nuclear spin. The variation can be explained very simply by assuming that the sample is large enough to represent an ensemble average, and that the observation time is much longer than the nuclear fluctuation. The deviation can be represented by the stochastic variable δb_j , with the ensemble average $\langle \delta b_j \rangle = 0$, which makes the total scattering length per ion

$$b_j = \langle b_j \rangle + \delta b_j. \quad (5.22)$$

Assuming that the deviation is independent between sites $\langle \delta b_j \delta b_{j'} \rangle = 0$. The implication is that the coherent partial differential scattering cross section is partly dependent on the different nuclei position at the same time, which gives rise to interference effects. The incoherent partial differential scattering cross section does not give rise to any interference, and so it is independent of \mathbf{q} .

The total incoherent scattering cross section, σ_{inc} from a single nuclei can be looked up in tables like [35], where the listed σ_{inc} are originally found from thermal scattering experiments. The total incoherent scattering cross section $\sigma_{\text{inc,tot}}$, from a system of n different nuclei in the unit cell, is simply the sum of the individual nuclei's incoherent scattering cross sections

$$\sigma_{\text{inc,tot}} = \sum_i^n \sigma_{\text{inc},i}. \quad (5.23)$$

5.3 The nuclear neutron scattering cross section

In this section, equation (5.16) will be extended to account for the scattering from a single crystal.

5.3.1 Nuclear scattering cross section of a single crystal

The coherent elastic nuclear differential neutron scattering cross section from a crystal will be the summed scattering from all atoms' nuclei in the crystal. The way to calculate this is to extend

equation (5.20) to a sum across all the crystal's nuclear scattering lengths. Luckily, the periodicity of a crystal can be used to minimize the calculation, and the coherent elastic nuclear differential neutron scattering cross section can be reduced to two factors [33]:

- The *nuclear structure factor* $F_N(\mathbf{q})$, which accounts for the scattering from a single unit cell.

$$F_N(\mathbf{q}) = \sum_j b_j e^{-2W_j} e^{i\mathbf{q} \cdot \mathbf{\Delta}_j}, \quad (5.24)$$

where $\mathbf{\Delta}_j$ is the basis vector, which describes the j 'th atom's position in the unit cell. The Debye-Waller factor e^{-2W_j} is included to take the thermal motion of the scattering nucleus into account. As hinted in the j index, the Debye-Waller factor is site dependent. Fortunately, the Debye-Waller factor can be approximated to be the same for all sites [32]

$$2W \approx \frac{1}{3} q^2 \cdot \langle u^2 \rangle, \quad (5.25)$$

where q is the magnitude of \mathbf{q} and $\langle u^2 \rangle$ is the mean square displacement of the scattering nuclei. For the cubic lattice $\langle u^2 \rangle$ increases with temperature. The Debye-Waller factor is therefore maximum one and decreases as q^2 and temperature are increased.

- A factor accounting for the combined scattering of N unit cells, given by

$$\left| \sum_u e^{i\mathbf{q} \cdot \mathbf{r}_u} \right|^2 = N \frac{(2\pi)^3}{V_0} \delta(\mathbf{q} - \boldsymbol{\tau}), \quad (5.26)$$

where V_0 is the volume of one unit cell, and $\boldsymbol{\tau}$ is the reciprocal lattice vector. For a cubic lattice

$$\boldsymbol{\tau} = h \frac{2\pi}{a} \hat{\mathbf{x}} + k \frac{2\pi}{a} \hat{\mathbf{y}} + l \frac{2\pi}{a} \hat{\mathbf{z}}, \quad (5.27)$$

where a is the length the of cubic unit cell, and (h, k, l) are the Miller indices. The magnitude of the reciprocal lattice vector can be written

$$\tau = n \frac{2\pi}{d}, \quad (5.28)$$

where d is the spacing between lattice planes and n is an integer.

The nuclear coherent differential scattering cross section is then given by a combination of the two factors

$$\left. \frac{d\sigma}{d\Omega} \right|_{\text{coh el}} = N \frac{(2\pi)^3}{V_0} |F_N(\mathbf{q})|^2 \sum_{\mathbf{q}} \delta(\mathbf{q} - \boldsymbol{\tau}). \quad (5.29)$$

5.3.2 Bragg's law and the Laue Condition

The delta function in equation (5.29) shows that the elastic coherent nuclear scattering only happens when

$$\boldsymbol{\tau} = \mathbf{q}, \quad (5.30)$$

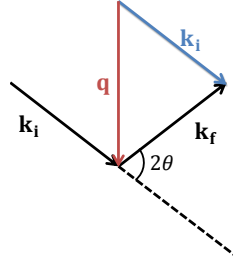


Figure 5.3: Illustration of the scattering triangle, which shows how \mathbf{q} is defined as the difference between \mathbf{k}_i and \mathbf{k}_f .

which is called the Laue condition. The implication of the Laue condition is that the elastic coherent nuclear scattering will show up as peaks in the reciprocal space at integer values of (h, k, l) .

Including the initial and final wave vector of the neutron $\boldsymbol{\tau} = \mathbf{q} \equiv \mathbf{k}_i - \mathbf{k}_f$, where the angle between \mathbf{k}_i and \mathbf{k}_f is 2θ , as illustrated in figure 5.3. For elastic scattering, the magnitude of the scattering vectors are constant $k = k_i = k_f = \frac{2\pi}{\lambda}$, and the Laue condition can be written into the magnitude form $\tau = 2k \sin(\theta)$. Combining this with equation (5.28), Bragg's law is identified

$$n\lambda = 2d \sin(\theta), \quad (5.31)$$

where n is an integer. Bragg's law shows that neutrons with a series of wavelengths are scattered given by $\lambda_n = \frac{1}{n} 2d \sin(\theta)$. Bragg's law and the Laue condition show the same thing in two different spaces, namely that coherent nuclear scattering only happens when the distance between the lattice planes allow for constructive interference of scattering waves. The Laue condition describes the scattering condition in reciprocal space, and Bragg's law describes it in real space.

5.3.3 Bragg Peaks

The elastic scattering from a single crystal in a monochromatic[†] beam will not result in a delta function when measuring at $\mathbf{q} = \boldsymbol{\tau}$ as equation (5.29) suggests. Instead a peak with non zero width is measured, called a Bragg peak. The broadening arises from two factors: Mosaic spread of the crystal and instrumental resolution [32].

Mosaic spread arises from the fact that a single crystal is never a perfect single crystal but can rather be viewed as a number of small crystallites distributed around a mean direction. The FWHM of this distribution is called the mosaic of the crystal.

Instrumental resolution is a phenomenon with many causes; the incoming neutron beam has a natural divergence, the beam will not be completely monochromatic, and so on. All combined it gives a broadening of the Bragg peak.

5.4 Inelastic neutron scattering cross section

Equation (5.29) describes elastic scattering from neutrons interacting with the stationary lattice. Scattering neutrons can also absorb or deposit energy in the lattice in an inelastic processes. The

[†]A single wavelength.

next two subsections will describe what the inelastic cross section looks like when the neutron is interacting with magnetism or phonons in a crystal.

5.4.1 Phonon cross section

There are $3N$ different phonon modes for a lattice with N atoms in the unit cell. The phonons are separated into two groups [14]:

- 3 modes with zero energy at the Brillouin zone center $q' = 0$, and usually maximum energy at the zone boundary $\mathbf{q}' = \pi/a$. Here a is the unit cell length (for simple cubic), and q' is the phonon wave vector magnitude. These phonons are called acoustic phonons, and their dispersion relation follows

$$\hbar\omega_s \propto \left| \sin \left(\frac{\mathbf{q}' \cdot \mathbf{a}}{2} \right) \right| \quad (5.32)$$

- The other $3(N - 1)$ modes are called optical phonons. Their energy are always larger than zero, and they typical have maximum energy around the Brillouin zone center.

Since phonons are bosons, the occupation number n_s of a phonon mode with energy $\hbar\omega_s$ is given by Bose statistics [24]

$$n_s = \frac{1}{e^{\frac{\hbar\omega_s}{k_B T}} - 1}. \quad (5.33)$$

When the neutron scatters off the crystal planes, it can create or absorb a phonon by depositing energy in or gaining energy from the lattice. The coherent phonon partial differential scattering cross section for any lattice is given by [32]

$$\begin{aligned} \left(\frac{d^2\sigma}{d\Omega dE} \right) &= \frac{k_f}{k_i} \frac{(2\pi)^3}{2V_0} \sum_{s,d,\boldsymbol{\tau}} \frac{e^{-2W}}{\omega_s} \left| \frac{b_d}{M_d} e^{i\mathbf{q} \cdot \mathbf{d}} (\mathbf{q} \cdot \mathbf{e}_{d,s}) \right|^2 \\ &\times [\langle n_s + 1 \rangle \delta(E_i - E_f - \omega_s) \delta(\mathbf{q} - \mathbf{q}' - \boldsymbol{\tau}) + \langle n_s \rangle \delta(E_i - E_f + \omega_s) \delta(\mathbf{q} + \mathbf{q}' - \boldsymbol{\tau})]. \end{aligned} \quad (5.34)$$

The sum in equation (5.34) is taken across all phonon modes, indexed s , all lattice vectors $\boldsymbol{\tau}$, and the position of all atoms \mathbf{d} in the unit cell. The phonon mode sum is a double sum running across phonon wave vector, \mathbf{q}' and polarization index of the phonon mode p . $\hbar\omega_s$ is the energy of the s phonon mode with wave vector \mathbf{q}' . M_d and b_d are the mass and scattering length respectively of the atom at site d . $\mathbf{e}_{d,s}$ is the polarization vector of the phonon for the s phonon mode.

The two terms $\langle n_s + 1 \rangle \delta(\omega - \omega_s) \delta(\mathbf{q} - \mathbf{q}' - \boldsymbol{\tau})$ and $\langle n_s \rangle \delta(\omega + \omega_s) \delta(\mathbf{q} + \mathbf{q}' - \boldsymbol{\tau})$ represent phonon absorption and emission through the scattering process. $\langle n_s \rangle$ and $\langle n_s + 1 \rangle$ are the population factors. If the temperature is approaching zero, only the lattice ground state is populated and thereby the neutrons can not gain energy from absorbing a phonon. The neutron would still be able to create a phonon in the scattering process. This result is also reflected by $\langle n_s \rangle \rightarrow 0$ and $\langle n_s + 1 \rangle \rightarrow 1$ for $T \rightarrow 0$, which shows that only phonon creation, and not absorption, that can happen at very low temperatures.

5.4.2 Magnetic cross section

Neutrons interact with magnetic fields inside a sample since they are spin-1/2 particles. Elastic neutron scattering from magnetic long range ordered system resembles the nuclear coherent scattering, with Bragg peaks forming in specific parts of the reciprocal space. The magnetic peak position will be governed by a delta function like $\delta(\mathbf{q} - \boldsymbol{\tau} - \mathbf{Q})$, where \mathbf{Q} is the magnetic ordering vector. In general, antiferromagnetically ordered systems will form a bipartite lattice, as shown in figure 2.2, and so the ordering vector is positioned on the Brillouin zone boundary ($\mathbf{Q} = n\frac{\pi}{a}\hat{\mathbf{x}} + m\frac{\pi}{a}\hat{\mathbf{y}} + p\frac{\pi}{a}\hat{\mathbf{z}}$, where n, m, p are integers). The result is that the scattering from an antiferromagnetically ordered system will show up as peaks at half integer miller indices in the reciprocal space. A ferromagnetically ordered system's unit cell resembles the structural, and so \mathbf{Q} is positioned in the Brillouin zone center ($Q = 0$). Therefore, ferromagnetic Bragg peaks are typically at the same positions as the structural Bragg peaks.

In systems where only short range order is possible, magnetic Bragg peaks will not form. Instead periodic oscillating scattering in reciprocal space will show up, and it will have a periodicity of the reciprocal length scale of the ordering system. In the following, the general (elastic and inelastic) scattering rules for magnetic systems will be shown.

The inelastic neutron scattering processes will change the magnetic quantum system from an initial state, $|\lambda_i\rangle$ with energy E_i into a final state $|\lambda_f\rangle$ with energy E_f . The total magnetic partial differential cross section must be dependent on the summed probability of scattering between all quantum states with a given neutron energy transfer $\hbar\omega$.

The total magnetic neutron scattering cross section can be written [33]

$$\left. \frac{d^2\sigma}{d\Omega dE} \right|_{\text{magn.}} = e^{-2W} (\gamma r_0)^2 \frac{k_f}{k_i} \left[\frac{g}{2} F_m(\mathbf{q}) \right]^2 S(\mathbf{q}, \omega). \quad (5.35)$$

The unitless constant $\gamma = 1.913$ comes from the relation between the nuclear magneton $\mu_N = \mu_B \frac{m_e}{m_p}$, and the magnetic moment of the neutron μ_n . $\frac{m_e}{m_p}$ is the ratio between the mass of the electron and proton. $r_0 = e^2\mu_0/(4\pi m_e)$ is the classical radius of the electron.

The magnetic form factor $F_m(\mathbf{q})$ describes the magnetic scattering from a single ion. The magnetic form factor will be the summed scattering from the unpaired electron distribution around the nucleus. The magnetic form factor is given as the Fourier transform of the normalized spin density $s(\mathbf{r})$

$$F_m(\mathbf{q}) = \int e^{i\mathbf{q} \cdot \mathbf{r}} s(\mathbf{r}) d^3r, \quad (5.36)$$

where r is the displacement of the unpaired electron from the center of the atom. The magnetic form factor is different for every magnetic ion but always approach 1 at small \mathbf{q} and decays smoothly to zero towards large \mathbf{q} .

The magnetic structure factor is given by

$$S(\mathbf{q}, \omega) = \sum_{\alpha, \beta} \left(\delta_{\alpha, \beta} - \frac{q_\alpha q_\beta}{q^2} \right) S^{\alpha\beta}(\mathbf{q}, \omega), \quad (5.37)$$

where $\alpha, \beta = x, y, z$. $S^{\alpha\beta}(\mathbf{q}, \omega)$ is sometimes called the dynamic correlation function and is given by [36]

$$S^{\alpha\beta}(\mathbf{q}, \omega) = \sum_{\lambda_i, \lambda_f} p_{\lambda_i} \langle \lambda_i | \mathbf{V}_\beta^\dagger | \lambda_f \rangle \langle \lambda_f | \mathbf{V}_\alpha | \lambda_i \rangle \delta(\hbar\omega + E_i - E_f), \quad (5.38)$$

where λ_i and λ_f are the magnetic quantum states of the sample, with energy E_i and E_f and p_{λ_i} is the probability of the system is in λ_i state. \mathbf{V}_α and \mathbf{V}_β are the Fourier transform of the spin operator s_j^α in the α -direction.

$$\mathbf{V}_\alpha = \sum_j e^{-i\mathbf{q} \cdot \mathbf{r}_j} \hat{\mathbf{S}}_j^\alpha, \quad (5.39)$$

where \mathbf{r}_j represents the position of the j ion.

It can be shown that neutrons only sense the part of the magnetic moment that is perpendicular to the neutron scattering vector \mathbf{q} [33]. The factor $\left(\delta_{\alpha,\beta} - \frac{q_\alpha q_\beta}{q^2}\right)$ includes this in the magnetic cross section.

Usually, only the $S^{xx}(\mathbf{q}, \omega)$, $S^{yy}(\mathbf{q}, \omega)$, and $S^{zz}(\mathbf{q}, \omega)$ terms contribute to equation (5.35), the rest of the terms will sum to zero [32], and therefore I can write that

$$S(\mathbf{q}, \omega) = \sum_\alpha \left(1 - \frac{q_\alpha^2}{q^2}\right) S^{\alpha\alpha}(\mathbf{q}, \omega). \quad (5.40)$$

Due to the custom that the applied field is usually applied along the z-direction, the term $S^{zz}(\mathbf{q}, \omega)$ is called the longitudinal correlation function, whereas $S^{xx}(\mathbf{q}, \omega)$ and $S^{yy}(\mathbf{q}, \omega)$ are called the transverse correlation functions. There is no preferred direction for Heisenberg spin model in zero field, so [36]

$$S^{xx}(\mathbf{q}, \omega) = S^{yy}(\mathbf{q}, \omega) = S^{zz}(\mathbf{q}, \omega). \quad (5.41)$$

When a field is applied, the spin symmetry breaks down, and equation (5.41) can no longer be assumed to be valid. Instead, the transverse correlation functions have to be calculated individually by using [36]

$$S^{xx}(\mathbf{q}, \omega) = S^{yy}(\mathbf{q}, \omega) = \frac{1}{4} [S^{+-}(\mathbf{q}, \omega) + S^{-+}(\mathbf{q}, \omega)], \quad (5.42)$$

where

$$\begin{aligned} S^{+-}(\mathbf{q}, \omega) &= \sum_{\lambda_i, \lambda_f} p_{\lambda_i} |\langle \lambda_f, m_i - 1 | \mathbf{V}_- | \lambda_i, m_i \rangle|^2 \delta(\hbar\omega + E_i - E_f) \\ S^{-+}(\mathbf{q}, \omega) &= \sum_{\lambda_i, \lambda_f} p_{\lambda_i} |\langle \lambda_f, m_i + 1 | \mathbf{V}_+ | \lambda_i, m_i \rangle|^2 \delta(\hbar\omega + E_i - E_f), \end{aligned} \quad (5.43)$$

where $\langle \lambda_f, m_i \pm 1 |$ indicates that the sum across λ_f only needs to be taken for λ_f in the magnetization subspace $m_i \pm 1$, where m_i is the magnetization subspace of λ_i . This is due to the properties of the raising and lowering spin operators in \mathbf{V}_- and \mathbf{V}_+

$$\begin{aligned} \mathbf{V}_+ &= \sum_j e^{-i\mathbf{q} \cdot \mathbf{r}_j} \hat{\mathbf{S}}_j^+ \\ \mathbf{V}_- &= \sum_j e^{-i\mathbf{q} \cdot \mathbf{r}_j} \hat{\mathbf{S}}_j^-, \end{aligned} \quad (5.44)$$

which when applied to λ_i creates a state in the $m_i \pm 1$ subspace.

The total magnetic cross section σ_{mag} can be estimated from integrating the magnetic partial

differential scattering cross section from equation (5.35) with respect to energy and solid angle. By assuming elastic scattering $k_i = k_f$, that $T = 0$ K and thereby $e^{-2W} = 1$, and $F_m(q) = 1$, the elastic magnetic cross section can be assumed to be

$$\sigma_{\text{mag}} \approx 4\pi \left(\gamma r_0 \frac{g}{2} \right)^2 \int \sum_q \sum_{\alpha, \beta} \left(\delta_{\alpha, \beta} - \frac{q_\alpha q_\beta}{q^2} \right) S^{\alpha\beta}(\mathbf{q}, \omega) d\omega. \quad (5.45)$$

According to equation (5.41), and since all elements with $\alpha \neq \beta$ will sum to zero, the following is valid when the cross section is measured in zero applied field

$$\sum_{\alpha, \beta} \left(\delta_{\alpha, \beta} - \frac{q_\alpha q_\beta}{q^2} \right) S^{\alpha\beta}(\mathbf{q}, \omega) = \left(3 - \left(\frac{q_x^2}{q^2} + \frac{q_y^2}{q^2} + \frac{q_z^2}{q^2} \right) \right) S^{zz}(\mathbf{q}, \omega) = 2S^{zz}(\mathbf{q}, \omega). \quad (5.46)$$

With my definition of the dynamical structure factor, given in equation (5.38), the sum rule reveals [37]

$$\int \sum_q \sum_{\alpha, \beta} S^{\alpha\beta}(\mathbf{q}, \omega) d\omega = 3 \int \sum_q \sum_{\alpha, \beta} S^{zz}(\mathbf{q}, \omega) d\omega = NS(S+1), \quad (5.47)$$

where N is the number of ions in the magnetic unit cell. An energy and \mathbf{q} integrated magnetic cross section can be deduced from combining equation (5.45), (5.46), and (5.47). For a $S = 1/2$ system, with $g \approx 2$, the total magnetic cross section is

$$\sigma_{\text{mag}} \approx 2\pi(\gamma r_0)^2 N. \quad (5.48)$$

5.5 Polarization analysis

Polarization analysis is used to separate magnetic, nuclear coherent, and nuclear spin incoherent scattering. This section will introduce the concept of polarization analysis.

A polarized neutron beam is a beam where all (or almost all) neutron spins are pointing along the same direction, commonly defining to be along the z -axis [32]. Neutron spins can then either be parallel to the polarization direction, called spin up and denoted \uparrow , or anti parallel, called spin down and denoted \downarrow . Different scattering process will affect the spin of the neutron differently. The neutron spin direction before and after the samples therefore needs to be measured. This leaves us with 4 kind of differential neutron spin state cross sections to measure [32]:

$$\left(\frac{d\sigma_{\uparrow \rightarrow \uparrow}}{d\Omega} \right) \quad \left(\frac{d\sigma_{\uparrow \rightarrow \downarrow}}{d\Omega} \right) \quad \left(\frac{d\sigma_{\downarrow \rightarrow \uparrow}}{d\Omega} \right) \quad \left(\frac{d\sigma_{\downarrow \rightarrow \downarrow}}{d\Omega} \right). \quad (5.49)$$

$\uparrow \rightarrow \uparrow$ denotes that the polarization direction is \uparrow before and after the scattering. The spin direction is conserved in $\uparrow \rightarrow \uparrow$ and $\downarrow \rightarrow \downarrow$, and so this type of scattering is called *Non Spin Flip* (NSF) scattering. Opposite this is the *Spin Flip* (SF) scattering, where the spin direction is change, as in $\uparrow \rightarrow \downarrow$ and $\downarrow \rightarrow \uparrow$. The total differential scattering cross section can therefore be written

$$\left(\frac{d\sigma}{d\Omega} \right) = \left(\frac{d\sigma_{\text{NSF}}}{d\Omega} \right) + \left(\frac{d\sigma_{\text{SF}}}{d\Omega} \right). \quad (5.50)$$

The polarization vector \mathbf{P} is a measure of how many spin up and spin down neutrons are detected, and along the z -direction $P = 2f - 1$, where f is the fraction of spin up and down. So all neutrons

have spins pointing down if $P = -1$, and all neutron have spins pointing up if $P = 1$.

To separate the magnetic, nuclear spin incoherent, and nuclear coherent scattering a *XYZ polarization analysis* can be done. In XYZ polarization analysis, the polarization alternates between the three orthogonal directions $\hat{\mathbf{x}}$, $\hat{\mathbf{y}}$, and $\hat{\mathbf{z}}$, while still measuring all 4 different cross sections, from equation (5.49), for each direction. I will in the following paragraphs introduce the principle behind XYZ polarization analysis based on [38].

The total scattering from a system can be written in terms of

$$\left(\frac{d\sigma}{d\Omega}\right)_{\text{tot}} = \left(\left(\frac{d\sigma}{d\Omega}\right)_{\text{coh}} + \left(\frac{d\sigma}{d\Omega}\right)_{\text{incoh}}^{\text{isotope}}\right) + \left(\frac{d\sigma}{d\Omega}\right)_{\text{incoh}}^{\text{spin}} + \left(\frac{d\sigma}{d\Omega}\right)_{\text{mag}} \quad (5.51)$$

$$= N + I + M, \quad (5.52)$$

where N stands for nuclear coherent, I for spin incoherent and M for magnetic scattering.

Nuclear scattering is polarization independent, and the spin orientation of the spin are conserved so that

$$\left(\frac{d\sigma_{\text{NSF}}}{d\Omega}\right)_{\text{coh}}^{(\alpha)} = N \quad \text{and} \quad \left(\frac{d\sigma_{\text{SF}}}{d\Omega}\right)_{\text{coh}}^{(\alpha)} = 0, \quad (5.53)$$

where α is the polarization direction.

A spin incoherent scattering process is also polarization independent, but there is 2/3 change of flipping the spin and therefore

$$\left(\frac{d\sigma_{\text{NSF}}}{d\Omega}\right)_{\text{incoh}}^{(\alpha)} = \frac{1}{3}I \quad \text{and} \quad \left(\frac{d\sigma_{\text{SF}}}{d\Omega}\right)_{\text{incoh}}^{(\alpha)} = \frac{2}{3}I. \quad (5.54)$$

The scattering of polarized neutrons due to magnetism is a bit more complicated since the neutrons only scatters of the component of the magnetic moments in the sample perpendicular to \mathbf{q} . The relative difference between NSF and SF scattering in the different Cartesian coordinates is useful to define as

$$p^\alpha = \frac{\left(\frac{d\sigma_{\text{NSF}}}{d\Omega}\right)^{(\alpha)} - \left(\frac{d\sigma_{\text{SF}}}{d\Omega}\right)^{(\alpha)}}{\left(\frac{d\sigma_{\text{NSF}}}{d\Omega}\right)^{(\alpha)} + \left(\frac{d\sigma_{\text{SF}}}{d\Omega}\right)^{(\alpha)}}. \quad (5.55)$$

By assuming that the scattering vector is only in the xy-plane, and defining that the angle between \mathbf{q} and x-axis is ϕ , the above ratios in the three different directions are

$$p^x = -\cos^2(\phi), \quad p^y = -\sin^2(\phi), \quad \text{and} \quad p^z = 1. \quad (5.56)$$

Using what is known about the spin incoherent and the coherent scattering together with the above consideration of magnetic scattering, the three different scattering components M , I , and N can be separated by:

$$\begin{aligned} M &= 2 \left[\left(\frac{d\sigma_{\text{SF}}}{d\Omega}\right)^{(x)} + \left(\frac{d\sigma_{\text{SF}}}{d\Omega}\right)^{(y)} - 2 \left(\frac{d\sigma_{\text{SF}}}{d\Omega}\right)^{(z)} \right], \\ N &= \frac{1}{6} \left[2 \left(\frac{d\sigma_{\text{NSF}}}{d\Omega}\right)^{(x)} - \left(\frac{d\sigma_{\text{SF}}}{d\Omega}\right)^{(x)} + 2 \left(\frac{d\sigma_{\text{NSF}}}{d\Omega}\right)^{(y)} - \left(\frac{d\sigma_{\text{SF}}}{d\Omega}\right)^{(y)} + 2 \left(\frac{d\sigma_{\text{NSF}}}{d\Omega}\right)^{(z)} - \left(\frac{d\sigma_{\text{SF}}}{d\Omega}\right)^{(z)} \right], \\ I &= \frac{3}{2} \left[3 \left(\frac{d\sigma_{\text{SF}}}{d\Omega}\right)^{(z)} - \left(\frac{d\sigma_{\text{SF}}}{d\Omega}\right)^{(y)} - \left(\frac{d\sigma_{\text{SF}}}{d\Omega}\right)^{(x)} \right]. \end{aligned}$$

A useful property of ferromagnetic scattering is that when applying an external field to a ferromagnetic sample perpendicular to the scattering plane, and parallel to \mathbf{P} , only NSF scattering occurs. In this configuration the NSF scattering from a ferromagnet is, however, not the same for initial neutron spin being \uparrow or \downarrow . In some alloys with ferromagnetic ordering, the relation is such that almost only spin pointing parallel (or in other alloys anti parallel) will scatter. These kind of alloys can be used as polarizers to generate an almost fully polarized beam (ie $P_z = \pm 1$).

5.6 Neutron instruments

Two types of neutron sources exist at large scale facilities: Reactor sources, which utilize the excess neutrons from a fission process to create free neutrons, and spallation sources that use the neutrons created when an accelerated proton beam hits a target material.

Both processes result in high energy neutrons, and in order to slow neutrons down to thermal energies, $1 \text{ meV} < E < 1 \text{ eV}$, which is a necessity for neutron scattering, neutron moderators are used. When neutrons scatter off an atom's nucleus, they will loose some of their energy to the nucleus. In moderators successive scattering is used to slow the neutrons. A good moderator needs to have a large scattering cross section, and a low absorption cross section. Hydrogen possess this property, hence it is a very effective moderator. Liquid water (H_2O) is the most common moderator for thermal neutrons. To achieve cold neutrons (with energies below $\sim 10 - 15 \text{ meV}$), colder moderators are needed. Such moderators use liquid hydrogen H_2 with a temperature of 30 K .

Neutron guides are used to transport the neutrons from the source to the neutron scattering instruments. Guides are tubes where the walls are coated with layers of materials which reflect neutrons under a certain incoming critical angle. The critical angle of the material increase with increasing wavelength, and the loss of neutrons therefore decrease with increasing wavelength [33]. The neutron beam will have a broad distribution of wavelengths when exiting the guide, and so it is typically called a white neutron beam, as a reference to white light. In a Laue diffraction instrument, the white beam is emitted directly on to the sample, and detectors are placed around the sample to detect the scattered neutrons. Crystal symmetries can be identified from Laue diffraction, but to detect structures and dynamics of the system, the neutron wavelength needs to be separated and identified. The rest of this section will describe the instrument used to measure the Boleite crystals. The neutron scattering instruments used can be separated into three different types; triple axis spectrometers (RITA-II, IN3, IN8), the time-of-flight spectrometer IN4, and the polarized neutron diffractometer D7.

5.6.1 Triple axis spectrometers

As the name insinuates, a triple axis spectrometer uses three scattering axes to determine initial and final energy E_i and E_f , and scattering vectors k_i and k_f . The sample constitutes the second axis of the spectrometer, whereas the first and third are the so called monochromator and analyzer. The basic layout of a triple axis spectrometer is shown in figure 5.4.

A monochromator is built from single crystals and uses Bragg scattering from one or more crystals to scatter a neutron beam towards the sample. Following Bragg's law (equation (5.31)), only a specific set of wavelengths will scatter in the direction of the sample at a certain spacing between

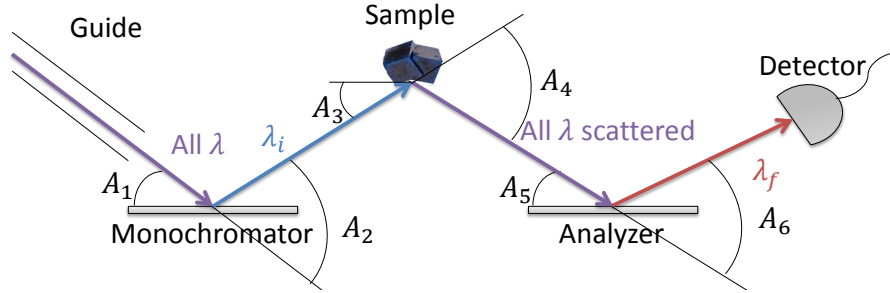


Figure 5.4: Basic layout of triple axis spectrometers. The white neutron beam ("All λ ") from the guide is monochromated by the monochromator which scatters neutrons with wavelength λ_i towards the sample. The neutrons are scattered elastically and inelastically at the sample ("All λ scattered"). An analyzer monochromates the neutrons from the sample and scatters neutrons with wavelength λ_f towards the detector. Scattering vectors \mathbf{k}_i and \mathbf{k}_f can be found and changed by controlling the angles in the system. Scattering angles (A_n , with $n = [1, 6]$) are explained in the main text.

crystal planes. The spacing depends on the monochromator's crystals orientation. The monochromators rotation around its own axis is defined as A_1 , and $A_1 = 0$ is when the monochromator is parallel to the incoming neutron beam. The rotation of the sample arm around the monochromator compared to the incoming beam is usually called A_2 , and to fulfill the Bragg condition $A_2 = 2A_1$ is used.

At the sample, the neutrons will scatter in directions depending on the sample structure. Depending on the dynamics of the sample, the neutrons can also experience inelastic scattering. The sample can be rotated with angle A_3 around itself on an axis perpendicular to the scattering plane. The arm heading towards the analyzer, called A_4 , can likewise be changed.

It would not be possible to determine the outgoing energy of the neutrons if the detector was placed at the analyzers position. An analyzer is the same as a monochromator, but its purpose is to determine the outgoing energy of the neutrons. The analyzer can like the monochromator rotate around its own axis, with an angle A_5 , and the detector is placed in an angle A_6 from the analyzer.

We have used three different triple axis spectrometers to measure boleite. The thermal triple axis spectrometers IN8 and IN3 at ILL, and the cold triple axis spectrometers RITA-II at PSI.

IN3 is a classical triple axis, as described above, whereas RITA-II and IN8 both used multi analyzer settings. Multi analyzers consist of a series of analyzers and a multi array detector bank as illustrated in figure 5.5. This is done to cover multiple A_4 directions at one time. RITA-II uses 9 analyzers, which is typically rotated to scatter a fixed k_f , and inelastic experiments are performed by changing k_i . In the boleite experiments on IN8, the Flatcone setting was used. Flatcone is a multi analyzer add-on to ILL triple axis spectrometers. The Flatcone add-on is illustrated in figure 5.6.

5.6.2 Time of flight spectrometer

A time of flight spectrometer uses the time of flight of the neutrons to determine initial and/or final energy of the neutrons. A large range of different methods can be used to determine the

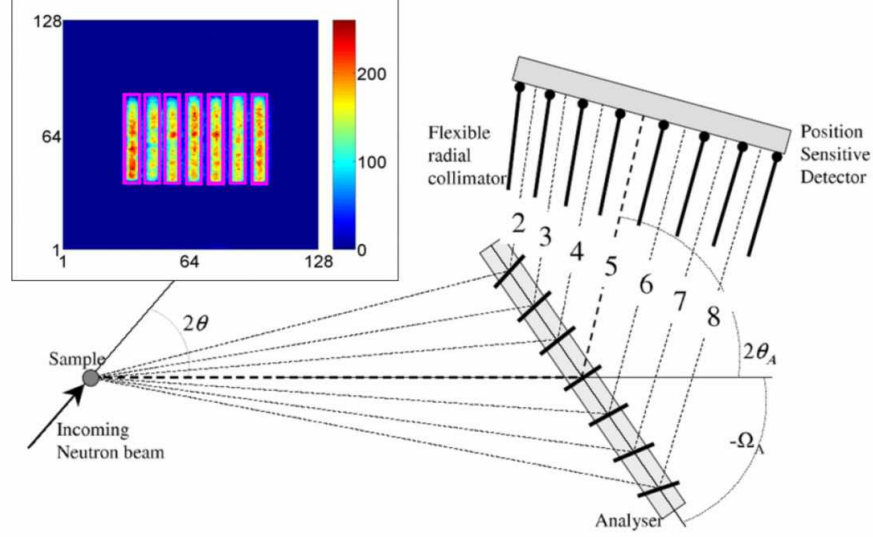


Figure 5.5: The principle behind multi analyser in triple axis spectrometers. The figure shows 7 of the 9 analysers of the RITA-II spectrometer, with an insert of the detector measurements in top left corner [39].

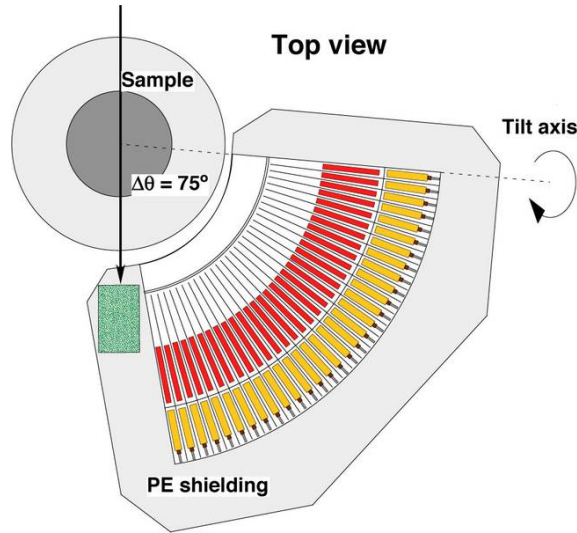


Figure 5.6: The Flatcone design. Flatcone contains 31 pairs of analyser and 31 detectors placed above the analysers. The first analyser in a pair (red area) is set to scatter $k_f = 3 \text{ \AA}^{-1}$, and the second analyser (yellow area) is set to scatter $k_f = 1.5 \text{ \AA}^{-1}$. By using a shutter, one selects whether it is the scattered neutrons from the first or the second analyser which reach the detector [40].

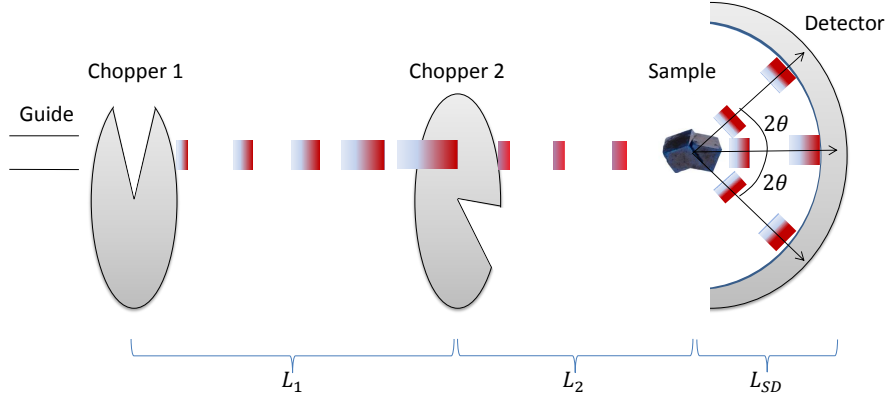


Figure 5.7: Basic layout of ToF spectrometers on a continuous source. Two choppers are used to monochromate the white beam from the guide. The neutrons are illustrated with colored bars, illustrating the spectrum of neutrons in space from cold (blue) to thermal (red). A time and position sensitive detector is used to determine the final energy E_f of the neutron and scattering angle θ .

energy from the time of flight of the neutrons, but they all use some kind of chopper systems. A chopper is a rotating device that at a given frequency opens for neutrons to pass through. The disc chopper is the most basic chopper. It is a rotating disc with slits distributed around its surface. This way the disc chopper allows neutrons through every time a slit passes the neutron beam. A single disc chopper can not alone be used for inelastic experiments as it only creates a pulsed white beam. A series of disc choppers can be used to create a pulse with a narrow wavelength bandwidth, which together with a time sensitive detector make it possible to do inelastic experiments.

A simplified example of how the chopper system works is shown in figure 5.7. Only neutrons with a small energy bandwidth will have the right velocity after the first chopper to travel the distance between the two choppers L_1 , and still arrive at the second chopper when it opens for the neutrons. The beam is in this way monochromated, and initial energy E_i and speed v_i of the neutron is known. The time that the neutron arrives at the sample can be calculated using v_i and knowing the distance L_2 from the second chopper to the sample. The sample is encircled with a time and position sensitive neutron detector, where each detector pixel corresponds to a scattering angle. The final speed v_f and energy E_f of the neutrons after scattering are obtained from the arrival time at the detector, and by knowing that the distance from sample to the detector is L_{SD} . \mathbf{k}_i and \mathbf{k}_f can be determined from the neutron scattering angle and the rotation of the sample.

For our boelite experiments, we used the thermal time of flight spectrometer IN4C at the ILL illustrated in figure 5.8. IN4C covers an energy range of 10-100 meV. IN4C is not a standard time of flight spectrometer as it uses a double curving monochromator to monochromate the beam, and a Fermi chopper to determine the neutron time at the sample, which combined with the time sensitive detector array gives possibility for inelastic experiments. A Fermi chopper is a rotating cylinder containing a collimator inside. In this way the Fermi chopper opening time is dependent

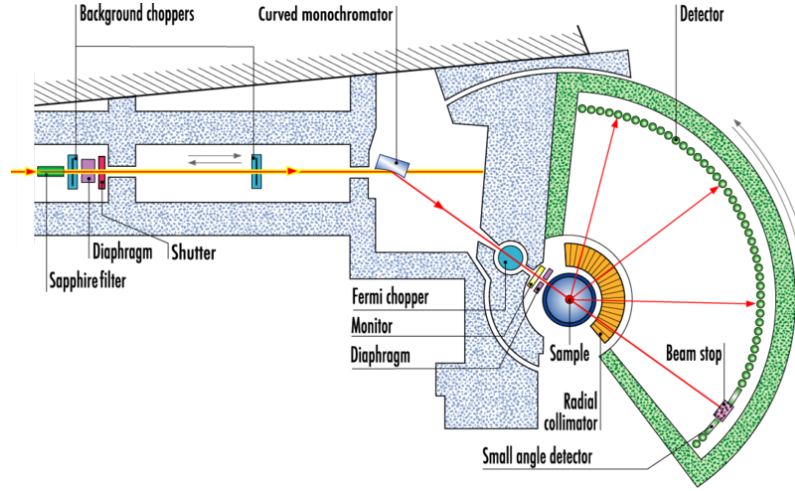


Figure 5.8: IN4C time of flight spectrometer [42].

on the incoming angle of neutrons to the sample, which can be used to increased energy resolution in the so called time focusing technique[‡]. IN4C also has two disc choppers called the background choppers by the ILL. The disc choppers primary purpose is to remove all high energy neutrons and gamma rays [42].

5.6.3 The polarized neutron diffractometer

A neutron polarization analysis diffractometer uses that it is possible to separate the magnetic, nuclear spin incoherent, and nuclear coherent scattering from each other, by using polarization analysis.

Our boleite samples were measure on the polarization analysis spectrometer *D7* at ILL. Figure 5.9 shows *D7*'s instrument layout. The following paragraphs give a short introduction to the components shown in figure 5.9.

D7 uses three monochromators to monochromate the neutron beam. The polarization of the neutrons are achieved with the help of a polarizer. The polarizer used in *D7* is a Schaerpf bender-type supermirror polarizer [43]. This type of polarizer is a multi channel guide with curving walls and coated with polarizing supermirrors. The Schaerpf bender-type supermirror polarizer is constructed in a way that all neutrons will at least be reflected one time or absorbed by the guide walls. To achieve a $P \approx 1$, the supermirrors are coated with an absorbing anti-reflecting layer to avoid neutrons with the wrong spin being transmitted through the polarizers' walls [45].

A guiding field is placed between instrument components to avoid loss of polarization between the polarizer and the sample, and the sample and the detection system. A *flipper*[§] is placed between the sample and the polarizer. A flipper uses a radio frequency field perpendicular to the polarization, and it can thereby change the spin state of the neutrons from $\uparrow \rightarrow \downarrow$ or $\downarrow \rightarrow \uparrow$ [32].

The detector system consists of an array of analyzers and detectors placed around the sample. At

[‡]The time-focusing technique was not used for Boleite, but the interested reader can find more in Hannu Mutka's paper [41].

[§]*D7*'s flipper is a Mezei flipper, which are described in details in reference [46].

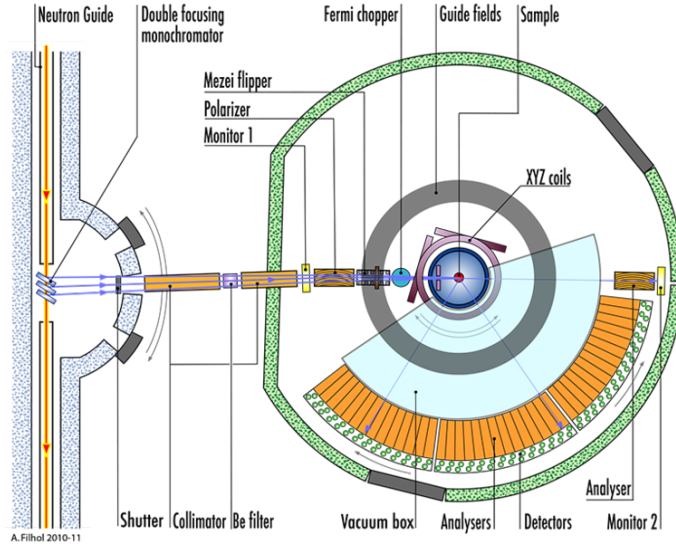


Figure 5.9: D7 polarization analysis spectrometer. The different components are elaborated in the main text [43].

D7, an analyzer consists of a Schaefer bender-type supermirror polarizer which is only allowing spin up through [43].

On D7, the direction of polarization of the neutrons at the sample position is altered between \hat{x} , \hat{y} , and \hat{z} with the help of magnetic fields generated by coils placed around the sample [43]. After scattering off the sample, the neutron polarization direction is change back to the \hat{z} -direction by the guiding fields.

When using XYZ polarization analysis, D7 is set to diffraction mode where only the scattering angle, and not the magnitude of k_f , is measured. This means that XYZ-polarization measurement method on D7 is an energy integrated measurement.

D7 can also be set to spectroscopy mode where it can makes inelastic measurements with the help of its Fermi choppers. It is however not possible to run the spectroscopy mode and separate magnetic, nuclear incoherent, and coherent scattering from each other, and it was therefore not used for our boleite samples.

CHAPTER 6

Boleite

Boleite ($\text{KPb}_{26}\text{Ag}_9\text{Cu}_{24}\text{Cl}_{62}(\text{OH})_{48}$) is a deep blue, natural mineral found all around the world. Large crystals are usually found in mines in Mexico and south western USA. Boleite is usually formed in a reaction of chlorides with sulfides in oxygenated lead-copper-deposits, but it has also been found in smelter slag immersed in seawater [47]. I will in this chapter present the structure of boleite, and introduce its interesting magnetic unit cell.

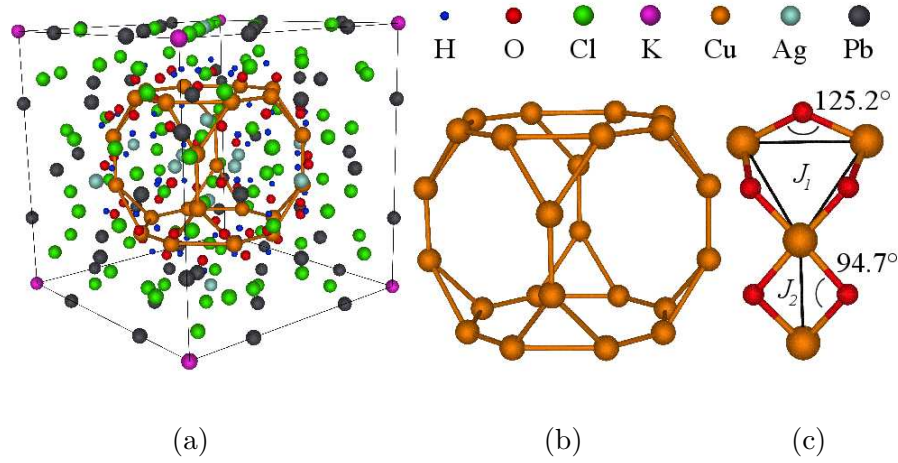


Figure 6.1: Boleite's unit cell in a ball-and-stick model. The legend in the top right shows the atoms' color coding. (a) Full unit cell with all atoms. (b) The copper atoms in the unit cell with couplings shown between them. Notice how the copper cube is isolated in the center of the unit cell. (c) Zoom-in on one corner of the cube, where copper-oxide bonds form intra triangle coupling J_1 and inter triangle coupling J_2 . The figure is contributed by Sonja Holm and presented in reference [7]. The figure is made in VESTA[48] based on numbers from reference [5].

6.1 Properties of boleite

Boleite has a cubic unit cell in the $\text{Pm}\bar{3}\text{m}$ space group with side length $a = 15.288 \text{ \AA}$ [47]. The magnetism in boleite arises from the copper ions* in the center of the unit cell, as figure 6.1a shows. The $24 \text{ Cu}^{2+} S = 1/2$ ions form a truncated cube, with 3 copper ions forming equilateral triangles in each of the 8 corners of the cube, as seen in figure 6.1b. The distance between copper ions in a triangle is 3.48 \AA , and the distance between neighboring triangles is 2.89 \AA . This is too far from each other for direct exchange bonds to occur. Two possible types of super exchange pathways

*Copper is the only transition metal in boleite.

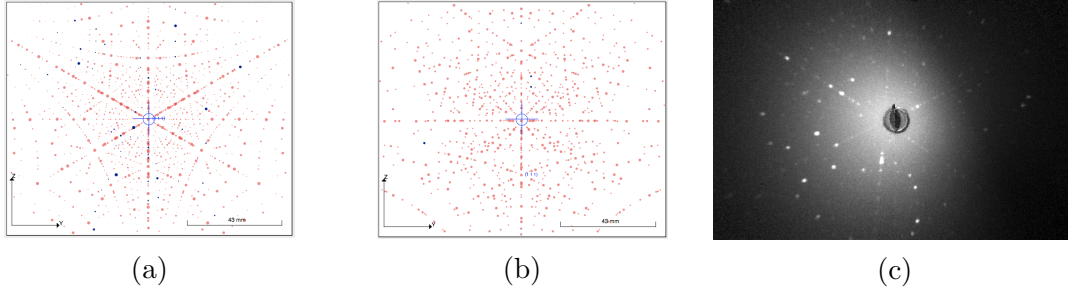


Figure 6.2: X-ray Laue diffraction pattern from boleite and pseudoboleite radiated in the (1 1 1) direction. Theoretical estimates of X-ray Laue diffraction pattern are made in QLaue [50]. The figures were originally presented in reference [6]. (a) Estimated Laue diffraction pattern from boleite. Boleite will in X-ray Laue diffraction measurement have clear peaks in the diagonal. (b) Estimated Laue diffraction pattern from pseudoboleite. Pseudoboleite does not have peaks in the diagonal. (c) Diffraction pattern from crystal F, which shows a diagonal line of peaks and is therefore most likely boleite.

exist in boleite. One is through chloride ions, and the other is through the oxide ions. We believe that the oxide pathway is the most likely of these two possibilities, as the distance between copper and oxide ions is 1.96 \AA compared to the chloride-copper distance of 2.82 \AA [5]. The copper-oxide bonds are different between inter and intra triangle copper ions, as shown in figure 6.1c. Our expectation is that the two types of copper-oxide bonds will create two different antiferromagnetic exchange coupling constants. I will denote the exchange coupling within triangles as J_1 , and the exchange coupling between triangles as J_2 .

The copper cubes in boleite are isolated in the center of the structural unit cell, and the distance between two copper cubes is $\sim 7.5 \text{ \AA}$, which makes possible exchange interaction between neighboring spin cubes negligible. We therefore believe that long range magnetic order can be neglected in boleite, and that the magnetism in boleite arises from the isolated 24 spin cubes clusters. The magnetic structure in boleite is therefore a unique possibility to study a real, and possibly frustrated, finite sized system of 24 spins.

6.1.1 Identifying proper Boleite crystals

Boleite closely resembles the mineral pseudoboleite in appearance, and the two minerals sometimes grow on top of each other [47]. Pseudoboleite has the chemical composition $\text{Pb}_5\text{Cu}_4\text{Cl}_{10}(\text{OH})_8 \cdot 2(\text{H}_2\text{O})$, and it has a tetragonal unit cell in the $I4/mmm$ space group, with side lengths $a = 15.24 \text{ \AA}$ and $b = 30.74 \text{ \AA}$ [49].

Laue diffraction is an easy way to distinguish pseudoboleite from boleite, since the tetragonal unit cell will give a different scattering pattern than the cubic, due to the different symmetries of the unit cell. All crystals used in this project were tested with x-ray Laue diffraction to ensure that they were boleite and not pseudoboleite. X-ray Laue diffraction only probes the surface of the crystal, and it is assumed that the entire crystal is like its surface. Figure 6.2 shows how boleite crystals were identified using X-ray Laue diffraction. The crystals were measured and identified with X-ray Laue diffraction by Sonja Holm and Kenneth Lønæk [6].

6.2 The magnetic susceptibility

A large range of the identified boleite crystals' susceptibilities were measured at a range of different susceptometers. The susceptometers are presented in chapter 4. The experimental details of the different crystals are given in table 6.1.

Type 1 crystals			Type 2 crystals		
Crystal	Mass [mg]	Measured at:	Crystal	Mass [mg]	Measured at:
E	403	PSI PPMS	A	355	PSI PPMS
H	226	PSI MPMS	B	424	PSI PPMS
N	245	PSI MPMS	D	605	PSI PPMS
H1	197.0	EPFL MPMS	F	287	PSI PPMS
E1	137.1	EPFL MPMS	K	263	PSI MPMS
S1	76.4	AU PPMS	P	236	PSI MPMS
E2 ^(†)	21.3	AU PPMS	C1	118.8	EPFL MPMS
			P1	9.1	EPFL MPMS
			M1	84.2	AU PPMS
			O ^(*)	308.9	AU PPMS
			C2 ^(†)	29.9	AU PPMS
			C3 ^(†)	9.9	AU PPMS

Table 6.1: The measured crystals' mass and place of measurement. The definition of the crystal types used in the table are given in the main text. A number in a crystal's name labels that different pieces of the same crystal were measured. The used susceptometers are presented in chapter 4. (*) The susceptibility curve of crystal O was only measured for $T < 20$ K, where it showed a clear type 2 crystal susceptibility kink. (†) The three crystals' susceptibility curves all showed significantly larger offset than all other susceptibility curves.

The susceptibility curves of all crystals from table 6.1, except crystal C2, C3, E2, and O are presented in figure 6.3. The figure shows that most data is very similar for $T > 30$ K. At $T < 30$ K, two different types of susceptibility curves are observed from the boleite crystals. I will define the boleite crystals according to the two types of susceptibility curves:

- **Type 1 crystal:** The susceptibility increases as the temperature is decreased.
- **Type 2 crystal:** The susceptibility increases as the temperature is decreased until a kink around 3 K. After the kink, the susceptibility decreases with decreasing temperature.

The measurements from PSI all seem to be identical at $T > 200$ K. What is not visible in figure 6.3 is that the PPMS data from PSI have much larger errors than the MPMS measurements done at PSI and EPFL. The AU measurements and some of the EPFL measurements have an offset

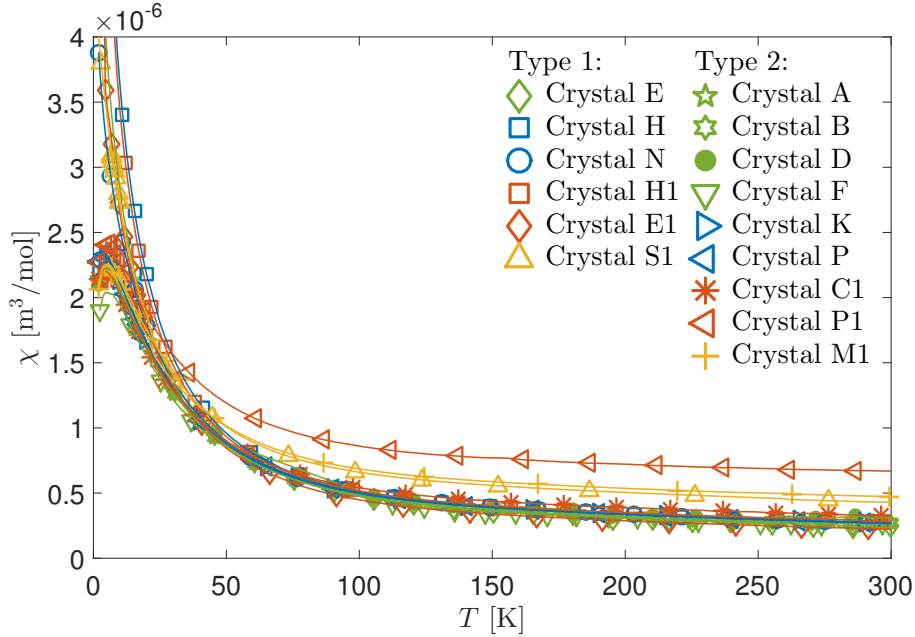


Figure 6.3: The mass normalized magnetic susceptibility from different boleite crystals. Every crystal is given a unique marker (see legend in top right) and every instrument a unique color. The crystals were measured at PSI PPMS (green), PSI MPMS (blue), EPFL MPMS (red), and AU PPMS (Yellow). The crystal properties are given in table 6.1.

compared to the PSI MPMS and PPMS data. The EPFL and AU measurements' offsets are not self consistent, in the sense that the measurements are not alike at high temperatures. Due to the above considerations, only the 4 PSI MPMS measurements are used to test the different susceptibility models in this and the next chapter.

The MPMS data from PSI is consistent when separated into the two types. In figure 6.4, the inverse susceptibility of crystal K (type 2) and H (type 1) obtained at MPMS at PSI is shown as an example. There are two distinct kinks seen in the inverse susceptibility of type 2 crystals, one at $T \approx 130$ K and one at $T \approx 3$ K. For type 1 crystals there is only a kink at $T \approx 130$ K. Since we assume that boleite has two exchange constants, our initial guess is that the data will have two transition temperatures, where the small spin systems, like the 8 spin triangle, are frozen into their ground state(s).

I will denote the transition temperatures of J_1 and J_2 as T_1 and T_2 respectively. An inverse susceptibility curve from a system with two transition temperatures can be expected to have two kinks. This is the case for the type 2 crystals' susceptibility curves.

The large temperature difference between the two kinks indicates a large difference in exchange coupling strength. The origin of the missing kink in the type 1 crystals' inverse susceptibility could very well be impurities. The impurities could create imperfect cubes with free spins. The paramagnetic behavior of the free spins could dominate the susceptibility curves, so that low temperature kinks were hidden beneath the paramagnetic contribution. This hypothesis is tested in the next chapter.

The two straight parts of the inverse susceptibility curve from crystal K and P are fitted with Curie Weiss lines (equation (4.6)), as shown in figure 6.4. The Curie Weiss line fitted to the high temperature region has a Curie Weiss temperature $\Theta_{CW,H} = -195 \pm 6$ K, and the fit to the low temperature region has $\Theta_{CW,L} = -10.4 \pm 0.2$ K. This indicates that both exchange constants give rise to antiferromagnetic coupling, since $\Theta_{CW} < 0$ K for both fits. We expect that the spins at the high temperature kink in the inverse susceptibility order due to either J_2 or J_1 , and thereby either are forming isolated dimers or trimers. As the thermal energy decreases with temperature, the weaker of the two exchange constant forces the entire 24 spin cube cluster to order.

An antiferromagnetic triangle will, as explained in chapter 3, behave like a paramagnet at temperature lower than the transition temperature with $1/\chi \rightarrow 0$ for $T \rightarrow 0$ K, due to its degenerate ground state. Unlike this, A spin dimer has a singlet ground state, and therefore $1/\chi \rightarrow \infty$ for $T \rightarrow 0$ below the transition temperature, for an external field parallel to the spin direction.

In figure 6.4 a paramagnetic like behavior is observed in the inverse susceptibility at temperatures below the first kink. This indicates that J_1 is much stronger than J_2 ; hence, the system will behave like 8 isolated trimers for $T \gg T_2$. As the thermal energy approaches the scale of J_2 , the 8 trimers orders into 24 spin states. The system can therefore be viewed as being in three different stages:

At $T \gg T_1$ all spins behave paramagnetically. As the temperature is lowered, the intermediate region $T_2 < T < T_1$ is reached. Here the spins behave as a cooperative paramagnet, since the spins are bound in the degenerate trimer ground states. At $T < T_2$, the entire 24 spin system orders.

The summed contribution from the coupling constants can as an approximation be estimated from equation (4.3), by assuming that $-\Theta_{CW} = T_N$. Following the interpretation from above, a Curie Weiss fit to the intermediate temperature ($T_2 < T < T_1$) susceptibility should be expected to give a Curie Weiss temperature solely dependent on J_2 coupling the 8 spin triangles. At $T > T_1$ both J_1 and J_2 will contribute, and so

$$\begin{aligned} \sum_{J_2,i} J_i &= -4k_B \Theta_{CW,L}, \\ \sum_{\text{All},i} J_i &= -4k_B \Theta_{CW,H}, \end{aligned} \quad (6.1)$$

where the sums are taken across all neighbors ($\sum_{\text{All},i}$) or all J_2 neighbors ($\sum_{J_2,i}$). Every spin has 2 J_1 neighbors and 1 J_2 neighbor and so

$$\begin{aligned} J_1 &= \frac{\sum_{\text{All},i} J_i - J_2}{2}, \\ J_2 &= \sum_{J_2,i} J_i. \end{aligned} \quad (6.2)$$

Using this assumption the first estimate of the coupling strengths are

$$\begin{aligned} J_1 &= 36 \pm 2 \text{ meV}, \\ J_2 &= 3.6 \pm 0.1 \text{ meV}. \end{aligned} \quad (6.3)$$

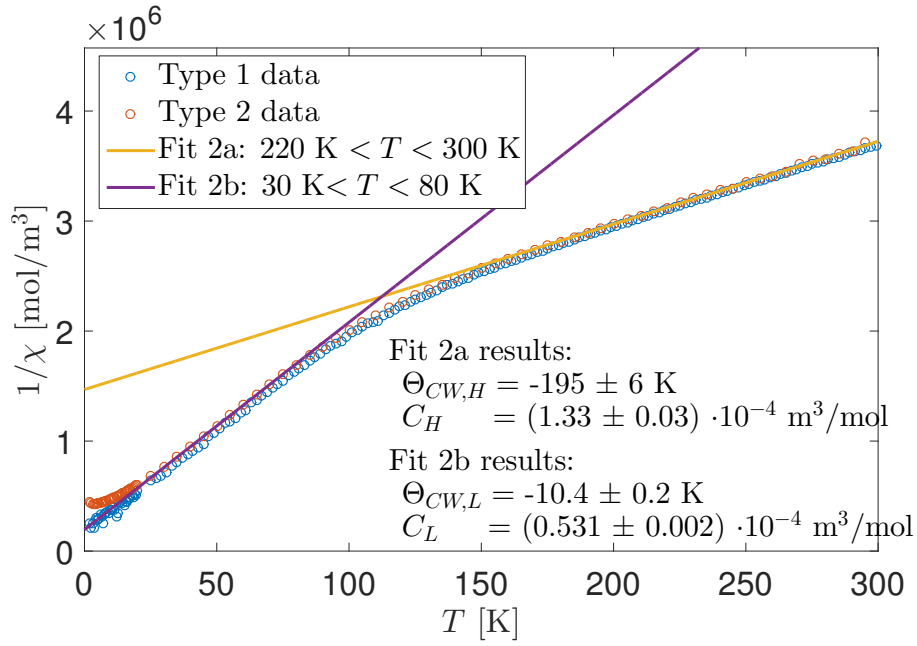


Figure 6.4: The inverse susceptibility from different boleite crystals, measured at the MPMS at PSI. The inverse susceptibility is separated into two categories. Type 1 data is from the two type 1 crystals, H. Type 2 data is from the type 2 crystal K. The type 2 data is fitted with two Curie Weiss lines, from equation (4.6). The legends show the fit boundary (top left) and the fit parameters (bottom right).

CHAPTER 7

Modeling the susceptibility

A quantum mechanical $S = 1/2$ spin model is needed to fully understand the magnetic structures in boleite. It is reasonable to construct the model based on the susceptibility data, since it constitute the largest amount of data with a clear indication of magnetism. All eigenenergies of a system need to be found in order to model the susceptibility, according to equation (4.8).

To calculate all eigenenergies of the boleite system, a matrix of size $2^{24} \times 2^{24}$ needs to be diagonalized. Even though the matrix can be block diagonalized using magnetization and geometric symmetries, the largest matrices still have a size of $\sim 2^{19} \times 2^{19} = 2.7 \cdot 10^{11}$. This is beyond the limitations of complete diagonalization routines, and one has to make an approximative system of less spins, or use other approximations to find the eigenenergies.

This chapter will show the result of complete diagonalization of smaller spin systems (≤ 12 spins), before presenting approximative models of the full 24 spin system.

7.1 Simple models

Kenneth Lønþæk investigated the boleite system in his bachelor thesis [6]. In his thesis, Kenneth made exact calculations of eigenvalues of a triangle of spins and a 6 spin system, like the models shown in figure 7.1(a-b). The eigenvalues of the 6 spin model are shown in appendix A, and the eigenvalues of the triangle model are shown in table 3.1. The theoretical susceptibility of an antiferromagnetic system can be calculated from its eigenvalues using equation (4.9). The theoretical susceptibility models are afterwards fitted to the raw data from a type 2 boleite crystal by adjusting the exchange constants and multiplying a scaling parameter χ_0 .

Figure 7.2 presents such a fit, showing that the 6 spin model and the triangle model are alike at high temperatures, and that both are able to account for the kink in observed crystal data at ~ 130 K. The 6 spin model adds a kink in the susceptibility model at low temperatures compared to the triangle model. Due to this kink, the 6 spin model resembles the data better than the triangle model, as also seen from the reduced chi-square χ_{Red}^2 of the fits to the data at $T > 3$ K, which for the triangle model and 6 spin model are $\chi_{\text{Red}}^2 = 4.7 \cdot 10^6$ and $\chi_{\text{Red}}^2 = 2.7 \cdot 10^6$ respectively. The two models predict almost the same value of J_1 . The 6 spin model fit has $J_1 = 24.5 \pm 0.2$ meV and $J_2 = 1.8 \pm 0.1$ meV, and the triangle model has $J_1 = 24.6 \pm 0.2$ meV.

The exchange constants predicted by the 6 spin model and triangle model are significantly different to the exchange constants found by the Curie Weiss models, shown in equation (6.2). This difference is investigated in the end of this chapter.

The behavior of the 6 spin model is consistent with the expectations of the boleite system from chapter 6, where it was predicted that the susceptibility curve could be separated into three temperature regions: One where the spins behave freely, another where the spins are bound in triangle ground states, and a third where the coupling between the triangles forces the entire 24 spin to order into a collective state.

The 6 spin model shows similar behavior as the measured crystals' susceptibility curve but does not fit it completely. Four out of six spin sites in the 6 spin model, shown in figure 7.1b, are only

coupled to neighbors through the J_1 exchange constant. This is very different from the real boleite system, where all spin sites are coupled to two neighbors through J_1 and one through J_2 . To make a bigger spin model which resembles boleite better, a computer routine is needed.

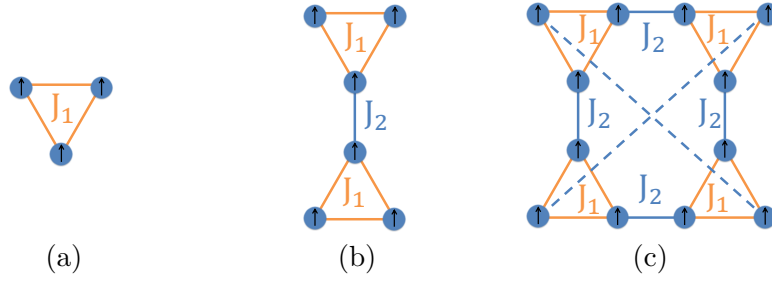


Figure 7.1: The model spin systems. The spins (colored circles) are positioned in the corner of the triangles. The coupling strengths between sites are shown with colored lines, with similarly colored labels (J_1 and J_2). (a) The spin triangle model. (b) The 6 spin model with two coupled spin triangles. (c) The 12 spin model with periodic boundary conditions. The spins in the corners of the system are coupled with J_2 to their cross diagonal counterpart (dashed lines).

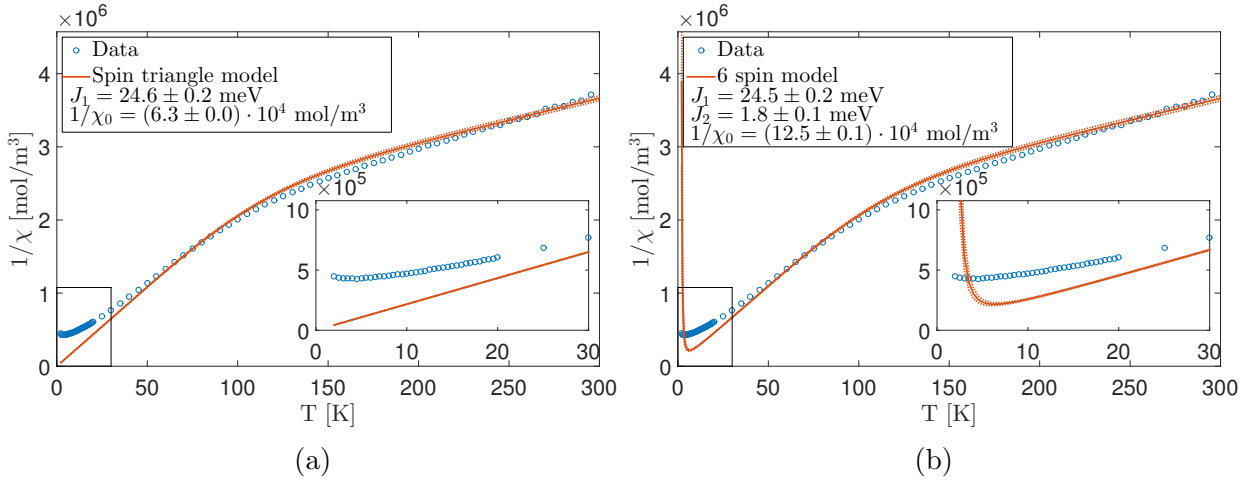


Figure 7.2: The inverse susceptibility from the type 2 boleite crystal K compared to the susceptibility predicted by the triangle model (a) and the 6 spin model (b). The dashed lines illustrates the upper and lower bound of the exchange constants. The models are presented in the main text. The fit parameters are given in the legends. The reduced chi-square of the fits to the data at $T > 3$ K are for the triangle model $\chi_{\text{Red}}^2 = 4.7 \cdot 10^6$ and for the 6 spin model $\chi_{\text{Red}}^2 = 2.7 \cdot 10^6$. The large χ_{Red}^2 is discussed later in this chapter.

7.2 Mexact

A primitive version of RLexact (RLexact was described in chapter 3) complete diagonalization algorithm was made in Matlab to efficiently calculate the susceptibility of a small $S = 1/2$ system with multiple exchange constants. I will call this algorithm for *Mexact*.

As it is the case with RLexact, Mexact uses the Ising basis to find the eigenstates of the Heisenberg Hamiltonian's interaction term $\hat{\mathcal{H}}_I$ (equation (2.19)) for a given spin system. The individual spin's spin eigenstate is in Mexact labeled with 0 or 1, where 0 and 1 corresponds to a spin up state ($m_S = +1/2$) and a spin down state ($m_S = -1/2$) respectively. An Ising state of the full system is then written as a series of ones and zeros. As an example, the 4 spin square lattice system basis state $|\psi_i\rangle = |1001\rangle$, labels that spin 1 and 4 points up, and spin 2 and 3 points down.

It is easy to translate $|1001\rangle$ into a binary number. In a system with N spins, any unique configuration of Ising spins can be translated into a unique binary number between 1 and 2^N , where any binary number is a unique spin configuration. Mexact first writes all states, then identifies their magnetization, and then sorts states according to it.

Mexact uses time reversal symmetry and block diagonalization. For every m -subspace the Hamiltonian is written into its matrix form $\hat{\mathcal{H}}_m$, by computing all elements $\langle\psi_j|\hat{\mathcal{H}}_I|\psi_i\rangle$, where i and j run across all Ising basis vectors in the subspace. Applying $\hat{\mathcal{H}}_I$ to an Ising state will result in a superposition of different Ising states

$$\hat{\mathcal{H}}_I|\psi_i\rangle = \sum_j^N c_i|\psi_j\rangle, \quad (7.1)$$

where N is the number of Ising states in the given subspace. Mexact uses that all Ising states are orthogonal and normalized so that $\langle\psi_j|\psi_i\rangle = \delta_{i,j}$. By identifying all non-zero c_i , all non-zero elements $\langle\psi_j|\hat{\mathcal{H}}_I|\psi_i\rangle$ are identified for every state $|\psi_i\rangle$.

As an example, lets take a quick look at the result from applying the Heisenberg Hamiltonian's interaction term $\hat{\mathcal{H}}_I$ to the $m = 0$ state $|1001\rangle$, for nearest neighbor exchange constant J :

$$\hat{\mathcal{H}}_I|1001\rangle = \frac{J}{2} (|0101\rangle + |1010\rangle). \quad (7.2)$$

This shows that the matrix elements $\langle 1010|\hat{\mathcal{H}}_I|1001\rangle$ and $\langle 0101|\hat{\mathcal{H}}_I|1001\rangle$ will be $\frac{J}{2}$. By repeating this for all states with $m = 0$, the full matrix $\hat{\mathcal{H}}_{m=0}$ is identified. Afterwards Mexact uses Matlab's eig-function to diagonalize $\hat{\mathcal{H}}_{m=0}$.

Mexact's validity was tested on a range of small spin systems. The results were compared to the results from RLexact, and the results presented by Haraldsen [3]. All tests showed a complete correspondence between the two algorithms and Haraldsen. Mexact is therefore assumed to find the correct eigenvalues of a spin system.

The largest, boleite resembling spin system that can be diagonalized using Mexact is a 12 spin system with periodic boundary conditions, as illustrated in figure 7.1c. The periodic boundary conditions are made such that all triangles are directly coupled through J_2 to each of the 3 other triangles. Using Mexact, all eigenvalues are found for the 12 spin model. The susceptibility is afterwards calculated from the eigenvalues using equation (4.9), and fitted to the data by adjusting the exchange constants and multiplying a scaling parameter χ_0 .

In figure 7.3, the result from fitting the 12 spin model is shown. The best fit of the 12 spin model

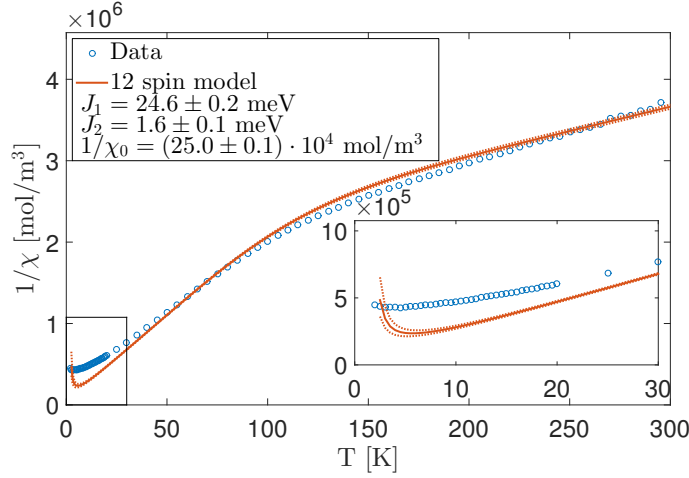


Figure 7.3: The inverse susceptibility from the type 2 boelite crystal K compared to the susceptibility predicted from the Mexact result for the 12 spin model. The dashed lines illustrates the upper and lower bound of the exchange constants. The model is presented in the main text. The fit parameters are given in the legends. The fit to the data at $T > 3$ K has $\chi_{\text{Red}}^2 = 2.4 \cdot 10^6$.

only gives slightly different values of J_1 and J_2 compared to the 6 spin model shown in figure 7.2. The two model almost fit the data equally well, both qualitatively and according to χ_{Red}^2 -values of the fit to the data at $T > 3$ K. The 6 spin model and 12 spin model have $\chi_{\text{Red}}^2 = 2.7 \cdot 10^6$ and $\chi_{\text{Red}}^2 = 2.4 \cdot 10^6$ respectively.

The next sections will introduce an approximative way of calculating the low temperature susceptibility of the full boelite system, to see how much it affects the result.

7.3 The variational model

In the previous section, it can be seen that the triangle model, the 6 spin model, and the 12 spin model describe the high temperature susceptibility equally well. This can be used to divide the model of the boelite system into a high and a low temperature model, where the triangle model describes the high temperature part of the susceptibility. A model of the low temperature region of the full 24 spin $S = 1/2$ system is introduced in the following sections.

7.3.1 Variational method

The low temperature model uses the *variational method*, which is based on the *variational principle*. The variational principle states that any state $|B\rangle$ of dimension N , will have [11]

$$\langle B | \hat{\mathcal{H}} | B \rangle = E \geq E_g, \quad (7.3)$$

where $\hat{\mathcal{H}}$, dimension $N \times N$, is the Hamiltonian that describes the system. E_g is the ground state of $\hat{\mathcal{H}}$. By picking a random test state $|B\rangle$, an upper bound of the ground state energy can be

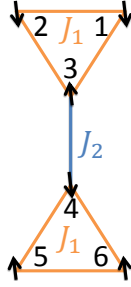


Figure 7.4: The 6 spin system. The numbers show the labeling of the spin sites. The coupling strengths between sites (J_1 and J_2) are shown with colored lines.

determined. The upper bound can be tightened by varying this random state.

The variational method introduces a way to choose the test state in a smart way. In the variational method, the test state $|B\rangle$ is written as a linear combination of random, orthogonal states $|b_j\rangle$, so that

$$|B\rangle = \sum_j c_j |b_j\rangle, \quad (7.4)$$

where c_j is a coefficient. c_j is determined by exact diagonalization of the matrix $\hat{\mathcal{H}}_s$, with matrix elements $\langle b_j | \hat{\mathcal{H}} | b_i \rangle$ [51]. The variational method has the additional benefit that not only is the lowest eigenvalue of $\hat{\mathcal{H}}_s$ an upper bound of E_g , but the larger eigenvalues of $\hat{\mathcal{H}}_s$ are upper bounds of the excited states of $\hat{\mathcal{H}}$ as well. To optimize the method, and tighten the estimated upper bounds, physical insight in the system can be used.

In the boelite system, the physical insight is that the system can be separated into a low and a high temperature system. A single Heisenberg spin triangle has 4 excited states with $E = \frac{3J_1}{4}$, and a 4 times degenerate ground state with $E = -\frac{3J_1}{4}$. At low temperatures, the gap between these two energy levels becomes much larger than the available thermal energy $k_B T \ll J_1$, which makes it improbable to excite the triangles.

It is likely that the ground state and the low energy excited states of the full boelite system are a linear combination $|T\rangle$ of isolated triangle ground states $|t_j\rangle$, since $J_1 \gg J_2$. I will therefore construct a model which estimates the low energy states of a coupled triangle system, by making linear combination of the isolated triangle ground states.

I will call this new model the *variational model*, since it is based on the variational method. I will in the following sections introduce the variational model, and show that it can model the low temperature susceptibility.

7.3.2 Notation and basic concept

The eigenstates and eigenenergies of a single triangle were calculated in chapter 3, and the results were shown in table 3.1. To introduce the variational model, I will use it to find the low energy eigenvalues of a 6 spin system, illustrated in figure 7.4. In order to show how the variational model works, the spins need to be labeled. In the following, I define spin number 1 to 3 to be in one triangle and spin number 4 to 6 to be in another. The two triangles are coupled through spin 3

and 4. To simplify the calculations, the two individual triangles $|m| = 1/2$ will be relabeled, as given in table 7.1. The $|m| = 3/2$ states are not relabeled as they will always be removed.

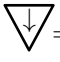
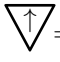










Triangle 1-3			
$m = -1/2$ subspace		$m = 1/2$ subspace	
State	Energy	State	Energy
 $= \frac{1}{\sqrt{3}}(1, \downarrow\rangle + 2, \downarrow\rangle + 3, \downarrow\rangle)$	$+\frac{3}{4}J_1$	 $= \frac{1}{\sqrt{3}}(1, \uparrow\rangle + 2, \uparrow\rangle + 3, \uparrow\rangle)$	$+\frac{3}{4}J_1$
 $= \frac{1}{\sqrt{3}}(1, \downarrow\rangle + e^+ 2, \downarrow\rangle + e^- 3, \downarrow\rangle)$	$-\frac{3}{4}J_1$	 $= \frac{1}{\sqrt{3}}(1, \uparrow\rangle + e^+ 2, \uparrow\rangle + e^- 3, \uparrow\rangle)$	$-\frac{3}{4}J_1$
 $= \frac{1}{\sqrt{3}}(1, \downarrow\rangle + e^- 2, \downarrow\rangle + e^+ 3, \downarrow\rangle)$	$-\frac{3}{4}J_1$	 $= \frac{1}{\sqrt{3}}(1, \uparrow\rangle + e^- 2, \uparrow\rangle + e^+ 3, \uparrow\rangle)$	$-\frac{3}{4}J_1$
Triangle 4-6			
$m = -1/2$ subspace		$m = 1/2$ subspace	
State	Energy	State	Energy
 $= \frac{1}{\sqrt{3}}(4, \downarrow\rangle + 5, \downarrow\rangle + 6, \downarrow\rangle)$	$+\frac{3}{4}J_1$	 $= \frac{1}{\sqrt{3}}(4, \uparrow\rangle + 5, \uparrow\rangle + 6, \uparrow\rangle)$	$+\frac{3}{4}J_1$
 $= \frac{1}{\sqrt{3}}(4, \downarrow\rangle + e^+ 5, \downarrow\rangle + e^- 6, \downarrow\rangle)$	$-\frac{3}{4}J_1$	 $= \frac{1}{\sqrt{3}}(4, \uparrow\rangle + e^+ 5, \uparrow\rangle + e^- 6, \uparrow\rangle)$	$-\frac{3}{4}J_1$
 $= \frac{1}{\sqrt{3}}(4, \downarrow\rangle + e^- 5, \downarrow\rangle + e^+ 6, \downarrow\rangle)$	$-\frac{3}{4}J_1$	 $= \frac{1}{\sqrt{3}}(4, \uparrow\rangle + e^- 5, \uparrow\rangle + e^+ 6, \uparrow\rangle)$	$-\frac{3}{4}J_1$

Table 7.1: $|m| = 1/2$ triangle eigenstates of the upper triangle (point-down triangle with spin 1 to 3) and lower triangle (point-down triangle with spin 4 to 6) of the 6 spin system in figure 7.4, with the new type of labeling. The constants $e^+ = e^{+i\frac{2\pi}{3}}$ and $e^- = e^{-i\frac{2\pi}{3}}$. The Ising states, eg. $|1, \downarrow\rangle$ etc. are given in equation (3.1)

When calculating the matrix elements of the Hamiltonian, the variational model uses that the zero point of the energy is equal to the sum of the ground state energies from two individual triangles. The model effectively sets $J_1 \rightarrow \infty$, which makes it impossible to excite the triangles.

The Heisenberg Hamiltonian's interaction term from equation (2.19) can for this low temperature, two triangle system be rewritten into

$$\hat{\mathcal{H}}_6 = J_2 \hat{\mathbf{S}}_3 \cdot \hat{\mathbf{S}}_4 = J_2 \hat{S}_3^z \hat{S}_4^z + \frac{J_2}{2} (\hat{S}_3^- \hat{S}_4^+ + \hat{S}_4^- \hat{S}_3^+). \quad (7.5)$$

The new Hamiltonian only has 16 eigenstates (4 ground states on each triangle giving a total of $4^2 = 16$ configurations). The diagonalizing of the Hamiltonian is done in a basis consisting of all possible configuration of outer products between the isolated triangle ground states. The basis has

the following orthogonal and normalized basis states

$$\begin{aligned}
 & \left\{ \begin{array}{l} \nabla \otimes \triangle, \quad \nabla \otimes \triangle, \quad \nabla \otimes \triangle, \quad \nabla \otimes \triangle \\ \nabla \otimes \triangle, \quad \nabla \otimes \triangle, \quad \nabla \otimes \triangle, \quad \nabla \otimes \triangle \\ \nabla \otimes \triangle, \quad \nabla \otimes \triangle, \quad \nabla \otimes \triangle, \quad \nabla \otimes \triangle \\ \nabla \otimes \triangle, \quad \nabla \otimes \triangle, \quad \nabla \otimes \triangle, \quad \nabla \otimes \triangle \end{array} \right\} \quad m = -1, \\
 & \left\{ \begin{array}{l} \nabla \otimes \triangle, \quad \nabla \otimes \triangle, \quad \nabla \otimes \triangle, \quad \nabla \otimes \triangle \\ \nabla \otimes \triangle, \quad \nabla \otimes \triangle, \quad \nabla \otimes \triangle, \quad \nabla \otimes \triangle \\ \nabla \otimes \triangle, \quad \nabla \otimes \triangle, \quad \nabla \otimes \triangle, \quad \nabla \otimes \triangle \\ \nabla \otimes \triangle, \quad \nabla \otimes \triangle, \quad \nabla \otimes \triangle, \quad \nabla \otimes \triangle \end{array} \right\} \quad m = +1, \\
 & \left\{ \begin{array}{l} \nabla \otimes \triangle, \quad \nabla \otimes \triangle, \quad \nabla \otimes \triangle, \quad \nabla \otimes \triangle \\ \nabla \otimes \triangle, \quad \nabla \otimes \triangle, \quad \nabla \otimes \triangle, \quad \nabla \otimes \triangle \\ \nabla \otimes \triangle, \quad \nabla \otimes \triangle, \quad \nabla \otimes \triangle, \quad \nabla \otimes \triangle \\ \nabla \otimes \triangle, \quad \nabla \otimes \triangle, \quad \nabla \otimes \triangle, \quad \nabla \otimes \triangle \end{array} \right\} \quad m = 0.
 \end{aligned} \tag{7.6}$$

For the full boleite system, this new variational model will reduce the number of states by a factor of $2^8 = 256$ (i.e. from 2^{24} to $4^8 = 2^{16}$). Together with block diagonalization, this will reduce the problem so that the largest matrix that needs to be diagonalized for the 24 spin system will be $\sim 2^{12} \times 2^{12}$. This can be done on a desktop computer.

7.3.3 Calculation the spin 6 system

The 6 spin system has in the reduced low temperature form only three m-subspaces, $m = [-1, 0, +1]$. I will use the $m = +1$ subspace as an introduction on how the full 6 spin system is calculated. The Hamiltonian $\hat{\mathcal{H}}_6$ first needs to be written into its matrix form. The matrix elements are given by $\langle i | \hat{\mathcal{H}}_6 | j \rangle$, where i and j are the basis states presented in equation (7.6). All matrix elements are found by applying the Hamiltonian to each of the 4 states to see which states they map into. As an example (The Ising notation, like $|1, \uparrow\rangle$ or $|6, \uparrow\rangle$, is taken from equation (3.1)):

$$\begin{aligned}
 \hat{\mathcal{H}}_6 \left(\nabla \otimes \triangle \right) &= \frac{J_2}{3} \hat{\mathbf{S}}_3 \cdot \hat{\mathbf{S}}_4 \left(|1, \uparrow\rangle + e^+ |2, \uparrow\rangle + e^- |3, \uparrow\rangle \right) \otimes \left(|4, \uparrow\rangle + e^+ |5, \uparrow\rangle + e^- |6, \uparrow\rangle \right) \\
 &= \frac{J_2}{3} \hat{\mathbf{S}}_3 \cdot \hat{\mathbf{S}}_4 \left(|1, \uparrow\rangle |4, \uparrow\rangle + e^+ |1, \uparrow\rangle |5, \uparrow\rangle + e^- |1, \uparrow\rangle |6, \uparrow\rangle \right. \\
 &\quad \left. + e^+ |2, \uparrow\rangle |4, \uparrow\rangle + e^- |2, \uparrow\rangle |5, \uparrow\rangle + |2, \uparrow\rangle |6, \uparrow\rangle \right. \\
 &\quad \left. + e^- |3, \uparrow\rangle |4, \uparrow\rangle + |3, \uparrow\rangle |5, \uparrow\rangle + e^+ |3, \uparrow\rangle |6, \uparrow\rangle \right) \\
 &= \frac{J_2}{12} \left(- |1, \uparrow\rangle |4, \uparrow\rangle + e^+ |1, \uparrow\rangle |5, \uparrow\rangle + e^- |1, \uparrow\rangle |6, \uparrow\rangle \right. \\
 &\quad \left. - e^+ |2, \uparrow\rangle |4, \uparrow\rangle + e^- |2, \uparrow\rangle |5, \uparrow\rangle + |2, \uparrow\rangle |6, \uparrow\rangle \right. \\
 &\quad \left. + e^- |3, \uparrow\rangle |4, \uparrow\rangle - |3, \uparrow\rangle |5, \uparrow\rangle - e^- |3, \uparrow\rangle |6, \uparrow\rangle \right) \\
 &= \frac{J_2}{12} \left(|1, \uparrow\rangle + e^+ |2, \uparrow\rangle - e^- |3, \uparrow\rangle \right) \otimes \left(-|4, \uparrow\rangle + e^+ |5, \uparrow\rangle + e^- |6, \uparrow\rangle \right) \\
 &= \frac{J_2}{36} \left(\nabla - 2e^+ \nabla - 2e^- \nabla \right) \otimes \left(\triangle - 2\triangle - 2\triangle \right). \tag{7.7}
 \end{aligned}$$

The raising and lowering operators do not affect the $m = 1$ states since they only give a non-zero result when the combined single triangle states (like $|2, \uparrow\rangle |4, \uparrow\rangle$), contain either $|3, \uparrow\rangle$ or $|4, \uparrow\rangle$. As an example $\hat{S}_3^- \hat{S}_4^+ |2, \uparrow\rangle |4, \uparrow\rangle = |1, \downarrow\rangle |\uparrow\uparrow\rangle_{4-6}$, whereas $\hat{S}_3^- \hat{S}_4^+ |2, \uparrow\rangle |5, \uparrow\rangle = 0$. When the raising and lowering operators give a non zero result for the $m = 1$ basis states, they will always lead to

combined single triangle states containing $|\uparrow\uparrow\uparrow\rangle$. This state is an excited isolated triangle state, and is not possible to reach since $J_1 \rightarrow \infty$. The $\hat{S}_3^z \hat{S}_4^z$ also couples the state to excited triangle states (i.e. \triangleup and $\nabla\uparrow$), which are also removed due to $J_1 \rightarrow \infty$. The final result is:

$$\begin{aligned}\hat{\mathcal{H}}_6 \left(\nabla\uparrow \otimes \triangleup \right) &= \frac{J_2}{36} \left(\nabla\uparrow - 2e^+ \nabla\uparrow \right) \otimes \left(\triangleup - 2\triangleup \right) \\ &= \frac{J_2}{36} \left(\nabla\uparrow \otimes \triangleup - 2\nabla\uparrow \otimes \triangleup - 2e^+ \nabla\uparrow \otimes \triangleup + 4e^+ \nabla\uparrow \otimes \triangleup \right).\end{aligned}\quad (7.8)$$

When these calculations are done for the three other $m = +1$ states, the results are:

$$\hat{\mathcal{H}}_6 \left(\nabla\uparrow \otimes \triangleup \right) = \frac{J_2}{36} \left(\nabla\uparrow \otimes \triangleup - 2\nabla\uparrow \otimes \triangleup - 2e^+ \nabla\uparrow \otimes \triangleup + 4e^+ \nabla\uparrow \otimes \triangleup \right), \quad (7.9)$$

$$\hat{\mathcal{H}}_6 \left(\nabla\uparrow \otimes \triangleup \right) = \frac{J_2}{36} \left(\nabla\uparrow \otimes \triangleup - 2\nabla\uparrow \otimes \triangleup - 2e^- \nabla\uparrow \otimes \triangleup + 4e^- \nabla\uparrow \otimes \triangleup \right), \quad (7.10)$$

$$\hat{\mathcal{H}}_6 \left(\nabla\uparrow \otimes \triangleup \right) = \frac{J_2}{36} \left(\nabla\uparrow \otimes \triangleup - 2\nabla\uparrow \otimes \triangleup - 2e^- \nabla\uparrow \otimes \triangleup + 4e^- \nabla\uparrow \otimes \triangleup \right). \quad (7.11)$$

Using equations (7.8) to (7.11), I can write the Hamiltonian in matrix form:

$$\hat{\mathcal{H}}_{6,m=+1} = \begin{pmatrix} \nabla\uparrow \otimes \triangleup \\ \nabla\uparrow \otimes \triangleup \\ \nabla\uparrow \otimes \triangleup \\ \nabla\uparrow \otimes \triangleup \end{pmatrix}^\dagger \begin{pmatrix} \nabla\uparrow \otimes \triangleup & \nabla\uparrow \otimes \triangleup & \nabla\uparrow \otimes \triangleup & \nabla\uparrow \otimes \triangleup \\ \nabla\uparrow \otimes \triangleup & \nabla\uparrow \otimes \triangleup & \nabla\uparrow \otimes \triangleup & \nabla\uparrow \otimes \triangleup \\ \nabla\uparrow \otimes \triangleup & \nabla\uparrow \otimes \triangleup & \nabla\uparrow \otimes \triangleup & \nabla\uparrow \otimes \triangleup \\ \nabla\uparrow \otimes \triangleup & \nabla\uparrow \otimes \triangleup & \nabla\uparrow \otimes \triangleup & \nabla\uparrow \otimes \triangleup \end{pmatrix} \begin{pmatrix} 1 & -2 & -2e^- & 4e^- \\ -2 & 1 & 4e^- & -2e^- \\ -2e^+ & 4e^+ & 1 & -2 \\ 4e^+ & -2e^+ & -2 & 1 \end{pmatrix} \cdot \frac{J_2}{36} \quad (7.12)$$

Diagonalizing $\hat{\mathcal{H}}_{6,m=+1}$ gives the following eigenvalues:

$$E_{m=+1,1} = -\frac{J_2}{12} \quad E_{m=+1,2} = -\frac{J_2}{12} \quad E_{m=+1,3} = \frac{J_2}{36} \quad E_{m=+1,4} = \frac{J_2}{4} \quad (7.13)$$

The exact same is found for $\hat{\mathcal{H}}_{6,m=-1}$, as could be expected from the time reversal symmetry of the Heisenberg Hamiltonian.

For $m = 0$, it becomes significantly more complicated, since all 8 states couple to all 8 states. An example of what happens when the Hamiltonian $\hat{\mathcal{H}}_6$ is applied to a basis state can be seen in

appendix B. Below, the full Hamiltonian of the $m = 0$ subspace is shown:

$$\hat{\mathcal{H}}_{6,m=0} = \begin{pmatrix} \nabla \otimes \triangle \\ \nabla \otimes \triangle \\ \nabla \otimes \triangle \\ \nabla \otimes \triangle \\ \nabla \otimes \triangle \\ \nabla \otimes \triangle \\ \nabla \otimes \triangle \\ \nabla \otimes \triangle \end{pmatrix}^\dagger \begin{pmatrix} \nabla \otimes \triangle & \nabla \otimes \triangle & \nabla \otimes \triangle & \nabla \otimes \triangle & \nabla \otimes \triangle & \nabla \otimes \triangle & \nabla \otimes \triangle & \nabla \otimes \triangle \\ \nabla \otimes \triangle & \nabla \otimes \triangle & \nabla \otimes \triangle & \nabla \otimes \triangle & \nabla \otimes \triangle & \nabla \otimes \triangle & \nabla \otimes \triangle & \nabla \otimes \triangle \\ \nabla \otimes \triangle & \nabla \otimes \triangle & \nabla \otimes \triangle & \nabla \otimes \triangle & \nabla \otimes \triangle & \nabla \otimes \triangle & \nabla \otimes \triangle & \nabla \otimes \triangle \\ \nabla \otimes \triangle & \nabla \otimes \triangle & \nabla \otimes \triangle & \nabla \otimes \triangle & \nabla \otimes \triangle & \nabla \otimes \triangle & \nabla \otimes \triangle & \nabla \otimes \triangle \\ \nabla \otimes \triangle & \nabla \otimes \triangle & \nabla \otimes \triangle & \nabla \otimes \triangle & \nabla \otimes \triangle & \nabla \otimes \triangle & \nabla \otimes \triangle & \nabla \otimes \triangle \\ \nabla \otimes \triangle & \nabla \otimes \triangle & \nabla \otimes \triangle & \nabla \otimes \triangle & \nabla \otimes \triangle & \nabla \otimes \triangle & \nabla \otimes \triangle & \nabla \otimes \triangle \\ \nabla \otimes \triangle & \nabla \otimes \triangle & \nabla \otimes \triangle & \nabla \otimes \triangle & \nabla \otimes \triangle & \nabla \otimes \triangle & \nabla \otimes \triangle & \nabla \otimes \triangle \\ \nabla \otimes \triangle & \nabla \otimes \triangle & \nabla \otimes \triangle & \nabla \otimes \triangle & \nabla \otimes \triangle & \nabla \otimes \triangle & \nabla \otimes \triangle & \nabla \otimes \triangle \end{pmatrix} \begin{pmatrix} -1 & 2 & -4e^- & 2e^- & 2 & -4 & 8e^- & -4e^- \\ 2 & -1 & 2e^- & -4e^- & -4 & 2 & -4e^- & 8e^- \\ -4e^+ & 2e^+ & -1 & 2 & 8e^+ & -4e^+ & 2 & -4 \\ 2e^+ & -4e^+ & 2 & -1 & -4e^+ & 8e^+ & -4 & 2 \\ 2 & -4 & 8e^- & -4e^- & -1 & 2 & -4e^- & 2e^- \\ -4 & 2 & -4e^- & 8e^- & 2 & -1 & 2e^- & -4e^- \\ 8e^+ & -4e^+ & 2 & -4 & -4e^+ & 2e^+ & -1 & 2 \\ -4e^+ & 8e^+ & -4 & 2 & 2e^+ & -4e^+ & 2 & -1 \end{pmatrix} \cdot \frac{J_2}{36} \quad (7.14)$$

The eigenvalues to $H_{m=0}$ are the following:

$$\begin{aligned} E_{m=0,1} &= -\frac{3J_2}{4} & E_{m=0,2} &= -\frac{J_2}{12} & E_{m=0,3} &= -\frac{J_2}{12} & E_{m=0,4} &= -\frac{J_2}{12} \\ E_{m=0,5} &= \frac{J_2}{36} & E_{m=0,6} &= \frac{J_2}{4} & E_{m=0,7} &= \frac{J_2}{4} & E_{m=0,8} &= \frac{J_2}{4} \end{aligned} \quad (7.15)$$

It should be mentioned here that relabeling the triangle spin sites, so that for instance 1 and 5 are the spins that couples with J_2 , gives the same eigenvalues.

7.3.4 Comparison to complete diagonalization

Now let us compare the result found in the above section to the result found when diagonalizing the full Hamiltonian. The full 6 spin system has been diagonalized by hand in reference [6]. In table 7.2, the low lying eigenvalues from the complete diagonalization is compared to the results obtained by the variational model. The table shows that the two results are identical when the approximation $J_1 \gg J_2$ is applied.

7.4 The variational model and 24 spin boleite system

To calculate all low lying eigenenergies of the full boleite system, the variational model needs to be implemented in a computer algorithm.

In the computer algorithm, it is no longer useful to keep the triangle notation, from table 7.1, as we do not no longer need to only distinguish between the ground states of two coupled triangles.

	Complete diagonalization	Complete diagonalization for $E_G(J_2 = 0) = 0$ and $J_1 \rightarrow \infty$	Variational model
$E_{ m =1}$	$\approx \begin{cases} -\frac{3}{2}J_1 + \frac{1}{4}J_2 & 2 \text{ states} \\ -\frac{3}{2}J_1 + \frac{1}{36}J_2 & 2 \text{ states}^* \\ -\frac{3}{2}J_1 - \frac{1}{12}J_2 & 4 \text{ states}^* \end{cases}$	$\begin{cases} \frac{1}{4}J_2 & 2 \text{ states} \\ \frac{1}{36}J_2 & 2 \text{ states}^* \\ -\frac{1}{12}J_2 & 4 \text{ states}^* \end{cases}$	$\begin{cases} \frac{1}{4}J_2 & 2 \text{ states} \\ \frac{1}{36}J_2 & 2 \text{ states} \\ -\frac{1}{12}J_2 & 4 \text{ states} \end{cases}$
$E_{ m =0}$	$\approx \begin{cases} -\frac{3}{2}J_1 + \frac{1}{4}J_2 & 3 \text{ states} \\ -\frac{3}{2}J_1 + \frac{1}{36}J_2 & 1 \text{ states}^* \\ -\frac{3}{2}J_1 - \frac{1}{12}J_2 & 3 \text{ states}^* \\ -\frac{3}{2}J_1 - \frac{3}{4}J_2 & 1 \text{ state} \end{cases}$	$\begin{cases} \frac{1}{4}J_2 & 3 \text{ states} \\ \frac{1}{36}J_2 & 1 \text{ states}^* \\ -\frac{1}{12}J_2 & 3 \text{ states}^* \\ -\frac{3}{4}J_2 & 1 \text{ state} \end{cases}$	$\begin{cases} \frac{1}{4}J_2 & 3 \text{ states} \\ \frac{1}{36}J_2 & 1 \text{ state} \\ -\frac{1}{12}J_2 & 3 \text{ states} \\ -\frac{3}{4}J_2 & 1 \text{ state} \end{cases}$

Table 7.2: Comparison between the variational model used on a 6 spin system, and the complete diagonalization of a 6 spin system. **Left:** The complete diagonalization results for the 6 spin system. Only states of energy $\sim -\frac{3}{2}J_1$ are shown. Exact diagonalization results are taken from [6], and the full results can be seen in appendix A. **Center:** The complete diagonalization results for the 6 spin system, where the ground state of two non coupled triangles is set as the zero point energy, $E_G(J_2 = 0) = 0$, and $J_1 \rightarrow \infty$. **Right:** Full result of variational model. * marks that this energy is only valid when $J_2^2 \ll J_1^2$.

Instead, we need to distinguish between the 4 ground states of 8 different triangles. To do so, each triangle ground state will have a number and be relabeled with

$$\begin{aligned}
|0\rangle &= |-1/2, 1\rangle &= \frac{1}{\sqrt{3}}(|s_{(1,t),\downarrow}\rangle + e^+|s_{(2,t),\downarrow}\rangle + e^-|s_{(3,t),\downarrow}\rangle), \\
|1\rangle &= |-1/2, -1\rangle &= \frac{1}{\sqrt{3}}(|s_{(1,t),\downarrow}\rangle + e^-|s_{(2,t),\downarrow}\rangle + e^+|s_{(3,t),\downarrow}\rangle), \\
|2\rangle &= |1/2, 1\rangle &= \frac{1}{\sqrt{3}}(|s_{(1,t),\uparrow}\rangle + e^+|s_{(2,t),\uparrow}\rangle + e^-|s_{(3,t),\uparrow}\rangle), \\
|3\rangle &= |1/2, -1\rangle &= \frac{1}{\sqrt{3}}(|s_{(1,t),\uparrow}\rangle + e^-|s_{(2,t),\uparrow}\rangle + e^+|s_{(3,t),\uparrow}\rangle). \quad (7.16)
\end{aligned}$$

The labeling $|m, r\rangle$ shows the magnetization m and the rotation direction r of a single triangle's state. Rotation refers to the order of the phase factor (1 , e^+ , and e^-) in equation (7.16). $s_{i,t}$ is the number (integer from 1 to 24 for the full boelite system) of the i 'th spin in the t 'th triangle. The Ising states, like $|s_{(1,t),\downarrow}\rangle$ and $|s_{(2,t),\uparrow}\rangle$, are equivalent with the definition in (3.1). The triangle ground states depend on the numbering of the individual spins, but the final eigenenergies is independent of the numbering of the spins.

The full system's variational model's basis states will be a combination of the numbers 0 to 3, revealing the state of each triangle. As an example, we have for the $m = 0$ state: $|1/2, 1\rangle \otimes |-1/2, -1\rangle = |12\rangle$.

An example of a 4 triangle system could be the $m = 1$ state $|1021\rangle$. Here triangle 1 is in a $|1\rangle = |-1/2, -1\rangle$ state, triangle 2 is in a $|2\rangle = |1/2, 1\rangle$ state, triangle 3 is in a $|0\rangle = |-1/2, 1\rangle$

state, and triangle 4 is in a $|1\rangle = |-1/2, -1\rangle$ state.

By using this triangle ground state numbering, all the 4^N unique basis states from a system with N triangles, can be written as $|000.....0\rangle$ to $|333.....3\rangle$.

The Heisenberg Hamiltonian from equation (2.18) is reduced to the spin interaction terms between inter triangle neighbors (int) as

$$\hat{\mathcal{H}}_N = J_2 \sum_{\langle i,j \rangle}^{\text{int}} \hat{\mathbf{S}}_i \cdot \hat{\mathbf{S}}_j. \quad (7.17)$$

When the spin operators (\hat{S}_j^z , \hat{S}_j^+ , and \hat{S}_j^-) are applied to a variational model basis state, it will apply to each individual triangle Ising state like $|s_{i,t}, \uparrow\rangle$ and $|s_{i,t}, \downarrow\rangle$ which contains spin $s_{i,t} = j$. In the variational model basis states, each triangle Ising state has a phase factor, i.e. 1, e^+ , and e^- , as seen in equation (7.16). I will use $P_{s_{i,t}}$ to denote the phase factors in front of the Ising states, like $|s_{i,t}, \uparrow\rangle$ and $|s_{i,t}, \downarrow\rangle$, in any given triangle t 's ground state $|m, r\rangle$.

When the operator \hat{S}_j^z is applied to a triangle ground state, it is the phase factor of triangle Ising state with $s_{(i,t)} = j$ that becomes important since

$$\hat{S}_j^z |m, r\rangle = 2m |m, r\rangle - 4m P_j^* |m, -r\rangle, \quad (7.18)$$

where P_j^* is the complex conjugate of the phase factor in front of the Ising state $j = s_{i,t}$ ($|j, \uparrow\rangle$ or $|j, \downarrow\rangle$) in triangle state $|m, r\rangle$.

For the raising and lowering operators, it is again the phase factor of the $s_{i,t} = j$ Ising state that becomes important when applying the spin operator to the j 'th spin.

For \hat{S}_j^+ , the magnetization of the state is changed as well as the spin rotation

$$\hat{S}_j^+ |m, r\rangle = -|-m, r\rangle + 2P_j^* |-m, -r\rangle \quad \text{For } m = -1/2 \quad (7.19)$$

$$\hat{S}_j^+ |m, r\rangle = 0 \quad \text{For } m = +1/2. \quad (7.20)$$

The opposite is true for the \hat{S}_j^-

$$\hat{S}_j^- |m, r\rangle = -|-m, r\rangle + 2P_j^* |-m, -r\rangle \quad \text{For } m = +1/2 \quad (7.21)$$

$$\hat{S}_j^- |m, r\rangle = 0 \quad \text{For } m = -1/2. \quad (7.22)$$

The above shows that two coupled triangles need to be of opposite magnetization for the lowering-raising operator term to give a non zero result.

The computer algorithm needs the above math to calculate all matrix elements in $\langle i | \hat{\mathcal{H}}_N | j \rangle$. The algorithm uses the orthogonality of the basis states to do this. When $\hat{\mathcal{H}}_N$ is applied to a specific coupling, the basis state $|i\rangle$ will be mapped into N_B other basis states labeled $|B_n\rangle$. $N_B = 4$ triangle states in the coupling have the same magnetization, and $N_B = 8$ if they have opposite magnetization. This was also seen in the calculations of the two coupled triangles above. The algorithm locates the N_B matrix elements $\langle B_n | \hat{\mathcal{H}}_N | i \rangle$ and adds the pre-factor in front of $|B_n\rangle$ to the elements. The pre-factor is found together with the N_B states from computing $\hat{\mathcal{H}}_N | i \rangle$.

The $m = +1$ basis state $|1021\rangle$ from a 4 triangle system can be used as an example of how the algorithm finds the matrix elements.

There will be a coupling between triangle 1 and 2, and I define that it is the spin number 3 from triangle 1 that couples to spin number 4 from triangle 2 (the result is of course independent of

numbering). Spin triangle one is in state $|1\rangle = |-1/2, -1\rangle = \frac{1}{\sqrt{3}}(|1, \downarrow\rangle + e^-|2, \downarrow\rangle + e^+|3, \downarrow\rangle)$, and spin triangle two is in state $|2\rangle = |1/2, 1\rangle = \frac{1}{\sqrt{3}}(|4, \uparrow\rangle + e^+|5, \uparrow\rangle + e^-|6, \uparrow\rangle)$. It is only triangle 1 and 2 that are affected by $\hat{\mathbf{S}}_3 \cdot \hat{\mathbf{S}}_4$, since spin 3 and 4 reside in triangle 1 and 2. When applying the operators to the exchange coupling the following happens

$$\begin{aligned} & J_2 \left(\hat{S}_3^z \hat{S}_4^z |1021\rangle + \frac{\hat{S}_3^+ \hat{S}_4^- + \hat{S}_4^+ \hat{S}_3^-}{2} |1021\rangle \right) \\ &= \frac{J_2}{36} (-|1021\rangle + 2|1031\rangle + 2e^-|1020\rangle - 4e^-|1030\rangle + 2|1003\rangle - 4|1013\rangle + 8e^-|1012\rangle - 4e^-|1002\rangle) \end{aligned} \quad (7.23)$$

In this way the 8 matrix elements in $\hat{\mathcal{H}}_N$ have the following pre-terms added:

$$\begin{array}{llll} \frac{J_2}{36} & \text{is added to:} & \langle 1021 | \hat{\mathcal{H}}_N | 1021 \rangle, & \frac{J_2}{16} & \text{is added to:} & \langle 1003 | \hat{\mathcal{H}}_N | 1021 \rangle, \\ \frac{J_2}{16} & \text{is added to:} & \langle 1031 | \hat{\mathcal{H}}_N | 1021 \rangle, & -\frac{J_2}{8} & \text{is added to:} & \langle 1013 | \hat{\mathcal{H}}_N | 1021 \rangle, \\ \frac{J_2 e^-}{16} & \text{is added to:} & \langle 1020 | \hat{\mathcal{H}}_N | 1021 \rangle, & \frac{J_2 e^-}{4} & \text{is added to:} & \langle 1012 | \hat{\mathcal{H}}_N | 1021 \rangle, \\ -\frac{J_2 e^-}{8} & \text{is added to:} & \langle 1030 | \hat{\mathcal{H}}_N | 1021 \rangle, & -\frac{J_2 e^-}{8} & \text{is added to:} & \langle 1002 | \hat{\mathcal{H}}_N | 1021 \rangle. \end{array} \quad (7.24)$$

The above procedure is repeated for every state and every coupling, and in that way all non zero elements $\langle i | \hat{\mathcal{H}}_N | j \rangle$ in the matrix are found and calculated. In the end all eigenenergies of $\hat{\mathcal{H}}_N$, from equation (7.17), are found by complete diagonalization.

7.4.1 The result

To estimate the accuracy of the variational model, it is compared to the exact diagonalization of the full 24 spin boelite system done with Lanczos algorithm, using RLexact. Lanczos algorithm only finds the lowest energy states, and only one state for each set of degenerate states, as explained in chapter 3.

RLexact and the new variational model's result of the 24 spin system, and the Mexact results of the 12 spin model (presented in figure 7.1c) are compared in figure 7.5. The figure shows that the lowest eigenenergies of the full 24 spin boelite system predicted by the variational model and RLexact resemble each other closely. The eigenenergies of the 12 spin model found by Mexact is on the other hand quite different from the two. It is seen from the figure that for small values of $J_2/J_1 = 0.026$, the lowest eigenvalues from the variational model and RLexact are almost the same with an average difference of only 1.19 ± 0.04 % of the RLexact values. This is of course keeping in mind that degenerate states are not found by RLexact. As J_2/J_1 is increased to 0.175, the variational model eigenenergies begin to have increasingly larger values than the RLexact eigenenergies. The average difference between the RLexact results and the variational model results for $J_2/J_1 = 0.175$ is 7.8 ± 0.2 % of the RLexact values. The variational model relies on the approximation $J_2/J_1 \ll 1$, and the above observation shows that when this approximation becomes less valid, the variational model gives an increasingly looser upper bound.

Other interesting things are also seen from figure 7.5. Most noticeable is that the system seems

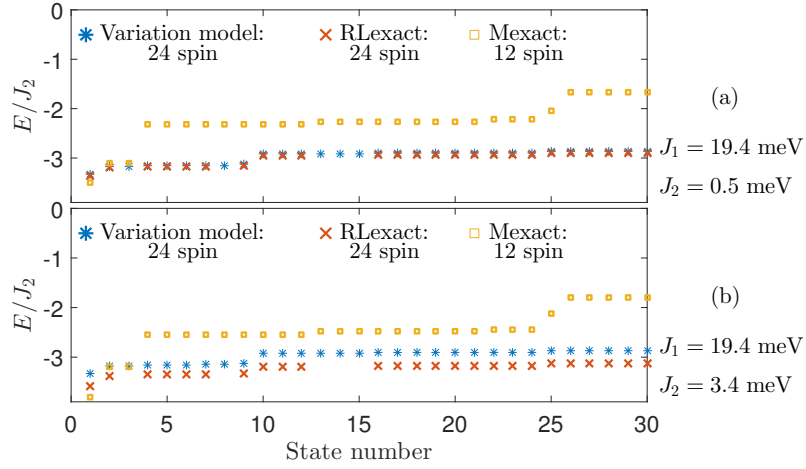


Figure 7.5: The ground state and the lowest excited states divided by J_2 predicted from the 12 spin model with Mexact, and the full 24 spin system with the variational model and RLexact. (a) and (b) show the results for two different values of J_2 and fixed J_1 (given to the right of the figure). RLexact results are obtained with Lanczos algorithm. Lanczos algorithm only finds one state in a degenerate set, and only one value from the RLexact result is plotted for every degenerate state found by the variational model. The $E/J_2 = 0$ corresponds to the ground state of non coupled triangles ($J_2 = 0$ meV). The eigenenergies from the 12 spin model is multiplied with 2, to account for the half number of spins in the 12 spin system.

to have a unique non-degenerate ground state, with a gap of $0.16 J_2$ to a group of 8 states with almost the same energy including some degenerate states. From the 10th state we reach a pseudo-continuum of excited states, where the lowest energy is $0.31 J_2$ larger than the ground state.

The susceptibility of a system can be calculated from the eigenenergies of the corresponding Hamiltonian as according to equation (4.8). The variational model only finds the low energy states, and so it can only give an estimate of the low temperature region of the susceptibility, where the thermal energy $k_B T$ is of a similar size or less than J_2 . The initial guess was that the triangle model could describe the high temperature region of a coupled triangle system when J_2/J_1 is small.

To test the variational model, it is used to predict the low temperature susceptibility of 4 coupled triangles. The result is compared to the susceptibility of a 12 spin model without periodic boundary condition and with a 4 isolated triangles model, both predicted from complete diagonalization with Mexact. The comparison is shown in figure 7.6. Three temperature regions are identified from the figure:

- $T > 80$ K: The 12 spin model and the 4 isolated triangles model give almost the same result. The variational model disagree as expected.
- $40 \text{ K} < T < 80 \text{ K}$ all three models agree.
- $T < 40 \text{ K}$ The variational model and the 12 model are very close. At temperatures below 2 K, the 12 spin model gives an infinite inverse susceptibility, whereas the variational model does not. The 4 isolated triangle model does as expected not fit the 12 spin system at these temperatures.

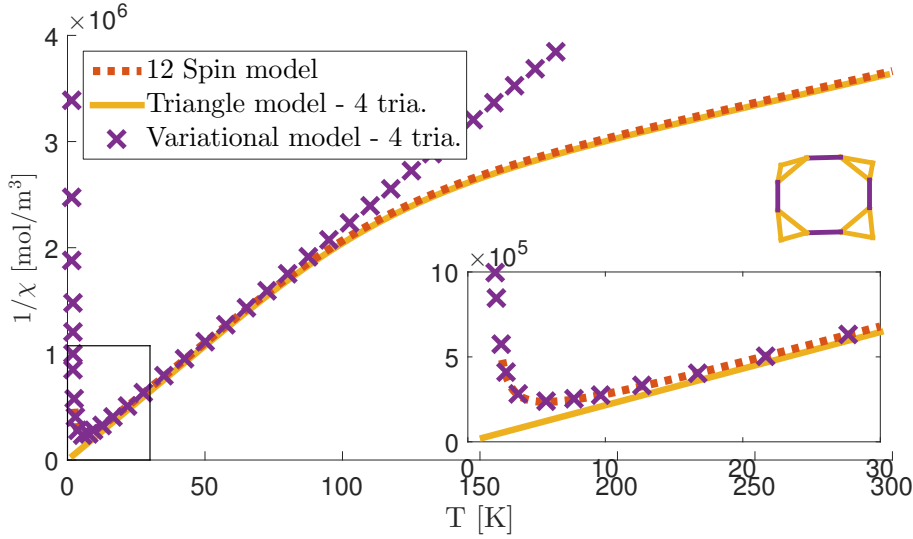


Figure 7.6: Different models of a 12 spin half boelite cube compared to each other. The half boelite cube is illustrated in the top right corner, with yellow triangles and purple inter triangle couplings. The three different models are: "12 spin model", which is based on the eigenvalues of the full 12 spin system found with Mexact. "Triangle model - 4 tria.", which is based on the eigenvalues of 4 isolated triangles found with Mexact. The "Variational model - 4 tria.", which is based on the variational model's prediction of the eigenvalues of 4 coupled triangles. The models have $J_1 = 24.6$ meV and $J_2 = 1.6$ meV. The inserted plot is a zoom-in on low temperatures.

Taking the above into account, a good estimate is that the full 24 spin boelite system can be described by a combined model:

- $T > 50$ K: The susceptibility is calculated from eigenenergies of the 8 isolated triangles model.
- $T \leq 50$ K: The susceptibility is calculated from eigenenergies of the variational model used on 8 coupled triangles.

This combined 24 spin model will in short be denoted the *CVT* (Combined Variation and Triangle) model.

A comparison between the boelite susceptibility data and the CVT model is seen in figure 7.7. As was the case for the 12 spin model, the CVT model gives a susceptibility that is quite different from the data. The 12 spin model, fitted to the inverse susceptibility data in figure 7.3, and the CVT model, shown in figure 7.7 give almost the same result both in terms of the qualitative appearance of the susceptibility curve and exchange constants. The 12 spin model predicts $J_1 = 24.6 \pm 0.2$ meV and $J_2 = 1.6 \pm 0.1$ meV, whereas the CVT model predicts $J_1 = 24.9 \pm 0.2$ meV and $J_2 = 1.3 \pm 0.1$ meV. Looking at the χ_{Red}^2 value of the two fits, the CVT model fits the data at $T > 3$ K slightly better, with a $\chi_{\text{Red}}^2 = 1.6 \cdot 10^6$ compared to the 12 spin model's $\chi_{\text{Red}}^2 = 2.4 \cdot 10^6$. From the χ_{Red}^2 -values and the predictions of the low eigenenergies seen in figure 7.5, the 24 spin CVT model seems to be the best model, of the ones presented, to account for the boelite system.

In the next section, I will show how a paramagnetic contribution can give rise to the difference between the data and the models.

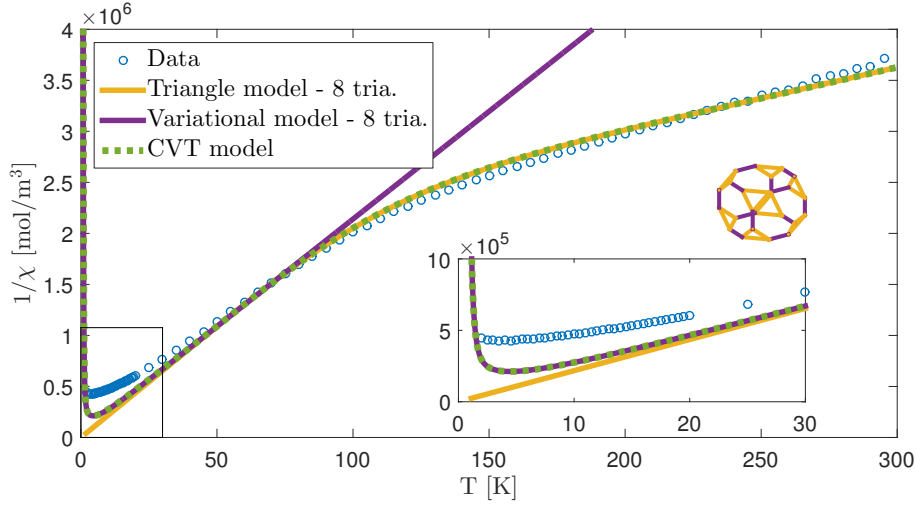


Figure 7.7: The measured inverse susceptibility from the boleite type 2 crystal K (data) fitted with the CVT model used on the full 24 spin Boleite cube. The full boleite cube is shown in the top right corner, with yellow triangles and purple inter triangle couplings. The CVT model consists of a model of 8 isolated triangles (Triangle model - 8 tria.), which is controlled by J_1 , and the variational model used on 8 coupled triangles (Variational model - 8 tria.), which is controlled by J_2 . The models are fitted together by keeping the scaling parameter $1/\chi_0 = (4.86 \pm 0.02) \cdot 10^5$ mol/m³ the same. The best fit is found at $J_1 = 24.9 \pm 0.2$ meV and $J_2 = 1.3 \pm 0.1$ meV. After fitting, the two models are forced to overlap at $T = 50$ K by adjusting the triangle model's scaling parameter. The scaling parameter is adjusted less than $\sim 3\%$. The insert plot is a zoom in on low temperatures. The best CVT fit to the data at $T > 3$ K has $\chi_{\text{Red}}^2 = 1.6 \cdot 10^6$.

7.5 Adjusting for the paramagnetic contribution

Figure 7.3 and 7.7 show that the susceptibility models of the boleite system do not match the measured susceptibility. An explanation of this mismatch could be that the samples contain a small amount of paramagnetic spins, coming from disorder in this natural system.

If the samples contain paramagnetic spins as well as interacting spins, the susceptibility curve should be a combination of the two. A combined susceptibility model based on a combination of paramagnetic spins and triangles of antiferromagnetic coupled spins are therefore fitted to the data. The combined model takes the weighted sum of the susceptibility from a triangle of spins χ_{tria} , coupled with J_1 , and the susceptibility of three paramagnetic spins χ_{para} . Hereby the susceptibility can be fitted accordingly

$$\chi_{\text{fit}} = \chi_0 ((1 - \rho)\chi_{\text{tria}} + \rho\chi_{\text{para}}), \quad (7.25)$$

where $\rho \in [0, 1]$ is the weight factor, and χ_0 is the scaling factor. ρ directly gives the percentage of paramagnetic spins compared to antiferromagnetic triangle spins, since χ_{para} is the susceptibility of three paramagnetic spins. The model is not taking the J_2 coupling into account, and so it is only valid where $k_B T \gg J_2$.

The data from a sample (in this case crystal K measured at PSI MPMS) is first fitted between $T = 60$ K and $T = 300$ K with a combined model, as shown in figure 7.8. The figure shows

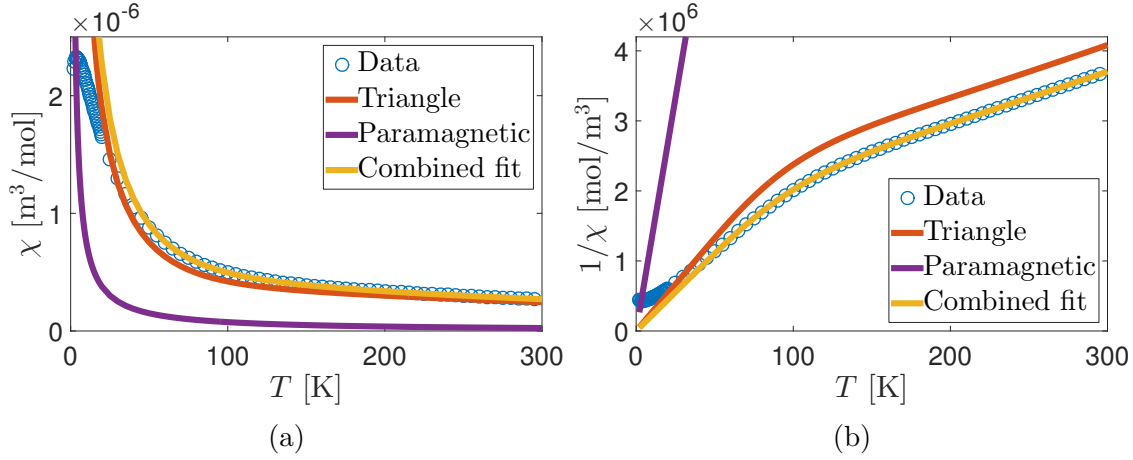


Figure 7.8: The susceptibility (a) and inverse susceptibility (b) from sample K measured at PSI MPMS (data). The data is fitted according to equation (7.25) (combined fit), with $J_1 = 19.9$ meV and $\rho = 0.062$. The contribution to the combined model from the single triangle model $\chi(\rho - 1)\chi_{\text{tria}}$ (Triangle) and paramagnetic model $\chi(\rho - 1)\chi_{\text{para}}$ (Paramagnetic) are shown in the figures as well.

that it is possible to describe the susceptibility above $T = 60$ K by adding a small paramagnetic contribution to the triangle model. In the case with the crystal K presented in figure 7.8, the data seems describable if 6.2 % of the total number of spins are paramagnetic. From the fit, the paramagnetic contribution to the susceptibility, $\chi_0\rho\chi_{\text{para}}$, can be found and subtracted from the raw data χ accordingly

$$\chi_{\text{adj}} = \chi - \chi_0\rho\chi_{\text{para}}. \quad (7.26)$$

In figure 7.9, χ_{adj} is shown together with the triangle contribution to the fit $\chi_0(1 - \rho)\chi_{\text{tria}}$.

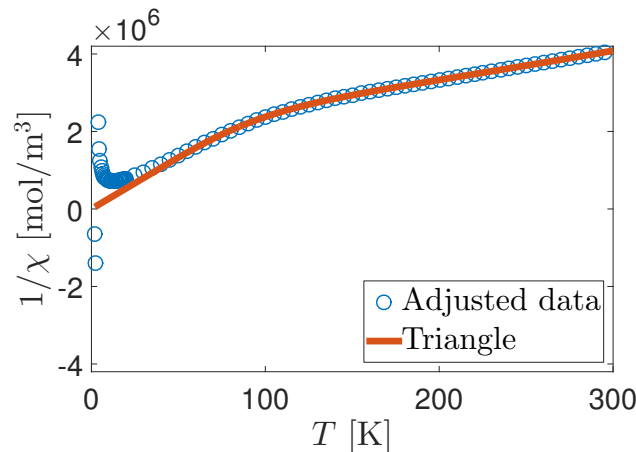


Figure 7.9: Adjusted data $1/\chi_{\text{adj}}$ from sample K found according to equation (7.26). The paramagnetic contribution, which was used to find $1/\chi_{\text{adj}}$, is found from fitting according to equation (7.25). The adjusted data is over plotted with the triangle contribution to the fit $1/(\chi_0(1 - \rho)\chi_{\text{tria}})$ (Triangle), where $J_1 = 19.9$ meV.

Figure 7.9 shows that at low temperatures $T < 2.5$ K, the inverse susceptibility data have negative values. The negative values arise from the subtraction of the paramagnetic contribution. In the low temperature limit, the paramagnetic contribution as well as the crystal susceptibility data are very large, but the difference is very small. Due to this, a small misfit of the paramagnetic contribution gives a negative value of $1/\chi_{\text{adj}}$ in the low temperature limit.

χ_{adj} was found for all measured samples. Appendix C shows how the paramagnetic contribution was found and subtracted from the raw data for all samples.

7.5.1 Fitting the CVT model to the adjusted data

The boleite crystals were in chapter 6 separated into two different types, showing different susceptibility. In the following the two types are analyzed separately. The CVT model (described in the previous section) was attempted fitted to the $1/\chi_{\text{adj}}$ curves, from all crystals where the paramagnetic contribution was present ($\rho > 0$). The CVT model and the $1/\chi_{\text{adj}}$ curves are shown for type 1 and type 2 crystals in figure 7.10 and 7.11 respectively. Similarly to what was observed for crystal K above, the figures show that the subtraction of the paramagnetic contributions fail at very low temperatures for all crystals, resulting in negative $1/\chi_{\text{adj}}$ values.

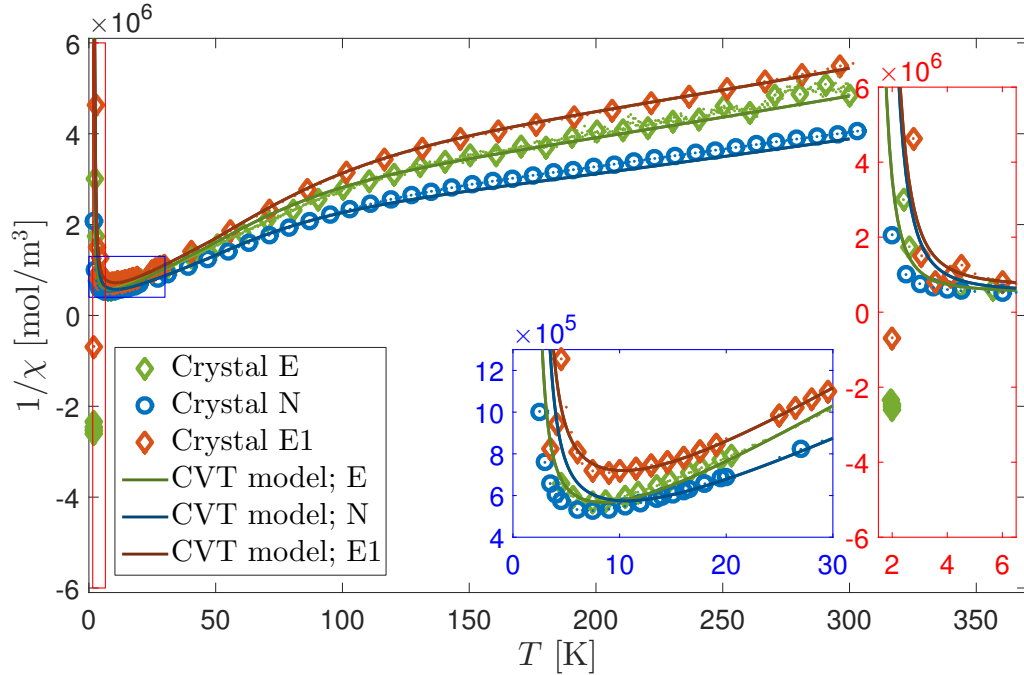


Figure 7.10: Type 1 crystals' $1/\chi_{\text{adj}}$, found according to equation (7.26), fitted with the CVT model. Only data from crystals where it was possible to fit the CVT model are included. The result of the fits are given in table 7.3. The instrument used to measure the data is given by the colors, where green is PSI PPMS, red is EPFL MPMS, and blue is PSI MPMS. The red and blue rectangle show different zoom-in on the low temperature area.

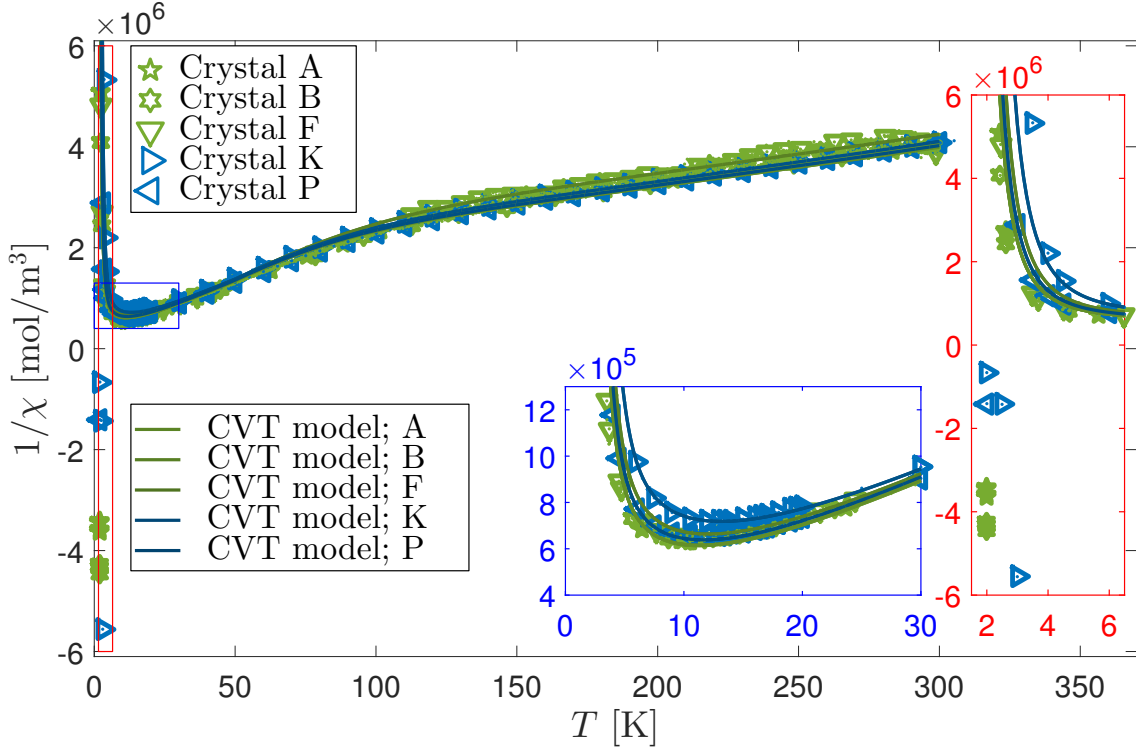


Figure 7.11: Type 2 crystals' $1/\chi_{\text{adj}}$, found according to equation (7.26), fitted with the CVT model. The result of the fits are given in table 7.3. The data color reflects the instrument used to measure the data, where green is PSI PPMS and blue is PSI MPMS. The red and blue rectangle show different zoom-in on the low temperature area. Only data from crystals where it was possible to fit the CVT model are included in this figure. Each of the crystals' data and fits can be seen separately in appendix C.

The results of the fits from figure 7.10 and 7.11 are shown in table 7.3. As the table shows, it was possible to fit the CVT model to the susceptibility curve from all type 2 crystals with $\rho > 0$. For type 1 crystals, it was not possible to fit all $1/\chi_{\text{adj}}$ curves with the CVT model even when $\rho > 0$. Both the EPFL MPMS and the PSI MPMS measurement of crystal H showed that the adjusted data had $1/\chi_{\text{adj}} \rightarrow 0$ when $T \rightarrow 0$ K, making it impossible to fit a CVT model with $J_2 > 0$ meV. The success of the subtraction of the paramagnetic contribution seems closely connected with what instrument the susceptibility curve was measured at. For 8 out of 9 susceptibility curves measured at the two PSI instruments, it was possible to find and subtract the paramagnetic contribution from the data. For the EPFL measurements, it was only 2 out of 4 curves where a paramagnetic contribution were identified. No paramagnetic contribution could be identified in the AU data.

Type 1 crystals						Type 2 crystals					
Crystal	m [mg]	ρ	J_1 [meV]	J_2 [meV]	χ_{Red}^2	Crystal	m [mg]	ρ	J_1 [meV]	J_2 [meV]	χ_{Red}^2
E [‡]	403	0.119	19.6	2.5	0.3	A [‡]	355	0.038	20.2	3.3	1.4
H [§]	226	0.065	-	-	-	B [‡]	424	0.037	18.9	3.3	1.0
N [§]	245	0.054	17.7	3.0	$4.3 \cdot 10^6$	D [‡]	605	0.000	-	-	-
H1 [*]	197	0.015	-	-		F [‡]	287	0.037	20.3	3.2	0.4
E1 [*]	137.1	0.124	21.9	2.9	$7.3 \cdot 10^5$	K [§]	263	0.062	18.2	3.7	$1.3 \cdot 10^5$
S1 [†]	76.4	0.000	-	-		P [§]	236	0.048	19.3	3.4	$1.4 \cdot 10^5$
						C1 [*]	118.8	0.000	-	-	-
						P1 [*]	9.1	0.000	-	-	-
						M1 [†]	84.2	0.000	-	-	-

Table 7.3: The results from adjusting the data for the paramagnetic contribution. ρ is found from fitting χ_{fit} from equation (7.25) to the raw susceptibility data. The paramagnetic contribution is subtracted from the raw data according to equation (7.26), and χ_{adj} is obtained. The χ_{adj} data was fitted with CVT model. J_1 and J_2 are given where the fit converge. and where the fit did not converge is marked with "-". The χ_{Red}^2 is given for every fit that converged, and is estimated for $T > 3$ K. The large difference is commented upon in the main text. The susceptometer used to measure the data is given by the marker in the crystal name: ‡ - PSI PPMS, § - PSI MPMS, * - EPFL MPMS, and † - AU PPMS.

In table 7.3 a large difference between the values of χ_{Red}^2 is observed. The large difference originates from the instrument, where the PSI PPMS (crystal E, A, B, and F) has an average error per measuring point of the inverse susceptibility of $\delta_{\text{PPMS}} \approx 2 \cdot 10^5 \text{ mol/m}^3$, the PSI and EPFL MPMS (crystal N, H1, K, P) have an average error of $\delta_{\text{MPMS}} \approx 6 \cdot 10^2 \text{ mol/m}^3$. The squared ratio of errors from the two instruments are $R_\delta = \left(\frac{\delta_{\text{PPMS}}}{\delta_{\text{MPMS}}}\right)^2 \approx 1 \cdot 10^5$. Due to the small error on the MPMS data, even small systematic uncertainties in the χ_{adj} data, of which one is the paramagnetic subtraction, can create a large χ_{Red}^2 . These systematic uncertainties will not be studied further. It is however clear from the consistency between the range of type 2 crystals' datasets and the models, that the behavior of the data in figure 7.11 is well described by the model above $T = 3$ K.

To compare the two different instrument types' data sets, a new normalized MPMS χ_{Red}^2 is defined as $\chi_{\text{A}}^2 = \chi_{\text{Red}}^2 / R_\delta$.

The procedure with finding the paramagnetic contribution, and subtracting it from the raw data, seems to work well for the type 2 crystals. As figure 7.11 shows, the CVT model fits the type 2 crystals' $1/\chi_{\text{adj}}$ very well above $T > 3$ K with $\chi_{\text{A}}^2 < 1.4$, and for the crystals with $\rho > 0$, the $1/\chi_{\text{adj}}$ curves are almost identical. For type 1, the procedure seems to be less efficient, as the CVT model does not fit the data very well. For 2 of the 3 type 1 crystals where it was possible to fit the CVT model, it resulted in a very large χ_{Red}^2 . For crystal N $\chi_{\text{A}}^2 = 43$ and E $\chi_{\text{A}}^2 = 7.3$. The CVT model therefore seems to fit the type 2 crystals' χ_{adj} better than the type 1 crystals' χ_{adj} .

In table 7.4, the results from table 7.3 are averaged, and afterwards compared to the results

from the CVT model fit to the raw data and the Curie Weiss fit to both the raw data and the χ_{adj} . The CVT model fits χ_{adj} much better than the raw data: When the CVT-model was fitted to the raw data from sample K it revealed a $\chi_{\text{Red}}^2 = 1.6 \cdot 10^6$. The CVT model fitted to the χ_{adj} of sample K had $\chi_{\text{Red}}^2 = 1.3 \cdot 10^5$.

The average result of the CVT model fitted to the type 2 crystals' χ_{adj} seems to be the best estimate of the exchange constants in the boleite system. The CVT model predicts, from the type 2 crystals' χ_{adj} curves, that $J_1 = 19.4 \pm 0.4$ meV and $J_2 = 3.4 \pm 0.1$ meV. The estimate gives a ratio $\frac{J_2}{J_1} = 0.175 \pm 0.005$. This is somewhat on the limit for the assumption that $\frac{J_2}{J_1} \ll 1$, which the CVT model relies on, as illustrated in figure 7.5. Even so, the exchange constants found from fitting the CVT model to the type 2 crystals' χ_{adj} are the best estimate of the actual size of the exchange constants in boleite.

Taking the average of weight factor of paramagnetic spins ρ from table 7.3 for each of the two types where the fit succeeded, we find $\bar{\rho}_1$ for type 1 crystals and $\bar{\rho}_2$ for type 2 crystals:

$$\begin{aligned}\bar{\rho}_1 &= 0.09 \pm 0.02, \\ \bar{\rho}_2 &= 0.044 \pm 0.005.\end{aligned}\tag{7.27}$$

The average only includes the datasets where the CVT model could be fitted after the subtraction of the paramagnetic contribution. From the result, it is clear that there is a significant difference in the amount of paramagnetic spins between type 1 and type 2 crystals.

The two different boleite crystal types have quite similar average coupling constants, as shown in table 7.4. Combining this with the size of $\bar{\rho}_1$ and $\bar{\rho}_2$, it seems to indicate that the difference between the two types of crystals is due to a paramagnetic contribution to the susceptibility. This will be discussed further in chapter 10.

	Curie Weiss model (type 2 crystals - raw data).	Curie Weiss model (type 2 crystals - χ_{adj}).	CVT model (type 2 crystals - raw data).	CVT model (type 1 crystals - χ_{adj}).	CVT model (type 2 crystals - χ_{adj}).
J_1 [meV]	36 ± 2	35 ± 2	24.9 ± 0.2	20 ± 1	19.4 ± 0.4
J_2 [meV]	3.6 ± 0.1	3.6 ± 0.4	1.3 ± 0.1	2.8 ± 0.2	3.4 ± 0.1

Table 7.4: Comparison between fit results from five different susceptibility models. The five models are: The Curie Weiss fit to the raw susceptibility data from the two type 2 crystals K and P, as shown in figure 6.4. The CVT model (the combined isolated triangle and variational model) fitted to the raw susceptibility data from the two type 2 crystals K and P, as shown in figure 7.7. The average result of fitting the CVT model and the Curie Weiss models to all crystals' χ_{adj} data. χ_{adj} is given in equation (7.26). The results from fitting the CVT model to χ_{adj} from type 1 and type 2 crystals are both included. The fit parameters for each of the fits of the crystals' χ_{adj} are given in table 7.3, and the fits are shown in figure 7.10 and 7.11.

7.6 The flaws of the Curie Weiss model

Table 7.4 shows that there is a discrepancy between the results obtained when fitting the boleite type 2 crystals' data with Curie Weiss models and when fitting with the quantum mechanical models.

The problem is twofold, and the result is that the estimate of the coupling strength from the Curie Weiss lines is wrong, since the assumption $T_N = -\Theta_{CW}$ is not valid, which is a requirement to use equation (4.3). In the following the ordering temperature T_N will be used for the transition temperature where the small 12 spin and 3 spin system is undergoing a transition into their low energy states. T_N is calculated according to the prediction of the ordering temperature in long range ordering systems from equation (4.3) so that $T_N = \frac{\sum_i J_i}{4k_B}$.

The first problem is that the fits are made too close to T_N . The problem is illustrated in figure 7.12a, where the expected inverse susceptibility from a triangle of spins is fitted with a Curie Weiss line both at extremely high temperatures $40 T_N > T > 42 T_N$ and close to the transition temperature $2 T_N > T > 3 T_N$. It is clearly seen from the figure that the inverse susceptibility does not follow a straight Curie Weiss line all the way from $T_N < T < 40 T_N$, and that the deviation becomes significant below $3 T_N$. The closer to T_N the Curie Weiss line is fitted to the data, the larger $-\Theta_{CW}$ becomes, and thereby also the estimated exchange constant. When fitting a Curie Weiss line to temperature of $2 T_N > T > 3 T_N$, the result is that the Curie Weiss estimate of the exchange constant is around twice the size of what the actual exchange constant is. It is also seen that even when fitting the Curie Weiss model to extremely large temperatures, the estimated coupling strength still deviates around 5% from the actual exchange constant used in the model. The second problem is the assumption that the full boleite spin system is in a paramagnetic state in the region between the two transition temperatures. The behavior of the low temperature inverse susceptibility of the spin triangles is like a paramagnet, but unlike a normal $S = 1/2$ paramagnet the triangles still have 4 degrees of freedom. Additionally, the $\hat{S}_3^+ \hat{S}_4^-$ inter triangle term does not behave as the $\hat{S}_1^+ \hat{S}_2^-$ term for free spins.

Combined, the two problems result in a miscalculation of the exchange constants J_2 and J_1 from the Curie Weiss models. The size of the problem is illustrated in figure 7.12b, where Curie Weiss lines are fitted to a 12 spin model like the model presented in figure 7.1c. The exchange constants are found from the Curie Weiss fits in the same way as they were for the boleite system, where they were calculated according to equation (6.2). The result is that the estimated J_1 is twice as large as the J_1 used in the model, which corresponds with what was found for the single triangle model when fitted to close to T_N . The estimated J_2 coupling is reasonably close to the models actual J_2 .

Using this knowledge, it is likely that the results from equation (6.3) are wrong, and that the Curie Weiss model overestimates J_1 by a factor of ~ 2 . This is indeed what is observed in e.g. table 7.4.

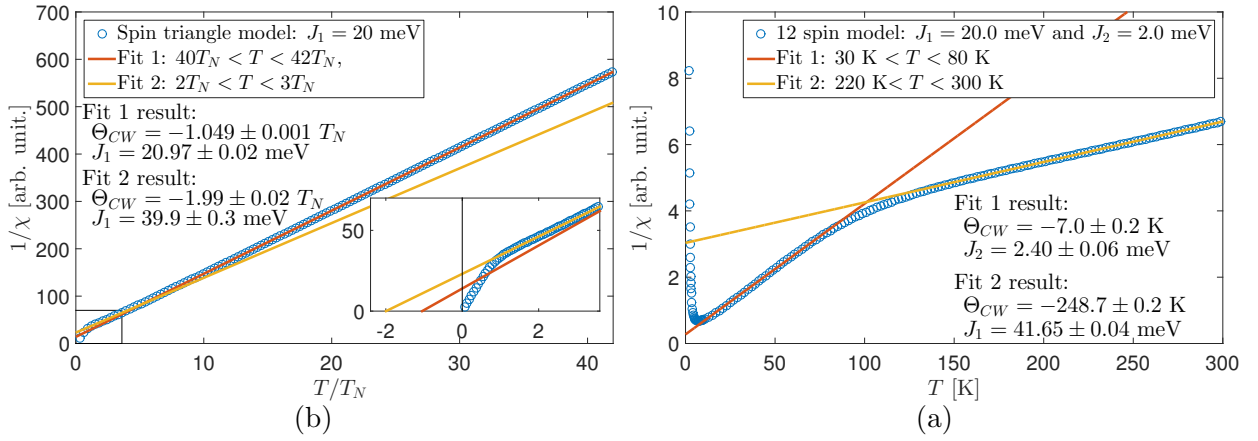


Figure 7.12: Discrepancy between the actual coupling constants, and the ones found from Curie Weiss fits when fitted to the expected inverse susceptibility from a system with spin triangles. The models' parameters are given in the legends. The fits' Curie Weiss temperature Θ_{CW} and the exchange constant calculated from Θ_{CW} are given in the inserted text. The exchange constants are calculated according to equation (6.2). (a) A single triangle model as function of temperature normalized to $T_N = \frac{J_1}{2k_B} = 116.05$ K, fitted with a Curie Weiss line at extreme temperatures and close to T_N . A zoom in on the temperature region $-2.5 T_N < T < 3.5 T_N$ is shown in the inserted figure. (b) Curie Weiss fits to low and high temperature regions (given in legends) of a 12 spin model.

CHAPTER 8

Other bulk experiments

The DC-susceptibility experiments revealed a clear magnetic signal, which in the previous chapter showed to be describable with the variational model. This chapter will in brief introduce the results and models of other bulk measurement techniques.

8.1 The heat capacity

The heat capacity at constant pressure C_P of the boleite type 2 crystal M1 was measured at the AU PPMS. The temperature normalized heat capacity $C_P(T)/T$ from crystal M1 is shown in figure 8.1. The thermal expansion of boleite is assumed small enough that $C_V \approx C_P$. The heat capacity should hence be describable with the model $C_V = C_{\text{Lat}} + C_{\text{Mag}}$, from equation (4.10).

The lattice heat capacity C_{Lat} can be calculated from equation (4.11). The magnetic heat capacity is calculated using equation (4.14). To minimize the amount of variables, the magnetic contribution is calculated from a model which combines the heat capacity from the 8 isolated triangles and the variational model with fixed $J_1 = 19.4$ meV and $J_2 = 3.4$ meV. The fitted model therefore only needs 3 parameters; two scaling parameters (a , b) and the Debye temperature Θ_D , so that

$$C_V = aC_{\text{Lat}}(\Theta_D) + bC_{\text{Mag}}. \quad (8.1)$$

The importance of the scaling parameters has not been assessed. The model is shown fitted to the data in figure 8.1a, and both model and data show a clear upturn with decreasing temperature in the measured C_P/T at low temperatures. Debye's model of the heat capacity (equation (4.11)), predicts that the lattice heat capacity normalized with temperature C_{Lat}/T at low temperature should follow a T^2 behavior. An upturn with decreasing temperature is therefore a clear indication of a magnetic contribution to the heat capacity of the crystal.

In the figure, the C_V model seems to show a similar pattern as the data, but it has not been able to make a complete fit. The model shows that the magnetic contribution to the heat capacity is very small compared to the lattice contribution, except at low temperatures. The magnetic heat capacity causes a significant increase in the combined heat capacity as the temperature is lowered. It is impossible to find the exchange constants from a single heat capacity measurement on a boleite crystal, but it is possible to get some information of the magnetic system from the heat capacity. Figure 8.1b shows that the increase in C_{Mag}/T is caused by the ordering of the 24 spin system at low temperature. The temperature normalized heat capacity from a spin triangle decreases with decreasing temperature at $T < 100$ K, whereas the temperature normalized heat capacity of the 8 coupled triangles, predicted by the variational model, increases with decreasing temperature.

As a consistency check, figure 8.1b also shows the predicted temperature normalized heat capacity from the 12 spin model presented in the previous chapter in figure 7.1c. The combined result of the variational model and the triangle model predicts a similar heat capacity normalized with temperature as the 12 spin model at $T > 10$ K as is clearly seen from the figure. There is a small discrepancy between the variational model and the 12 spin model at $T < 10$ K. The observation is consistent with the observed behavior of the susceptibility calculated from the three models, presented in chapter 7.

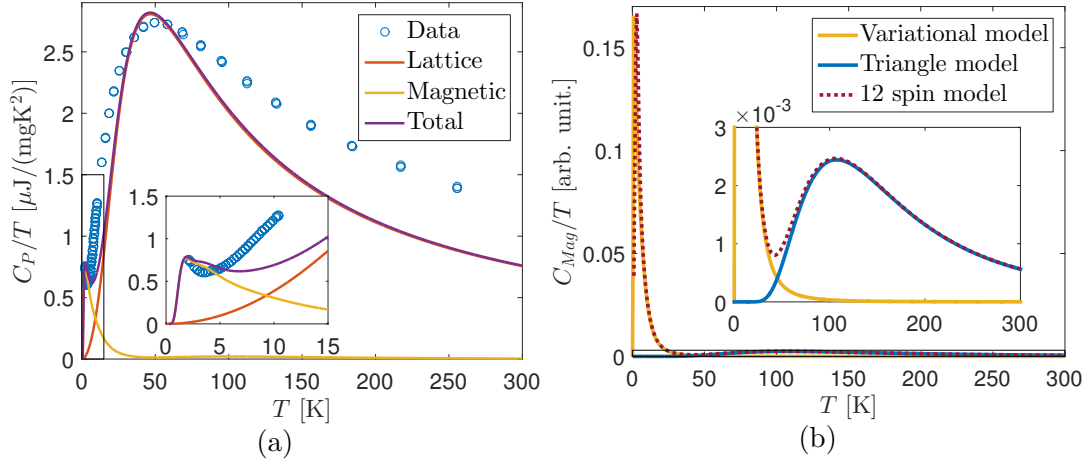


Figure 8.1: The heat capacity of boleite. (a) The measured heat capacity from crystal M1 (Data) fitted with a heat capacity model (Combined) according to equation (8.1). The magnetic heat capacity model (Magnetic) is calculated with exchange constants fixed at $J_1 = 19.4$ meV and $J_2 = 3.4$ meV. The lattice contribution (Lattice) is calculate from the Debye model in equation (4.11), and the best fit shows $\Theta_D = 166.8$ K. The scaling parameters of the shown fit are $a = 0.04$ and $b = 7.9$. (b) The magnetic heat capacity contribution C_{Mag} separated into its two components, plotted together with the 12 spin model's prediction of the heat capacity (12 spin model). The magnetic model is a combined model of a triangle model (Triangle model) and the variational model (Variational model). All models are normalized to the number of spins in them. The insert is a zoom-in on small C_{Mag}/T .

8.2 The magnetization as function of field

Crystal E1's and P1's magnetization as function of magnetic field were measured on the EPFL MPMS at $T = 1.5$ K. E1 is a type 1 crystal, and P1 is a type 2 crystal. The results of the experiments are shown together with the result from the variational model with $J_2 = 3.4$ meV and a spin triangle model with $J_1 = 19.4$ meV in figures 8.2 and 8.3. Due to the small variation in the magnetization data compared to a straight line, the comparison between the models and crystal magnetization is made in three steps: First a straight line is fitted to the model and crystal data. Secondly, the straight line is subtracted from the data. Last, the residual of the model data is scaled to the residual of the crystal data.

It was not possible to fit the data properly with the models, but a clear tendency is seen from the figures. The type 1 crystal's magnetization curve follows a behavior around a straight line which resembles the one seen from the triangle model. It should be mentioned that at temperatures of 1.5 K and an external field $|B| \leq 7.9$ T, the magnetization curve of a triangle model, with $J_1 = 19.4$ meV, and a paramagnetic model are completely alike in shape.

The type 2 crystal's magnetization curve seems to behave more like the variational model's magnetization curve. The variational model shows a large deviation from the data at $|B| > 4$ T. The deviation could originate from a paramagnetic contribution to the magnetization curve of the type 2 crystal, similar to the paramagnetic contribution seen in the susceptibility data.

From the magnetization as function of magnetic field at $T = 1.5$ K, it seems that ordering of the 24 spins is suppressed in the type 1 crystals. The type 2 crystal's magnetization shows an ordering, but also a contribution from what might be paramagnetic spins. The observation is in correspondence with the observed behavior from the susceptibility in chapter 7.

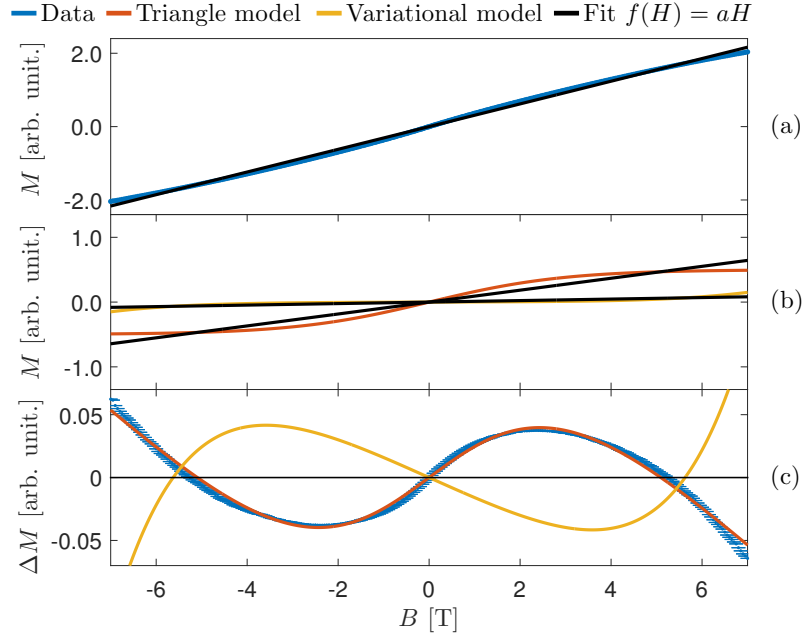


Figure 8.2: Magnetization as function of field at $T = 1.5$ K of the type 1 crystal E1 compared to the expected magnetization of the 24 spin variational model with $J_2 = 3.4$ meV, and a spin triangle model with $J_2 = 19.4$ meV. (a-c) have a common x-axis, and the legend is given on top of the figures. (a-b) The raw magnetization data and theoretical magnetization models fitted with straight lines $f(H) = aH$. (c) Difference between magnetization curve and fitted line $\Delta M = M - f(H)$. The theoretical models are scaled to fit the data.

8.3 The AC-susceptibility.

Dilution fridge cooling was used to measure the magnetic susceptibility down to temperatures of $T \sim 0.29$ K. It has only been possible, within the time frame of this project, to have one successful measurements at the EPFL AC-susceptometer at dilution fridge temperatures. The measured crystal was the type 1 crystal H1. Crystal H1 showed in the previous chapter to behave differently from most other crystals, since it was not possible to fit the CVT model even after the paramagnetic contribution was removed. In this section, the amount of impure defect spins (ie. paramagnetic spins) is found from the AC susceptometers dilution fridge data. The procedure to do this has been tried on other systems like Spangolite in reference [52].

I will in the following call crystal H1 susceptibility measured on the MPMS at EPFL, for the MPMS susceptibility. The AC susceptibility measured at dilution fridge temperatures will be called AC-dilution susceptibility. The MPMS susceptibility is measured within the temperature range $1.5 \text{ K} < T < 300 \text{ K}$. The AC-dilution susceptibility is measured within the temperature range $0.3 \text{ K} < T < 8 \text{ K}$. As mentioned in chapter 4, the AC-susceptometer finds the susceptibility

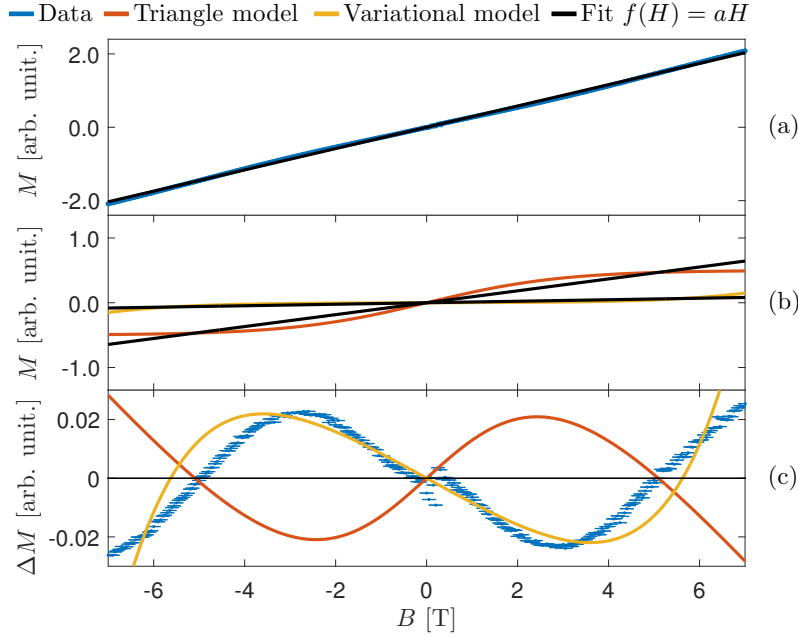


Figure 8.3: Magnetization as function of field at $T = 1.5$ K of the type 2 crystal P1 compared to the expected magnetization of the 24 spin variational model with $J_2 = 3.4$ meV, and a spin triangle model with $J_2 = 19.4$ meV. (a-c) have a common x-axis, and the legend is given on top of the figures. (a-b) The raw magnetization data and theoretical magnetization models fitted with straight lines $f(H) = aH$. (c) Difference between magnetization curve and fitted line $\Delta M = M - f(H)$. The theoretical models are scaled to fit the data.

by measuring the change in magnetization. This results in the AC-dilution susceptibility is scaled and offset differently from the MPMS susceptibility.

Using the exact same approach as in reference [52], the AC-dilution susceptibility is scaled to fit the MPMS data in their overlapping temperature region, $T = 1.5$ K $< T < 8$ K. The scaling can be seen in figure 8.4a. The scaling is performed by first fitting a straight line to the inverse of the MPMS susceptibility. The inverse of the AC-dilution susceptibility is forced to fit this straight line by subtracting a constant background, then multiplying a scaling parameter, and last offsetting the data.

The combined inverse susceptibility data is covering the entire range 0.3 K $< T < 300$ K. The scaling of the dilution data works reasonably well, but the correspondence between the two datasets is not perfect. The combined inverse susceptibility shows a kink at $T \sim 2.5$ K, and below this kink a linear dependency of temperature is observed, with $1/\chi \rightarrow 0$ for $T \rightarrow 0$. This behavior is sometimes referred to as a Curie tail. A curie tail in the susceptibility can be caused by defect spins.

The combined data's Curie tail is fitted with a Curie Weiss line (equation (4.6)), as shown in figure 8.4b. The best fit has a Curie Weiss temperature of $\Theta_{CW} = 0.29 \pm 0.03$ K, which indicates that the defect spins are slightly ferromagnetic. This could, however, be due to the scaling of the dilution fridge data. Using equation (4.5), the number of participating magnetic spins per unit volume, that causes the Curie tail, is found to be $N = 3.0 \pm 0.1$. Comparing this to the expected number

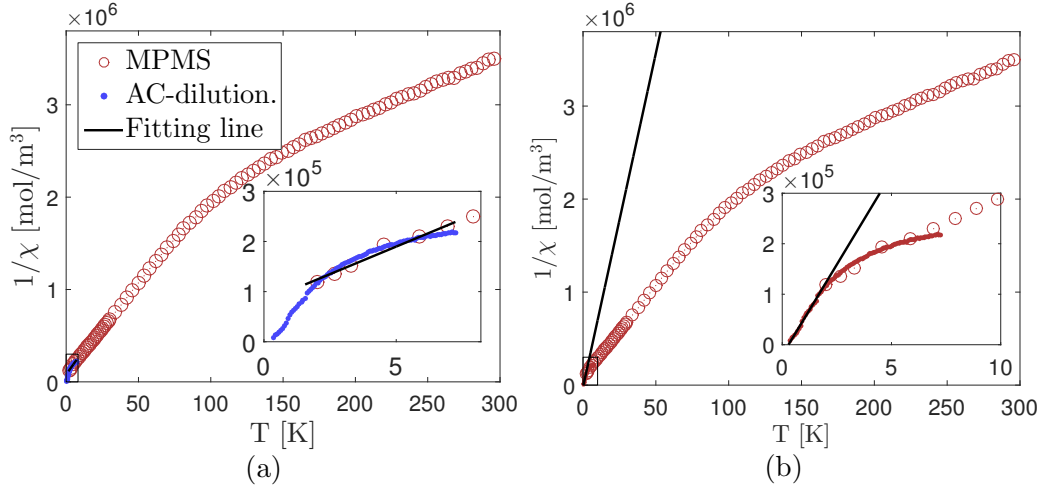


Figure 8.4: Inverse susceptibility from crystal H1 measured on the AC-susceptometer at temperatures $0.3 \text{ K} < T < 8 \text{ K}$ (AC-dilution) and MPMS susceptibility measured at $1.5 \text{ K} < T < 300 \text{ K}$. Both experiments were performed at EPFL. The inserted plots are zoom-ins on low temperatures. (a) The inverse AC-dilution susceptibility is scaled to fit the inverse MPMS susceptibility in the overlapping temperature region, as explained in the main text. (b) The inverse of the combined AC-dilution and MPMS susceptibility (red points) is fitted with a Curie Weiss line (black line) below $T < 2.5 \text{ K}$, according to equation (4.6). The parameters of the fitted line are $C = (1.39 \pm 0.04) \cdot 10^{-5} \text{ m}^3/\text{mol}$ and $\Theta_{\text{CW}} = 0.29 \pm 0.03 \text{ K}$.

of magnetic spins in the boleite unit cell, ie. 24, the ratio of defect spins to the total spins is

$$\rho_D = 0.123 \pm 0.004. \quad (8.2)$$

The small error comes from the error on the fit to the adjusted dilution data, and it does not include possible systematic errors from fitting the dilution data to the MPMS data. ρ_D is almost 30 % larger than the average amount of paramagnetic spins found in the preceding chapter where the type 1 crystals $\bar{\rho}_1 = 0.09 \pm 0.02$. ρ_D is also much larger than the ratio of paramagnetic spins in crystal H1 $\rho_{H1} = 0.015$, found by fitting a combined paramagnetic and triangle model in the preceding chapter.

The Curie Weiss line found from the dilution data can be subtracted from the raw data, as done for the paramagnetic contribution in the previous chapters. The resulting defect-spins-adjusted data can be seen in figure 8.5. The defect-spins-adjusted data can afterwards be fitted with the CVT model. In the figure, the CVT model is tried fitted with fixed $J_1 = 19.4 \text{ meV}$ and $J_2 = 3.4 \text{ meV}$. The fit is very bad with a $\chi_{\text{Red}}^2 = 1.0 \cdot 10^8$, which is 1000 times larger than the fit to $1/\chi_{\text{adj}}$. The best fit to the defect-spins-adjusted data is found at $J_1 = 15.4 \text{ meV}$ and $J_2 = 1.8 \text{ meV}$, which is significantly different from the results seen in the previous chapter. The CVT model is not fitting the high temperature susceptibility very well, and the fit to the MPMS data at $3 \text{ K} < T < 300 \text{ K}$ has $\chi_{\text{Red}}^2 = 3.7 \cdot 10^5$. This is 3 times larger than the χ_{Red}^2 from comparable results from the CVT model fit to the type 2 crystals' $1/\chi_{\text{adj}}$. At temperatures $T < 100 \text{ K}$, the fit is decent, but as it was the case with the subtraction of paramagnetic contribution in the previous chapter, the subtraction result in a negative susceptibility values.

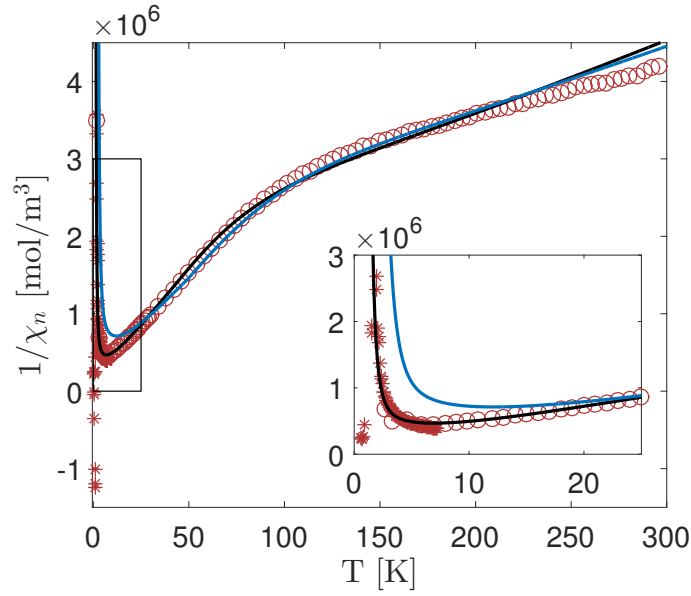


Figure 8.5: The inverse of the defect-spin-corrected susceptibility (red). The defect-spin-corrected susceptibility is found from subtracting the Curie Weiss line, with $C = (1.39 \pm 0.04) \cdot 10^{-5} \text{ m}^3/\text{mol}$ and $\Theta_{CW} = 0.29 \pm 0.03 \text{ K}$ from the combined AC-dilution and MPMS susceptibility from figure 8.4. The inverse of the defect-spin-corrected susceptibility is fitted with the CVT model (black). The parameters of the best fit result is $J_1 = 15.4 \text{ meV}$ and $J_2 = 1.8 \text{ meV}$. The best fit has $\chi_{\text{Red}}^2 = 3.7 \cdot 10^5$. The CVT model is also plotted with fixed $J_1 = 19.4 \text{ meV}$ and $J_2 = 3.4 \text{ meV}$ (blue). The fixed CVT model has $\chi_{\text{Red}}^2 = 1.0 \cdot 10^8$. The inserted plot is a zoom-in on the low temperature susceptibility. The χ_{Red}^2 is in both cases calculated from the correspondence with the EPFL MPMS data $3 \text{ K} < T < 300 \text{ K}$.

CHAPTER 9

Neutron scattering results

To further investigate the magnetic structure in boleite, a series of neutron scattering experiments were conducted. The aim was to identify elastic and inelastic structures, which could confirm our theories on the boleite system. This chapter will show the results obtained from neutron experiments, as well as introducing theoretical estimates of the scattering from boleite.

9.1 The expected magnitude of the neutron signal

It is expected that the magnetic scattering from boleite is very weak compared to the nuclear incoherent scattering due to the large amount of hydrogen in boleite.

The expected total nuclear incoherent scattering cross section of boleite is calculated to be $\sigma_{\text{inc,tot}} = 4285.2 \cdot 10^{-24} \text{ cm}^2$ using equation (5.23) and table 9.1. The magnetic scattering cross section is found from equation (5.48) and is $\sigma_{\text{mag}} = 43.8 \cdot 10^{-24} \text{ cm}^2$. The ratio between the magnetic signal and the incoherent background is

$$\frac{\sigma_{\text{mag}}}{\sigma_{\text{inc,tot}}} = 0.010. \quad (9.1)$$

This shows that the magnetic scattering from boleite should be very weak.

9.2 Neutron experiments

A large variety of neutron scattering experiments were conducted to try to detect a signal arising from magnetic ordering and excitations in boleite. Temperature dependence of the elastic scattering was measured on the triple axis spectrometer RITA-II and IN3, as we looked for possible magnetic ordering. The magnetic component of the total diffraction signal was extracted with

Element	Number in boleite's unit cell	$\sigma_{\text{inc}} [10^{-24} \text{ cm}^2]$	$\sigma_{\text{coh}} [10^{-24} \text{ cm}^2]$
H	48	82.03	1.7568
O	48	0.008	4.232
Cl	62	5.3	11.5257
K	1	0.27	1.69
Cu	24	0.55	7.485
Ag	9	0.58	4.407
Pb	26	0.003	11.115

Table 9.1: The incoherent σ_{inc} and coherent σ_{coh} neutron scattering cross section from elements in boleite. The elements' cross sections are from reference [35].

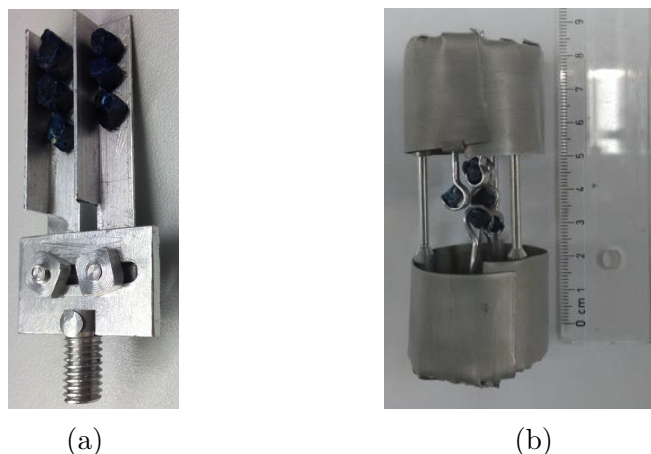


Figure 9.1: Pictures of the sample holders used in the neutron scattering experiments. (a) Sample holder 1: The 6 boleite crystals are glued to the sides of two aluminum bars. (b) Sample holder 2: The 7 boleite crystals are suspended from the "roof" and "floor" of the sample holder, and held by flat aluminum wires squeezed around the crystals. The "roof" and "floor" are kept apart by 3 aluminum pillars. Sheets of cadmium cover the top and bottom of the sample holder in the picture.

polarized neutron scattering on D7. RITA-II was also used to examine the magnetic field dependence of elastic and low energy inelastic scattering. Furthermore, the temperature dependence of the inelastic scattering was measured using the triple axis spectrometer IN8 and the time of flight spectrometer IN4 to look for high energy magnetic excitations arising from excited states of the triangles. Descriptions of the instruments are given in chapter 5. All neutron scattering intensities will be given in arb. unit.

9.2.1 Constructing the sample

To increase the scattering intensity, type 2 crystals were carefully coaligned along $(h\ 0\ 0)$ and $(0\ k\ k)$. Two different aluminum sample holders were used:

- Sample holder 1 contains 6 crystals (A, B, D, F, K, and P) with a total crystal mass of 2165. Sample holder 1 was used at RITA-II measurements of the elastic scattering from boleite.
- Sample holder 2 contains 7 crystals (A, B, D, F, K, O, and P) with a total crystal mass of 2474 mg. Sample holder 2 was used at all measurements at ILL (IN3, IN4, IN8, and D7), and RITA-II measurements of the behavior of elastic and low energy inelastic scattering from boleite in an external magnetic field.

The sample holders are shown in figure 9.1. The construction of the sample holders and coalignment of the crystals were carried out by Sonja Holm and Kenneth Lønbæk before the start of this master thesis project.

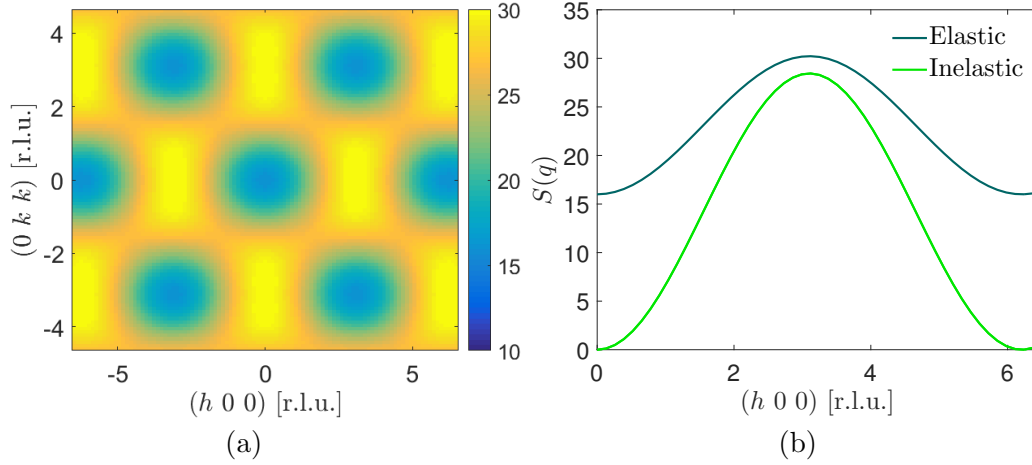


Figure 9.2: The expected $S(\mathbf{q}, \omega)$ from 8 isolated triangles of spins, arranged as in boelite's truncated copper cube, in zero field and $T = 0$ K. **(a)** Surface plot of the elastic structure factor $S(\mathbf{q}, 0)$ as function of $(h k k)$. The inelastic structure factor is similarly shaped but with a zero scattering intensity as minimum. **(b)** Elastic and inelastic structure factor along $(h 0 0)$. The inelastic scattering should be at $\Delta E = \frac{3}{2}J_1$

9.3 The elastic structure and low energy excitations

The magnetic structure factor $S(\mathbf{q}, \omega)$ can be calculated from the eigenstates of a system, according to equation (5.37) and (5.38). The structure factor is a good measure for the total scattering cross section since $\frac{d^2\sigma}{d\Omega dE}|_{\text{magn.}} \propto S(\mathbf{q}, \omega)$ according to equation (5.35).

Mexact can be used to calculate the eigenstates from a given system. I constructed an algorithm which could calculate $S(\mathbf{q}, \omega)$ for an isolated triangle system in an external magnetic field applied along the \hat{z} -direction, at $T = 0$ K, using equation (5.39) to (5.44). The algorithm was used to calculate $S(\mathbf{q}, \omega)$ for a system of 8 isolated triangles, with lattice parameters as the 8 triangles in the truncated boelite cube. The resulting $S(\mathbf{q}, \omega)$ is shown in figure 9.2. The length scale of the elastic $S(\mathbf{q}, 0)$ is of the order of $(6 0 0)$ r.l.u. It has not been possible to calculate the $S(\mathbf{q}, \omega)$ of the entire 24 spin system within the time frame of this project. However, it is possible to estimate the length scale of the scattering pattern from the size of the boelite copper cube. A boelite copper cube has side length 7.15 \AA compared to a unit cell of 15.288 \AA , which should mean that the scattering should be periodic function along $(h 0 0)$ of reciprocal length scale $(\sim 2 0 0)$ r.l.u.

Elastic neutron scattering from boelite, measured at RITA-II, revealed a bulge shape scattering intensity along the $(h 0 0)$ direction, as shown in figure 9.3a. The bulge shape pattern found on RITA-II decreases as temperature is increased from $T = 1.5$ K to $T = 300$ K. On IN3, temperature scans were made for different points in \mathbf{q} -space, revealing a general trend of decreased elastic scattering intensity as the temperature was increased, as shown in figure 9.3b. A bulge shape is also seen in the elastic scattering measured at IN8, as shown in figure 9.4.

Magnetic scattering should decrease with increasing temperature, and at first the shape of the bulge shape in RITA-II data resembles the expected shape of the magnetic structure factor shown in figure 9.2b. The center of the bulge shape found at RITA-II is however placed at $(5 0 0)$ r.l.u. whereas the theoretical estimate is that the peak intensity should be at $(3.1 0 0)$ r.l.u. The bulge

shape has not been measured beyond $(6\ 0\ 0)$ r.l.u., and it is therefore not possible to determine if it is periodic. If it is periodic, its length scale seems to be too large to be magnetic according to our understanding of the system. The total magnetic cross section is predicted to be around 1 % of the incoherent background, and hence, the change in intensity as function of temperature seen in both RITA-II and IN3 data is also too large to be of magnetic origin.

The bulge shapes seen in the IN8 data seem asymmetric around the $(h\ 0\ 0)$ and $(0\ k\ k)$ lines. In a cubic lattice, it is expected that magnetic scattering should be symmetric around the $(h\ 0\ 0)$ and $(0\ k\ k)$ lines, as the theoretical model in figure 9.2a also predicts.

We did not expect long range magnetic order to occur due to the long distance between the magnetic unit cells in boleite. The neutron data do not contradict this theory, as no magnetic Bragg peaks are identified in the elastic measurements.

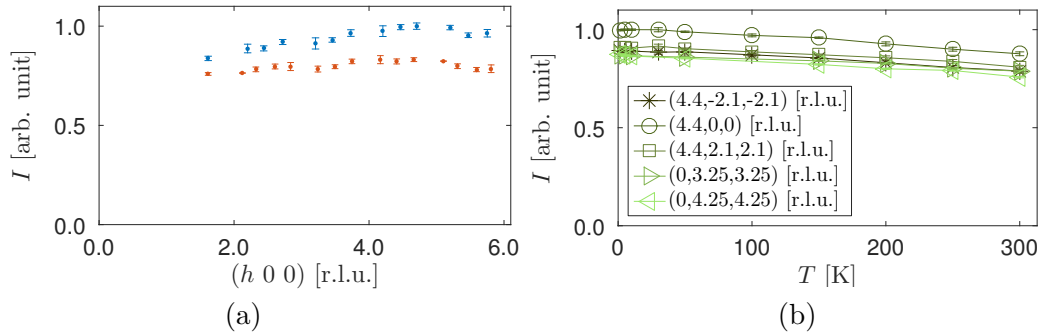


Figure 9.3: Elastic neutron scattering intensity from boleite. (a) Scattering intensity as function of $(h\ 0\ 0)$ for $T = 1.5$ K (blue) and $T = 300$ K (red) measured at RITA-II. Data from all 9 analyzer blades have been combined, the Bragg reflections have been removed, and the data have been binned. (b) Temperature dependence of scattering intensity at 5 different points in reciprocal space (legends), measured on IN3.

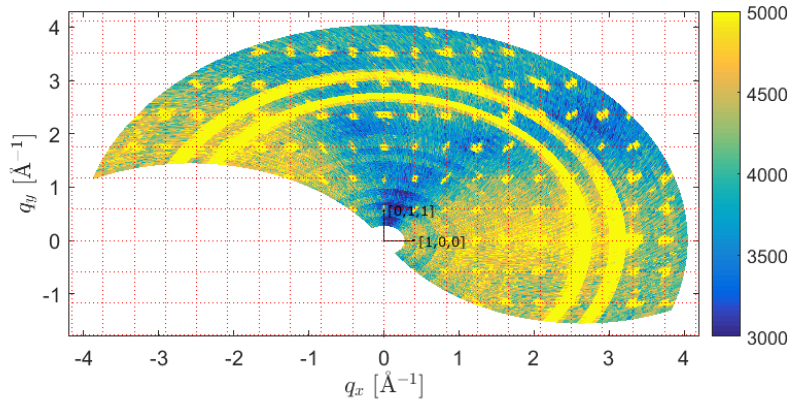


Figure 9.4: Elastic scattering at $T = 1.5$ K measured on IN8. The color scale is shown in the right colorbar, where the intensity is given in arbitrary units. The red grid marks integer values of $(h\ 0\ 0)$ and $(0\ k\ k)$ in r.l.u. The figure shows clear structural Bragg peaks. The two large intensity rings are aluminum powder rings from the sample environment. The clear pattern of two regions with higher intensity is investigated in the polarization analysis section.

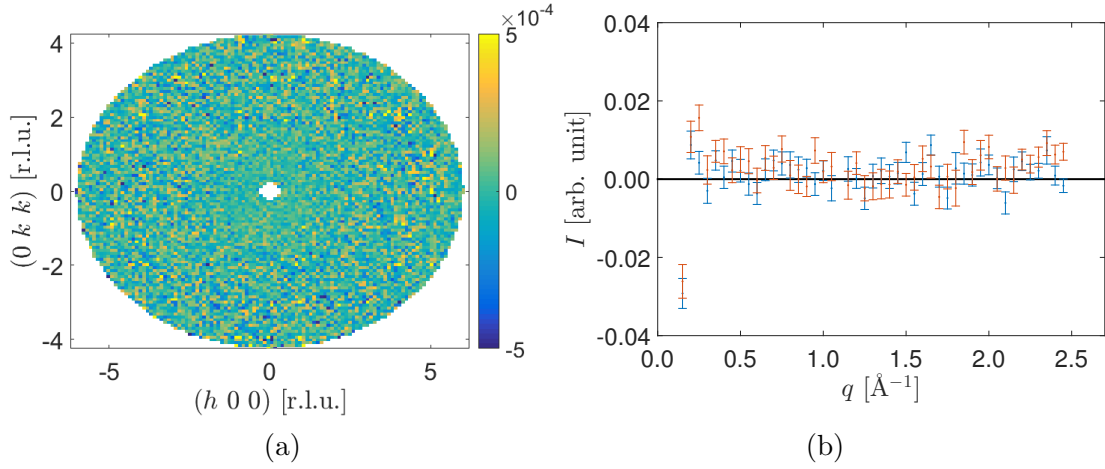


Figure 9.5: The magnetic scattering component from boleite. The intensity is normalized to peak intensity of the NSI scattering component, for $T = 1.5$ K. The magnetic and NSI scattering components are separated with polarized neutron analysis on D7. **(a)** Magnetic scattering component as function of $(h k k)$, at $T = 1.5$ K. **(b)** Powder average of magnetic scattering component of the total scattering from boleite, at $T = 1.5$ K (blue) and $T = 300$ K (red).

9.4 Polarization analysis

Using XYZ polarization analysis on D7, the magnetic, nuclear coherent, and NSI (Nuclear Spin Incoherent) components can be separated from the total energy integrated neutron scattering intensity. The magnetic neutron scattering component does not show any structures in $(h k k)$, as shown for $T = 1.5$ K in figure 9.5a. Figure 9.5b shows that even when taking the powder average of the magnetic component there is no clear difference between $T = 1.5$ K and $T = 300$ K. Integrating the magnetic component across \mathbf{q} , we are able to detect a total magnetic cross section significant larger than zero at $T = 1.5$ K of 6 ± 2 arb. unit. The total magnetic cross section increase with temperature to around 15 ± 3 arb. unit. at $T = 300$ K.

The NSI scattering component was found to be much larger than the magnetic. We find that the total energy and \mathbf{q} integrated magnetic cross section is only 0.10 ± 0.05 % of the total energy and \mathbf{q} integrated NSI cross section. From equation (9.1), the expectation was that the total energy and \mathbf{q} integrated magnetic cross section should be 1.0 % of the total energy and \mathbf{q} integrated nuclear incoherent scattering cross section. Hence, the measured ratio between magnetic and NSI is $\frac{1}{10}$ of this.

A pattern of low and high NSI intensities at $T = 1.5$ K in $(h k k)$ is visible in figure 9.6a. A similar pattern was found between Bragg reflections in elastic scattering intensity from boleite measured on IN8 as seen in figure 9.4. When the temperature is increased to $T = 300$ K, the NSI pattern of low and high intensity becomes less clear as seen in figure 9.6b.

We suggest that the pattern arises from absorption by the sample holder. Sample holder 2 was used for both the experiments on IN8 and D7, and it has three aluminum pillars in the scattering plane, as seen in figure 9.1b. The aluminum pillars absorb some of the incoming and outgoing neutrons from the sample. Figure 9.6(a-b) shows an illustration of how a single pillar's absorption

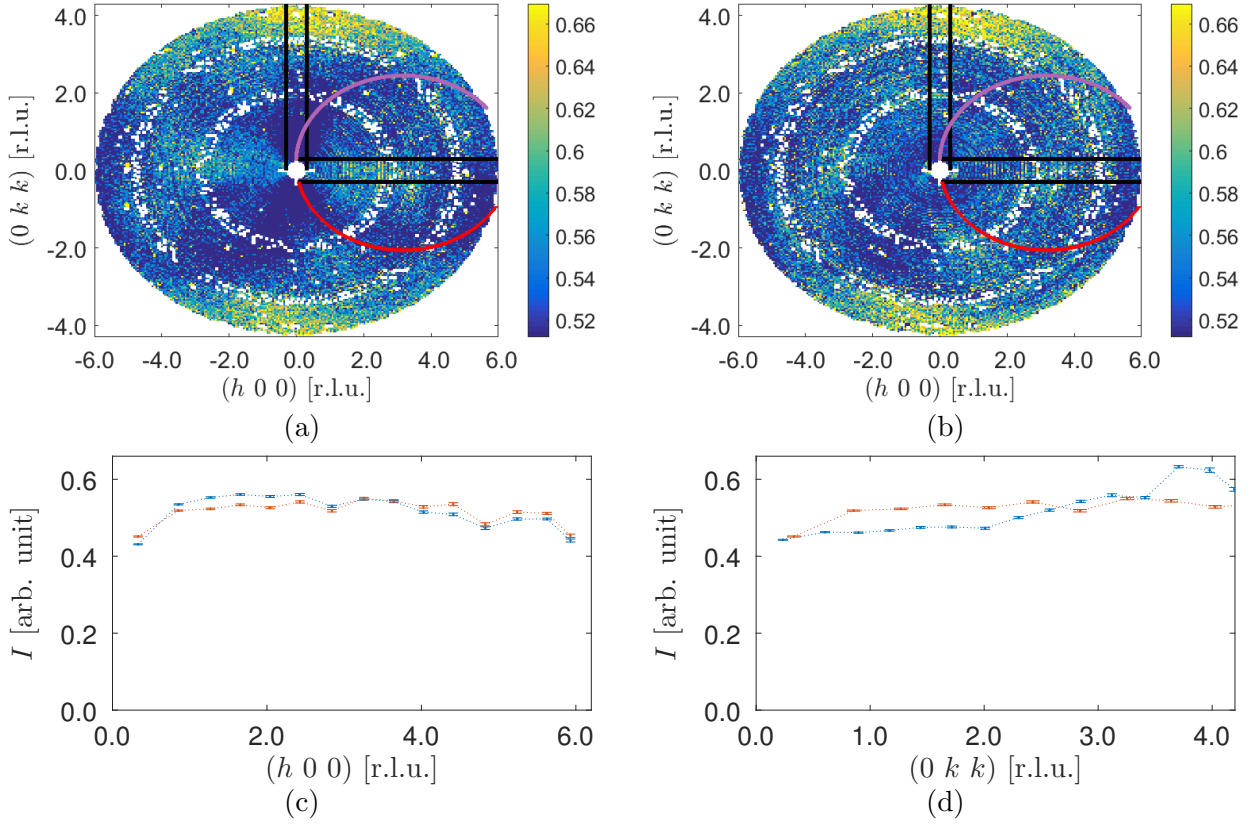


Figure 9.6: The NSI neutron scattering component separated from the total scattering from boleite by polarization analysis on D7. **(a-b)** Color plot of energy integrated NSI neutron scattering intensity at $T = 1.5$ K **(a)** and $T = 300$ K **(b)**. The color scale, shown to the right of the plots, are given in arbitrary units. The overlaid colored and curved lines represent the position in $(h \ k \ k)$ of a single sample holder pillar’s absorption of incoming (red) and outgoing (purple) neutrons from the center of the sample holder. The overlaid straight black lines show the area in q -space of the 1D plot of the NSI scattering intensity along $(h \ 0 \ 0)$, shown in **(c)**, and $(0 \ k \ k)$, shown in **(d)**. The NSI scattering intensity in **(c-d)** is binned and shown for both $T = 1.5$ K (blue) and $T = 300$ K (red).

of incoming and outgoing neutrons from the center of the sample holder would affect the detector signal. The absorption lines of a single pillar seem to follow the same kind of curving trend as the low intensity pattern in the NSI scattering component. It is difficult to model the exact absorption pattern from the pillars since multiple parameters contribute to the total absorption: As example one would have to know the exact position and shape of the 7 crystals and aluminum wires squeezed around them, the exact width of the beam, the width of the pillars, and the absorption cross section of all these things.

The NSI scattering components of the total scattering along $(h \ 0 \ 0)$ and $(0 \ k \ k)$ for low and high temperatures are shown in figure 9.6(c-d). The figures reveal that the energy integrated NSI signal can give rise to larger signal at $T = 1.5$ K than at $T = 300$ K. This is most clearly seen in the

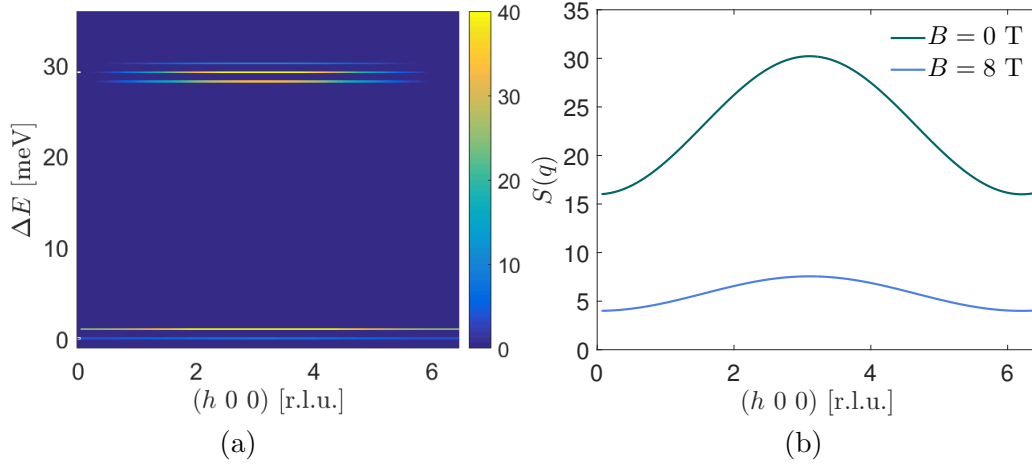


Figure 9.7: Expected $S(\mathbf{q}, \omega)$, from the 8 isolated spin triangles in the truncated boelite cube, in a field applied along the $\hat{\mathbf{z}}$ -direction, at $T = 0$ K. (a) $S(\mathbf{q}, \omega)$ at $B = 8$ T as function of $(h\ 0\ 0)$ and ΔE . (b) Elastic scattering $S(\mathbf{q})$ along $(h\ 0\ 0)$ at two different field strengths, given in the legends.

NSI component along $(0\ k\ k)$ in figure 9.6c, where the $T = 300$ K is largest for small q , and the $T = 1.5$ K is largest above $k = 3.5$ r.l.u.

It has not been possible to come up with an explanation of the temperature dependence of the NSI scattering observed in D7, as well as the temperature of the elastic signal from RITA-II. The shape of NSI scattering should be different in the elastic scattering signal measured at RITA-II, since different sample holders were used. This hypothesis was not properly tested by measuring the scattering from sample holder 2 on RITA-II.

9.4.1 Applying an external field

Figure 9.7 shows the expected $S(\mathbf{q}, \omega)$ from the 8 isolated triangles in a boelite configuration when an external field is applied at $T = 0$ K. The degenerate ground state is split into two states by the external field, and the excited quadruplet is split into 4, where only 3 states are reachable for the neutron scattering from the ground state. Magnetic scattering only happens between states where the difference in magnetization is $|\Delta m| \leq 1$ according to conservation of angular momentum. From the triangle model, it is expected that the elastic signal will decrease significantly, since the applied field breaks the degeneracy and hence moves scattering from the elastic line, and into the inelastic spectrum.

It has not been possible to calculate $S(\mathbf{q}, \omega)$ from the variational model. Instead, figure 9.8 shows how the variational model's 100 lowest eigenenergies of each of the magnetization subspaces will be affected by an external field. The result shows that for $J_2 = 3.4$ meV, a field of $B \sim 12$ T is required for the ground state to switch from the $m = 0$ subspace to the $m = 1$ subspace. It is therefore, from this model, not expected to see any difference in scattering signal when the external field is changed from $B = 0$ T to $B = 7.9$ T.

The two boelite models' validity was tested by applying an external magnetic field to the boelite

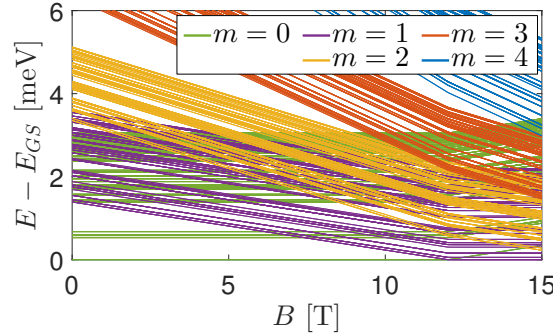


Figure 9.8: The 100 lowest eigenenergies of each of the magnetization subspaces as function of magnetic field, according to the variational model.

sample. The elastic signal was measured at $(h\ k\ k)=(3.1\ 0\ 0)$ r.l.u. at RITA-II as the external field was change from $B = 0$ T to $B = 7.9$ T. No change was found in the elastic line.

To test if possible low energy magnetic excitations were present, and affected by an external field, the inelastic spectrum was measured at different field strengths. The low energy inelastic signal was measured at $(h\ k\ k)=(3.5\ 0\ 0)$ r.l.u. between $\Delta E = 0$ meV and $\Delta E = 2.1$ meV. We expect that no phonons are present at the Brillouin zone boundary within this energy range, since the lowest energy acoustic phonon is believed to be at $\Delta E = 2.15 \pm 0.06$ meV. The phonon dispersion relation was measuring around the $(0\ 4\ 4)$ Bragg peak. The mapping of the phonon dispersion relation is shown in appendix D.

No significant difference was found in the inelastic scattering intensity between $B = 0$ T and $B = 7.9$ T, as shown in figure 9.9. A peak in intensity with center at 0.89 ± 0.03 meV is seen at both field strengths. The peak is placed slightly differently from what we would expect from the energy levels predicted by the variational model, with $J_2 = 3.4$ meV, as seen in figure 9.8. According to the variational model, the 4 lowest lying energy levels are placed between $E = 0.56$ meV and $E = 0.66$ meV. The peaks independence of field could be justified from the variational model, as seen from its predictions of the low energy states in figure 9.8. The peak is most likely not a phonon, as acoustic phonons are predicted to be located above $\Delta E > 2.15$ meV, at a Brillouin zone boundary. Unfortunately, the measurement was not repeated at $(-3.5\ 0\ 0)$ r.l.u. to see if the signal was also present here, which would be expected from the cubic structure of boleite.

The peak seen in figure 9.9 comes from a strong signal detected in 2 of the 9 analyzer blades in RITA-II detection system. This shows that the peak is localized in reciprocal space. This is not likely to be magnetic, since we expect broad shaped scattering patterns from the inelastic scattering as well as the elastic scattering.

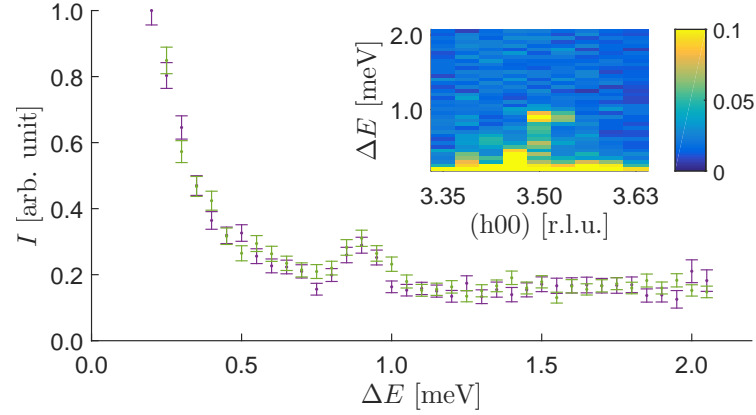


Figure 9.9: Inelastic neutron data measured at RITA-II along $(h\ 0\ 0)$ direction for $B = 0$ T (purple) and $B = 7.9$ T (green). All RITA-II's 9 analyzer blades intensity are summed. The instrument resolution tail from the elastic line is visible at $\Delta E \leq 0.5$ meV. The insert plot shows the raw scattering intensity at $B = 0$ T from the 9 analyzer blades as function of energy in a color plot. Each analyzer blade has its own position in $(h\ 0\ 0)$. Notice how the bulge shape, seen in the 1D data, only appears in analyzer blade 5 and 6.

9.5 The search for high energy excitations

With an exchange constant $J_1 = 19.4$ meV, an inelastic scattering signal should be placed around $\Delta E = 19.6 \text{ meV} \cdot \frac{3}{2} = 29.1$ meV, due to the high energy excitation, according to the 8 isolated triangles model. The inelastic scattering signal from IN4 is seen in figure 9.10. A range of bands of high intensity scattering can be seen in the figure. Around 29.1 meV, there are two high intensity bands, one at ~ 27 meV and one at ~ 33 meV. The intensity of the bands are increasing with q . Magnetic scattering would decrease with q , due to the magnetic form factor, whereas phonons scattering intensity increase as q^2 . It is therefore likely that the observed high intensity scattering bands are phonons. Unfortunately, the phonons are dispersed along the entire expected energy range of the high energy magnetic excitations. As the temperature is increased to $T = 250$ K, it is clear from figure 9.10 that the phonon scattering intensity is broadened in energy. This means that a simple subtraction of high and low temperature shows an uneven signal, which effectively prohibited us from identifying any magnetic excitations in the high energy region.

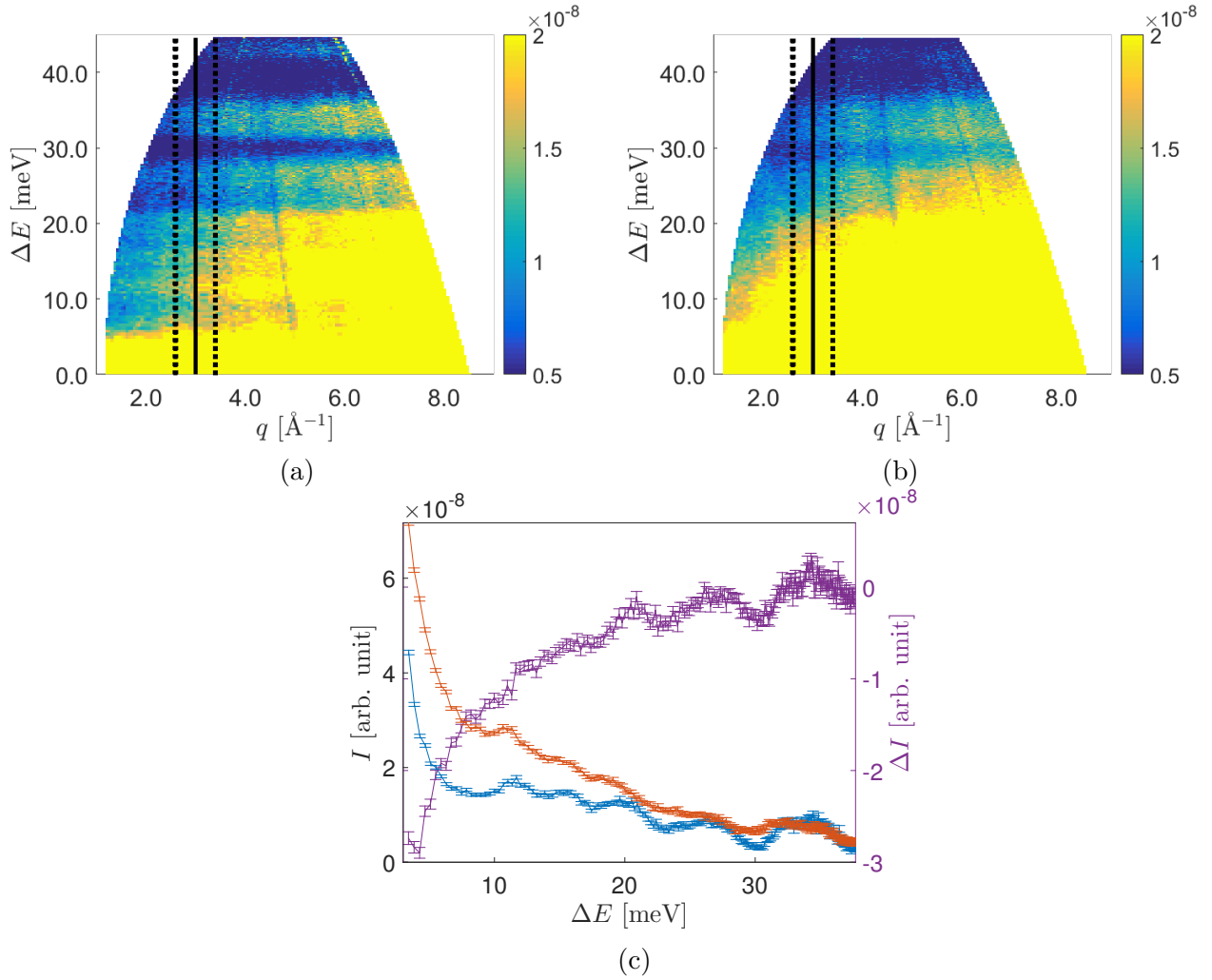


Figure 9.10: Inelastic neutron scattering from boleite measured at IN4. The sample was rotated 360 degree while measuring. Color plot of inelastic scattering from boleite at $T = 1.5$ K (a) and $T = 250$ K (b). The color scales shown to the right of the plots are in arbitrary units. Black lines mark 1D cut through. (c) 1D cut of IN4 data at $Q = 3 \pm 0.4$ \AA for $T = 1.5$ K (blue) and $T = 250$ K (red). The difference $\Delta I = I_{T=1.5\text{ K}} - I_{T=250\text{ K}}$ is shown on right axis (purple).

CHAPTER 10

Discussion

In chapter 6 and 7, it was shown that the magnetic susceptibility measured on boleite could be explained by an isolated magnetic unit cell formed as a truncated cube of 8 coupled copper ion triangles. The system was found to have two different exchange coupling strengths: $J_1 = 19.4 \pm 0.4$ meV, between the copper ions in the triangles, and $J_2 = 3.4 \pm 0.1$ meV, between the copper ions on neighboring triangles. The large difference between the exchange constants leads to the interpretation that boleite at $k_B T \gg J_1$ behaves as a collection of paramagnetic spins. When the temperature is decreased to $J_2 < k_B T < J_1$, the spins are bound in isolated triangle ground states. At $k_B T \ll J_2$, the 24 spin system orders into a unique singlet ground state.

However, a lot of questions are left unanswered. In this chapter, I will discuss the offset of the susceptibility data, the two different boleite types, the paramagnetic spins, and the missing neutron scattering results. In the end of the chapter, I will define the concept of a quantum spin droplet, and discuss how it relates to boleite.

10.1 The offset in the susceptibility data

The susceptibility measurements on the boleite crystals showed an inconsistent offset, as seen in figure 6.3. To quantify the offset, I define

$$\chi_{max} = \langle \chi(T > 285\text{K}) \rangle, \quad (10.1)$$

where $\langle \chi(T > 285\text{K}) \rangle$ is the mean of the susceptibility at $285\text{ K} < T < 300\text{ K}$. Additionally, a Curie Weiss line is fitted to the inverse susceptibility at $180\text{ K} < T < 300\text{ K}$, for all crystals, and the Curie Weiss temperature Θ_{CW} is found for each Curie Weiss line. In figure 10.1 $1/\chi_{max}$ and $-1/\Theta_{CW}$ are shown as function of the crystal mass.

Figure 10.1 shows that there is a clear correlation between $1/\chi_{max}$ and the mass. A similar, although not as clear, correlation is seen between $-1/\Theta_{CW}$ and the mass. The susceptibility is mass normalized, and $1/\chi_{max}$ should therefore be constant as function of mass. $-1/\Theta_{CW}$ should not depend on the mass normalization and should be the same for all measurements.

The different instruments allowed for different size of samples, and hence the mass is correlated with the instrument used. It has not been possible to examine how much the instrument affects the measurement. It is however clear that the small mass samples measured at the EPFL MSPM and AU PPMS have significant smaller $1/\chi_{max}$ than the samples measured at PSI PPMS and MPMS. The small mass samples are typically powder or small pieces obtained from the surface of the crystals. Assuming that the offset is an effect originating from the crystal, and not an instrument artifact, a possible explanation could be that small pieces of different crystal forms are found on the surface of the crystal. A general malfunction of the MPMS at EPFL and the PPMS at AU could also be the reason. We know from the AU instrument-responsible that it was indeed the case for some AU measurements (E2, C2, and C3). It could also be a systematic problem with the PPMS and MPMS instruments when used on small mass boleite sample that causes the offset. To examine the mass correlation further, measurements of a large boleite crystals should be done together with powder and small pieces from the same crystal at the MPMS at PSI.

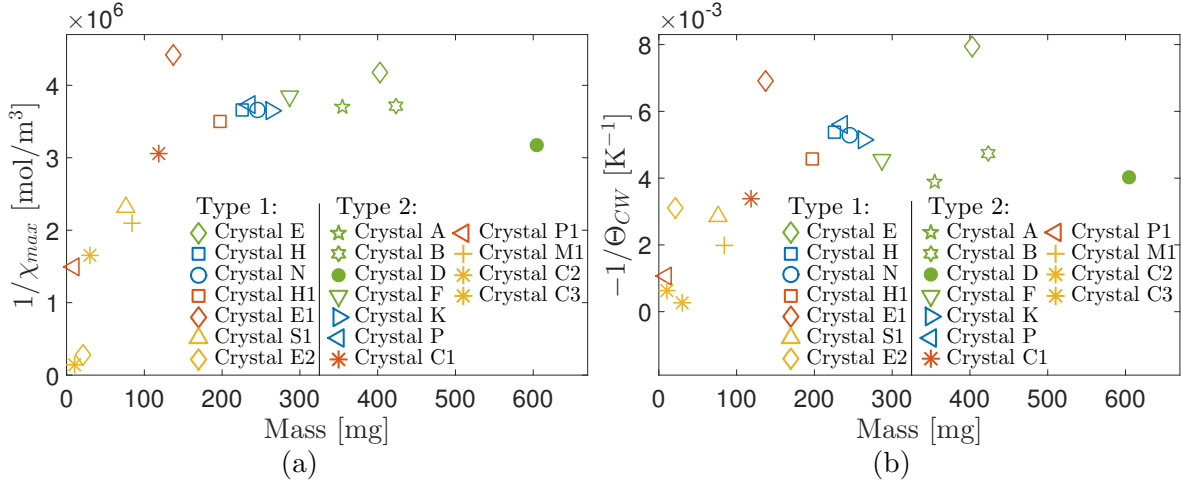


Figure 10.1: Mass dependence of the susceptibility. (a) Mean inverse susceptibility at $285 \text{ K} < T < 300 \text{ K}$, χ_{max}^{-1} , defined in equation 10.1, as function of mass. (b) The negative inverse Curie Weiss temperature $-\Theta_{CW}^{-1}$ of a Curie Weiss line fitted to the inverse susceptibility at $180 \text{ K} < T < 300 \text{ K}$, as function of mass.

10.2 The two boleite types and the paramagnetic spins

In chapter 6, two types of boleite crystals were defined. The definition of crystal types separates the crystals by a kink in the susceptibility around $T \sim 5 \text{ K}$. In this section, I will look into the behavior of the two crystal types and the paramagnetic contribution as seen from the bulk measurements.

We saw in chapter 7 that the missing kink could be explained by a suppression from a paramagnetic behavior. When this behavior was subtracted from the susceptibility, the type 1 crystals' susceptibility became more alike the type 2 crystals' susceptibility. For some of the crystals, the two types could be fitted with the CVT model, and both types show a similar result, as seen in figure 7.10 and 7.11.

We believe that the difference in type 1 and 2 crystals are due to a different amount of impurity (or defect) paramagnetic spins, since a difference in average amount of impurity spins is found in equation (7.27). The amount of impurity spins needed to suppress the transition into the ground state of a system of 24 spins is not determined accurately. A lower bound of the required amount of defect spins can be approximated to be given by the average result of fitting a paramagnetic spin model together with the triangle model to the susceptibility of type 1 crystals. The estimate is that if the amount of defects is above $9 \pm 2 \%$, the low temperature transition in the bulk measurements is suppressed by the paramagnetic contribution.

It is, however, a quite naive estimate, as we can see an overlap between the number of impurity spins in type 1 and type 2 crystals in table 7.2. As an example, the type 1 crystal N is found to have 5.4 % impurity spins, and the type 2 crystal K is found to have 6.2 %. The result indicates that a sharp transition between the two types of crystal as function of number of impurities might not exist, or/and that the estimate of the number of impurity spins are quite uncertain.

The type 1 crystal H1 was measured with an AC-susceptometer at dilution fridge temperatures at EPFL, as seen in figure 8.4 and 8.5. The low temperature ($T < 1 \text{ K}$) susceptibility shows a clear Curie tail, which is a direct indication of a paramagnetic behavior. The dilution fridge data and

the fitting of a combined paramagnetic and spin triangle model thereby both indicate the existence of spins that behave paramagnetically. The estimated amount of paramagnetic spins varies greatly between the measurements of H. From the fitting of a combined paramagnetic and triangle model to crystal H raw data, the amount of paramagnetic spins is estimated to 6.5 % for crystal H and 1.5 % for crystal H1. From the analysis of dilution fridge data of crystal H1, it was estimated that there was 12.3 ± 0.4 % paramagnetic spins. The difference in the crystal H results show that the estimate of the amount of paramagnetic spins is quite rough, since different crystals and techniques result in different results. Crystal H is, however, a special case as it was the only crystal where the CVT model could not be fitted after the subtraction of paramagnetic spins in chapter 7, and we should therefore be skeptical about all results measured on crystal H.

It would have been a major improvement on the estimate of the amount of paramagnetic spins in the boleite crystals, if more susceptibility measurements at dilution fridge temperatures could be performed. Especially, it would have been interesting to see if a Curie tail was present in the type 2 crystals' susceptibility at low temperature, which we would expect if paramagnetic spins were present. More susceptibility measurements at dilution fridge temperatures might also reveal possible inter cube ordering, which should reveal a third kink in the susceptibility and only occur at very low temperatures.

Our hypothesis, that the type 1 and 2 crystals' different behaviors are due to a difference in the amount of impurity spins, is strengthened by the measurements of magnetization as function of magnetic field. In figure 8.2 and 8.3, it is clearly seen that the type 2 crystal behaves more like the variational model, and the type 1 crystal like the triangle model. This indicates that the type 2 crystals undergo ordering into the low energy states of the full 24 spin system, whereas this ordering is suppressed in the type 1 crystals' magnetization curve.

The heat capacity of the boleite type 2 sample M1 could not be modeled fully but revealed a magnetic contribution. According to the variational model and the triangle model, the observed magnetic signal at low temperatures, seen as an upturn in heat capacity divided by temperature in figure 8.1, is due to the coupling of the 8 triangles. From the understanding gained from the susceptibility, and the magnetization as function of field, we would expect that a type 1 crystal would not show this upturn. It has however not been possible to measure a type 1 crystal. A problem with the heat capacity measurements is the uncertainty at the size of the lattice contribution. A method to separate the magnetic and lattice contribution could be to measure the heat capacity at different field strengths, since only the magnetic contribution should be affected.

It has not been established where the hypothesized paramagnetic contribution comes from. It is likely that random impurities in the boleite unit cell occur. As an example the magnetic Cu^{2+} ions could randomly be replaced with the non magnetic Zn^{2+} , creating imperfect cubes. It could also be possible that the paramagnetic impurities originate from small pieces of other crystal structures growing together with the boleite crystals. X-ray and neutron diffraction experiments might be able to resolve if other crystal structures are growing in between boleite crystals, and chemical composition analysis might resolve if Zn^{2+} ions are present in the crystals.

10.3 The neutron result

No magnetic structures could be identified in the neutron scattering data, where phonon and incoherent scattering created a too large background for the expected short range order magnetic scattering to be seen, as shown in chapter 9.

From the polarization analysis, we found that the total magnetic cross section is 0.10 ± 0.05 % of

the total nuclear spin incoherent cross section for $T = 1.5$ K. This does not correspond with the theoretical estimate of around 1 %. The theoretical estimate could be slightly wrong as it relies on a range of assumptions, like $F_m(q) = 1$. The average magnetic form factor $\langle F_m(q) \rangle$ is within any given q -range smaller than 1, since the magnetic form factor decreases from 1 to 0 as q is increased. The approximation $F_m(q) = 1$ therefore results in an overestimation of the total magnetic scattering cross section. At the same time, XYZ-polarization analysis is a complex method with 6 different polarization measurements per measuring point, as well as normalization measurements of cadmium, vanadium, and an empty aluminum container. In any of these measurements small assumptions are made, and it could affect the observed size of a very weak magnetic signal. It is therefore reasonable to have certain doubts of the estimated ratio of spin incoherent and magnetic scattering from the D7 measurements, as systematic uncertainties could affect the ratio. It is in any case clear that the magnetic scattering is extremely small compared to the incoherent background, and that no magnetic structures were observed in the magnetic component seen in figure 9.5.

Combining the results from all neutron experiment, it is evident that it has not been possible to detect magnetic structures in the neutron data, and that it is difficult, if not impossible, to detect magnetism in natural boleite using neutrons.

A way to optimize the chances of seeing the short range order magnetic scattering would be to minimize the incoherent background. This could be achieved if the boleite crystals were deuterated (i.e. replacing hydrogen ^1H with deuterium ^2H). Deuterium has an incoherent scattering cross section of $2.05 \cdot 10^{-24} \text{ cm}^2$ compared to $80.02 \cdot 10^{-24} \text{ cm}^2$ of hydrogen [35]. There is however still 62 chlorine atoms in the sample with a incoherent scattering cross section of $5.3 \cdot 10^{-24} \text{ cm}^2$, and the total incoherent scattering would even for a deuterated sample be $446.2 \cdot 10^{-24} \text{ cm}^2$. This means that the magnetic scattering cross section would be 9.8 % of the incoherent background, according to our theoretical estimate of the magnetic contribution. In other words, the magnetic scattering cross section would be 10 times larger, if the boleite crystals were deuterated compared to non-deuterated. If the theoretical estimate is wrong, and the ratio of magnetic scattering from the non-deuterated sample is of the order of 0.10 ± 0.05 %, as the D7 data suggests, the magnetic signal of a deuterated sample would only be around 1 % of the background. It is not within the authors knowledge possible to assess if the sample could be deuterated, but given the above discussion, it is not even certain that it would be worth the try.

10.4 Boleite - A quantum spin droplet

All the experimental results indicate that the boleite system behaves as a 24 spin system, and that the magnetic spins in different magnetic unit cells do not feel the presence of each other. This effectively prohibits long range interaction, the frustration parameter f (equation (3.3)) is in principle infinite, if the long range order temperature is defined to $T_O = 0$ K. The lack of long range interaction paths, however, also excludes that boleite is a true Quantum Spin Liquid, since a QSL needs long range quantum fluctuations.

In chapter 3, three different types of spin liquid behaviors were defined. Since the variational model describes the low temperature bulk data most accurately it is our best model of the low energy states of the system, and its results are usable in this discussion. In figure 7.5, it was shown that the variational model has a unique singlet ground state with an energy gap to a small continuum of the first excited singlet states $\Delta E \sim 0.66 \text{ meV}$. Above $\Delta E > 1.1 \text{ meV}$, there is a continuum of excited singlet, triplet, and higher spin states. This can also be seen in figure 9.8, which shows the field dependence of the 100 lowest energy states of all magnetization subspaces with $m \geq 0$.

The behavior of boleite seems very close to the definition of a type 1 gapped spin liquid. At $T = 0$ K, the cube will freeze into its ground state, but at temperature of just a few degrees, the 24 spin system will be able to be in multiple states.

The above discussion shows that the boleite system has a spin liquid like behavior, according to the quantum mechanical Heisenberg spin model, but it can not be a true spin liquid since the magnetic system only consist of 24 spins. We therefore invent the new term a *quantum spin droplet* to describe the boleite system. A quantum spin droplet is in this way defined as a quantum spin system that shows a spin liquid like behavior, but consists of too few interacting spins to be a real spin liquid.

CHAPTER 11

Conclusion

In this thesis, the magnetic structure of the natural mineral boleite was examined with the bulk measurement techniques: DC and AC-susceptibility, magnetization as function of field, and heat capacity. The data from these experiments have with varying success been shown to be describable with a combined Heisenberg spin model consisting of a low temperature model of the 24 magnetic spins, and a model of a triangle of spins. An estimated small contribution from paramagnetic spins was necessary to subtract from the raw data for the model to fit the magnetic susceptibility data. The model of the experimental data, in particular the magnetic susceptibility, shows that the magnetism in boleite is controlled by two different competing exchange interaction in between the 24 copper ions in the magnetic unit cell: $J_1 = 19.4 \pm 0.4$ meV between the copper ions in a triangle and $J_2 = 3.4 \pm 0.1$ meV between the copper ions on different triangles. The two competing exchange interactions result in two transition temperatures. At the high transition temperature, the triangles freeze into their ground states. At the second transition temperature, all the 24 spins in the copper cube begin to interact, and the system falls into a unique singlet ground state.

When the amount of paramagnetic impurities in the crystal becomes to large, we observe a suppression of the interaction between all 24 spins in bulk experiments. The system instead behaves as if it was 8 isolated triangles. We estimate that if the amount of defects magnetic spins is above 9 ± 2 % of the antiferromagnetic spins, the low temperature transition is suppressed.

The magnetism in boleite has not been measurable with neutrons, due to a large incoherent scattering background primarily originating from hydrogen in the crystal. It has therefore not been possible using this technique to get experimental evidence of how the magnetic structure is in boleite.

The model of the 24 spins in boleite revealed a gapped spin liquid like behavior. Due to the lack of long range interaction paths between the magnetic spin cubes in boleite, boleite can not be a true quantum spin liquid. Instead, the boleite system is in this thesis defined as a new type of quantum system, a (gapped) quantum spin droplet.

11.1 Outlook

The quantum spin droplet, boleite, is an interesting system which is a middle ground between small frustrated systems, like a single, equilateral triangle, and the frustrated lattice with quantum spin liquid behavior.

The nature of quantum spin droplets have only properly been examined with bulk measurement techniques. The thesis shows that neutron experiments are very difficult to use on boleite, and it is believed that even a deuterated boleite crystal still have significantly larger incoherent background than magnetic signal. It is therefore worth to consider if other techniques, like muon spin rotation spectroscopy or NMR could be used to measure the magnetic structure in boleite.

A lot of possible further bulk experiments could be performed. The boleite crystals magnetic susceptibility showed to have an offset correlated with the mass of the sample. This phenomena

would be interesting to examine further with tests of different pieces of the same crystal on the same susceptometer. Likewise, experimental data of the boleite crystals susceptibility below 1.5 K is greatly needed to insure that the models are correct, and to evaluate the amount of paramagnetic spins in a different way. It could also be used to establish if long range order occurs in boleite at very low temperatures.

The amount of paramagnetic spins is an interesting topic. As this thesis shows, there is a transition when the amount of paramagnetic spins becomes too large, where the interaction between all 24 spins are suppressed. It could be interesting to see if the transition could be determined accurately from more bulk measurements. X-ray and neutron diffraction measurement could be used to try to determine if the origin of these paramagnetic spins is due to random impurities or small quantities of other crystal structures growing together with boleite.

Bibliography

- [1] Dakotamatrix.com, *Picture of boleite*, accessed 29-03-2016, <http://www.dakotamatrix.com/mineralpedia/4810/boleite>
- [2] Stephen Blundell, *Magnetism in Condensed Matter*, Oxford University Press, Oxford, Great Britain, 1st edition, 2001.
- [3] J. T. Haraldsen, T. Barnes, and J. L. Musfeldt, *Neutron scattering and magnetic observables for $S=1/2$ spin clusters and molecular magnets*, Phys. Rev. B 71, 064403 (2005).
- [4] Leon Balents, *Spin liquids in frustrated magnets*, Nature 464, 199-208 (2010).
- [5] Mark A. Cooper and Frank C. Hawthorne, *Boleite: Resolution of the formula, $KPb_{26}Ag_9Cu_{24}Cl_{62}(OH)_{48}$* , The Canadian Mineralogist Vol. 38, pp. 801-808 (2000).
- [6] Kenneth Lønbæk, *Magnetic properties of the natural mineral Boleite*, B.Sc. thesis, University of Copenhagen 2014.
- [7] S. L. Holm, E. D. Christensen et. al. *Physics in spin-liquid droplets: 24-spin clusters in the mineral Boleite*, Manuscript in preparation (2016).
- [8] David J. Griffiths, *Introduction to Electrodynamics*, Prentice Hall, New Jersey, United States of America, 3rd edition, 1999.
- [9] Niels Bohr, *Studier over Metallernes Elektrontheori*, University of Copenhagen, Denmark, 1911
- [10] H.-J. Van Leeuwen. *Problèmes de la théorie électronique du magnétisme*, Journal de Physique et le Radium, 2(12):361-377, 1921.
- [11] David J. Griffiths, *Introduction to Quantum Mechanics*, Prentice Hall, New Jersey, United States of America, 2nd edition, 2005.
- [12] Nobelprize homepage, *list of laureates*, accessed 27-10-2015, http://www.nobelprize.org/nobel_prizes/physics/laureates/.
- [13] Kei Yosida. *Theory of Magnetism*. Springer, Germany, 1st edition, 1996.
- [14] Charles Kittel, *Introduction to solid state physics*, John Wiley and Sons, Inc, United States of America, 8th edition, 2005
- [15] P. W. Anderson, *The Resonating Valence Bond State in La_2CuO_4 and Superconductivity*, Science 235, 1196-1198 (1987).
- [16] B. Normand, *Frontier in frustrated magnetism*, Contemporary physics 50, No. 4, 533-552 (2009).
- [17] Stefan Wessel *Monte Carlo Simulations of Quantum Spin Models*, lecture notes from Autumn School on Correlated Electrons Emergent Phenomena in Correlated Matter 2013, Institute for Theoretical Solid State Physics, RWTH Aachen University.
- [18] Jane K. Cullum and Ralph A. Willoughby, *Lanczos Algorithms for Large Symmetric Eigenvalue Computations*, Birkhäuser-Boston INC, Secaucus, United States of America, 1985.
- [19] K. Lefmann and C. Rischel, *Dynamical Correlation function of the Nearest Neighbor and Haldane-Shastry Heisenberg Antiferromagnetic $s=1/2$ chains in zero and applied fields*, Phys. Rev. B 54, 6340-50 (1996).

- [20] Camilla Buhl Larsen, *Exact diagonalization studies of two-dimensional quantum spin systems*, M.Sc. thesis, University of Copenhagen 2015.
- [21] MATLAB and Statistics Toolbox Release 2015a, The MathWorks, Inc., Natick, Massachusetts, United States.
- [22] Andreas Honecker and Josef Schüle, *OpenMP Implementation of the Householder Reduction for Large Complex Hermitian Eigenvalue Problems*, Parallel Computing: Architectures, Algorithms, and Applications, Vol. 38, pp. 271-278 (2007).
- [23] Daniel C. Mattis and Robert H. Swendsen, *Statistical mechanics made simple*, World Scientific Publishing, United States of America 2nd edition, 2008
- [24] Henrik Bruus and Karsten Flensberg, *Many-Body Quantum Theory in Condensed Matter Physics*, Oxford University Press, Oxford, Great Britain, 1st edition, 2004.
- [25] Quantum Design, *Manual for PPMS*, accessed 02-01-2016, <http://www.qdusa.com/sitedocs/productBrochures/mag3-07.pdf>.
- [26] Quantum Design, *Manual for MPMS*, accessed 02-01-2016, http://physique.umontreal.ca/~andrea_bianchi/uploads/Site/SQUID_VSM_User_Manual.pdf.
- [27] Quantum Design, *Introduction to AC Susceptibility*, accessed 03-02-2016, <http://www.qdusa.com/sitedocs/appNotes/ppms/1078-201.pdf>.
- [28] R. C. Jaklevic, J. Lambe, A. H. Silver, and J. E. Mercereau, *Quantum Interference Effects in Josephson Tunnelling*, Phys. Rev. Letters 12 (7): 159160, (1963).
- [29] Quantum Design, *Manual for PPMS heat capacity measurement*, accessed 02-01-2016, <https://www.qdusa.com/sitedocs/productBrochures/heatcapacity-he3.pdf>.
- [30] Laurence Passell *Neutron Spectroscopy: How it all began*, article for Los Alamos workshop, Brookhaven National Laboratory, USA, 1980.
- [31] A. Garcia, J.L. Garcia-Luna, and G.L. Castro, *Neutron beta decay and the current determination of V_{ud}* Phys. Lett. B, 500:66, 2001.
- [32] Gordon L. Squires, *Thermal Neutron Scattering*, Cambridge University Press, United States of America, 3rd edition, 2012.
- [33] Kim Lefmann, *Neutron Scattering: Theory, Instrumentation, and Simulation*, Course notes, Niels Bohr Institute, University of Copenhagen, 2013.
- [34] John R.D. Copley, NCNR Summer School on Methods and Applications of Neutron Spectroscopy, June 25-29, 2007, *Introduction to neutron scattering*, accessed 01-11-2015, https://www.ncnr.nist.gov/summerschool/ss07/SS07Intro_talk.pdf.
- [35] NIST homepage, *Table of elements*, accessed 09-01-2016, <https://www.ncnr.nist.gov/resources/n-lengths/list.html>.
- [36] Kim Lefmann and Christian Rischel, *Dynamical correlation function of $S=1/2$ nearest-neighbor and Halden-Shastry Heisenberg antiferromagnetic chains in zero and applied fields.*, Physical Review B 54, Number 9 (1996).

- [37] J. Lorenzana, G. Seibold, and R. Coldea, *Sum rules and missing spectral weight in magnetic neutron scattering in the cuprates*, Physical Review B 72, 224511 (2005).
- [38] G. Ehlers, J. R. Stewart, et al, *Generalization of the classical xyz-polarization analysis technique to out-of-plane and inelastic scattering*, Rev. Sci. Instrum. 84, 093901 (2013).
- [39] PSI homepage, *RITA-II instrument description*, accessed 13-12-2015 <https://www.psi.ch/sinq/ritaii/description>.
- [40] ILL-homepage, *Flatcone layout*, accessed 03-03-2016, <https://www.ill.eu/instruments-support/instruments-groups/instruments/flatcone/description/instrument-layout/>.
- [41] Hannu Mutka, *Coupled time and space focusing for time-of-flight inelastic scattering*, Nuclear Instruments and Methods in Physics Research A 338, 144 150 (1994).
- [42] ILL-homepage, *IN4C instrument layout*, accessed 13-12-2015, <https://www.ill.eu/instruments-support/instruments-groups/instruments/in4c/description/instrument-layout/>.
- [43] ILL-homepage, *D7 instrument layout*, accessed 13-12-2015, <https://www.ill.eu/instruments-support/instruments-groups/instruments/d7/description/instrument-layout/>.
- [44] T. Chupp, Summer School on the Fundamentals of Neutron Scattering, June 22-26, 2009, *Neutron Optics and Polarization*, accessed 11-01-2016, https://www.ncnr.nist.gov/summerschool/ss09/pdf/Chupp_FP09.pdf.
- [45] O. Schaerpf, *Properties of beam bender type neutron polarizers using supermirrors*, Physica B156&157 (1989). 639
- [46] F. Mezei, *Neutron Spin Echo: A New Concept in Polarized Thermal Neutron Techniques*, Z. Physik 255, 146-160 (1972)
- [47] John W. Anthony, Richard A. Bideaux, Kenneth W. Bladh, and Monte C. Nichols, Eds., *Handbook of Mineralogy*, Mineralogical Society of America, Chantilly, USA, accessed 09-02-2016, <http://www.handbookofmineralogy.org/>.
- [48] M. Momma and F. Izumi, *Vesta 3 for three-dimensional visualization of crystal, volumetric and morphology data*, Journal of Applied Crystallography, 2011.
- [49] Pseudoboleite, webmineral.com, accessed 09-02-2016, <http://webmineral.com/data/Pseudoboleite.shtml#.VrneTPnhDIV>
- [50] Qlaue - Simulation of back reflection Laue diffraction. Download from <https://sourceforge.net/projects/qlaue/>.
- [51] Paolo Giannozzi Lecture notes: Numerical Methods in Quantum Mechanics, University of Udine, Italy, accessed 10-02-2016 <http://www.fisica.uniud.it/~giannozz/Corsi/MQ/LectureNotes/mq.pdf>
- [52] T. Fennel, J. O. Piatek, et. al. *Spangolite: An $s = 1/2$ maple leaf lattice antiferromagnet?*, J. Phys.: Condens. Matter 23, 164201 (2011).

Appendices

APPENDIX A

Complete solution to the 6 spin system

The complete diagonalization result of the 6 spin system is shown in this appendix. The result was calculated by Kenneth Lønbæk and originally presented in [6]. Below, all $2^6 = 64$ states of the 6 spin system are shown categorized by their magnetization:

$$E_{(m=3)} = E_{(m=-3)} = \left\{ \begin{array}{ll} \frac{3}{2}J_1 + \frac{1}{4}J_2 & 1 \text{ State} \end{array} \right\} 2 \times 1 \text{ States} \quad (\text{A.1})$$

$$E_{(m=2)} = E_{(m=-2)} \underset{\approx}{\mathcal{O}\left(\frac{J_2^2}{J_1^2}\right)} \left\{ \begin{array}{ll} \frac{3}{2}J_1 + \frac{1}{4}J_2 & 1 \text{ State} \\ \frac{3}{2}J_1 - \frac{1}{12}J_2 & 1 \text{ State}^* \\ \frac{1}{4}J_4 & 3 \text{ States} \\ -\frac{5}{12}J_2 & 1 \text{ State}^* \end{array} \right\} 2 \times 6 \text{ States} \quad (\text{A.2})$$

$$E_{(m=1)} = E_{(m=-1)} \underset{\approx}{\mathcal{O}\left(\frac{J_2^2}{J_1^2}\right)} \left\{ \begin{array}{ll} \frac{3}{2}J_1 + \frac{1}{4}J_2 & 1 \text{ State} \\ \frac{3}{2}J_1 - \frac{1}{12}J_2 & 1 \text{ State}^* \\ \frac{3}{2}J_1 - \frac{11}{36}J_2 & 1 \text{ State}^* \\ \frac{1}{4}J_2 & 4 \text{ States} \\ \frac{1}{36}J_2 & 1 \text{ State}^* \\ -\frac{5}{12}J_2 & 3 \text{ States}^* \\ -\frac{3}{2}J_1 + \frac{1}{4}J_2 & 1 \text{ State} \\ -\frac{3}{2}J_1 + \frac{1}{36}J_2 & 1 \text{ State}^* \\ -\frac{3}{2}J_1 - \frac{1}{12}J_2 & 2 \text{ States}^* \end{array} \right\} 2 \times 15 \text{ States} \quad (\text{A.3})$$

$$E_{(m=0)} \underset{\approx}{\mathcal{O}\left(\frac{J_2^2}{J_1^2}\right)} \left\{ \begin{array}{ll} \frac{3}{2}J_1 + \frac{1}{4}J_2 & 1 \text{ State} \\ \frac{3}{2}J_1 - \frac{1}{12}J_2 & 1 \text{ State}^* \\ \frac{3}{2}J_1 - \frac{11}{36}J_2 & 1 \text{ State}^* \\ \frac{3}{2}J_1 - \frac{5}{12}J_2 & 1 \text{ State}^* \\ \frac{1}{4}J_2 & 4 \text{ States} \\ \frac{1}{36}J_2 & 1 \text{ State}^* \\ -\frac{5}{12}J_2 & 3 \text{ States}^* \\ -\frac{3}{2}J_1 + \frac{1}{4}J_2 & 3 \text{ State} \\ -\frac{3}{2}J_1 + \frac{1}{36}J_2 & 1 \text{ State}^* \\ -\frac{3}{2}J_1 - \frac{1}{12}J_2 & 3 \text{ States}^* \\ -\frac{3}{2}J_1 - \frac{3}{4}J_2 & 1 \text{ States} \end{array} \right\} 1 \times 20 \text{ States} \quad (\text{A.4})$$

All states marked with a * are first order approximations assuming $J_2/J_1 \ll 1$.

APPENDIX B

Calculating the $m = 0$ subspace

In this appendix, I will show an example of what happens when the Hamiltonian $\hat{\mathcal{H}}_6$ from equation (7.5) is applied to a $m = 0$ basis state of the 6 spin system shown in figure 7.4. I will calculate what happens when the Hamiltonian $\hat{\mathcal{H}}_6$ is applied to $\left(\nabla \otimes \triangle\right)$. In the case of the $m = 0$ subspace, the raising and lowering operators ($\hat{S}_3^+ \hat{S}_4^-$) will couple this basis state with the basis states of opposite rotation, eg. $\left(\nabla \otimes \triangle\right)$. This happens because the isolated triangle Ising states $|1, \downarrow\rangle|5, \uparrow\rangle$, $|2, \downarrow\rangle|5, \uparrow\rangle$, $|1, \downarrow\rangle|6, \uparrow\rangle$, and $|2, \downarrow\rangle|6, \uparrow\rangle$ are flipped into other non excited states. The $|3, \downarrow\rangle|4, \uparrow\rangle$ state is also affected by $\hat{S}_3^+ \hat{S}_4^-$, but it is flipped into an excited spin $m = 3/2$ state, and it is therefore removed. All other isolated triangle Ising states, have spin 3 and 4 pointing in the same direction, and are therefore not affected by $\hat{S}_3^+ \hat{S}_4^-$. The full result when applying the Hamiltonian is

$$\begin{aligned}
 \hat{\mathcal{H}}_6 \left(\nabla \otimes \triangle \right) &= \frac{1}{3} \hat{\mathbf{S}}_3 \cdot \hat{\mathbf{S}}_4 (|1, \downarrow\rangle + e^+ |2, \downarrow\rangle + e^- |3, \downarrow\rangle) \otimes (|4, \uparrow\rangle + e^+ |5, \uparrow\rangle + e^- |6, \uparrow\rangle) \\
 &= \frac{J_2}{12} (|1, \downarrow\rangle|4, \uparrow\rangle - e^+ |1, \downarrow\rangle|5, \uparrow\rangle - e^- |1, \downarrow\rangle|6, \uparrow\rangle \\
 &\quad + e^+ |2, \downarrow\rangle|4, \uparrow\rangle - e^- |2, \downarrow\rangle|5, \uparrow\rangle - |2, \downarrow\rangle|6, \uparrow\rangle \\
 &\quad - e^- |3, \downarrow\rangle|4, \uparrow\rangle + |3, \downarrow\rangle|5, \uparrow\rangle + e^+ |3, \downarrow\rangle|6, \uparrow\rangle) \\
 &\quad + \frac{J_2}{6} (|1, \uparrow\rangle|5, \downarrow\rangle + e^- |1, \uparrow\rangle|6, \downarrow\rangle + |2, \uparrow\rangle|5, \downarrow\rangle \\
 &\quad + e^+ |2, \uparrow\rangle|6, \downarrow\rangle) \\
 &= \frac{J_2}{12} (-|1, \downarrow\rangle - e^+ |2, \downarrow\rangle + e^- |3, \downarrow\rangle) \otimes (-|4, \uparrow\rangle + e^+ |5, \uparrow\rangle + e^- |6, \uparrow\rangle) \\
 &\quad + \frac{J_2}{6} (|1, \uparrow\rangle + e^- |2, \uparrow\rangle) \otimes (|5, \downarrow\rangle + e^+ e^- |6, \downarrow\rangle) \\
 &= \frac{J_2}{36} \left(-\nabla + 2e^+ \nabla - 2e^- \nabla \right) \otimes \left(\triangle - 2\triangle - 2\triangle \right) \\
 &\quad + \frac{J_2}{18} \left(2\nabla - e^- \nabla - e^+ \nabla \right) \otimes \left(-e^+ \triangle + 2e^+ \triangle - e^+ \triangle \right).
 \end{aligned} \tag{B.1}$$

Again the excited states like \triangle_{\downarrow} are removed and

$$\begin{aligned} \hat{\mathcal{H}}_6 \left(\nabla \otimes \triangle \right) = \frac{J_2}{36} \big(& - \nabla \otimes \triangle + 2 \nabla \otimes \triangle + 2e^+ \nabla \otimes \triangle - 4e^+ \nabla \otimes \triangle \\ & - 4e^+ \nabla \otimes \triangle + 8e^+ \nabla \otimes \triangle + 2 \nabla \otimes \triangle - 4 \nabla \otimes \triangle \big). \end{aligned} \quad (\text{B.2})$$

Similar results are found for all other states, and the combined result is that the Hamiltonian is given in equation (7.14).

APPENDIX C

Subtracting the paramagnetic contribution.

This appendix illustrates how the paramagnetic contribution was found and subtracted from the raw data for each sample. The fitting of the paramagnetically adjusted data with the CVT model is also included for the type 2 boleite crystals.

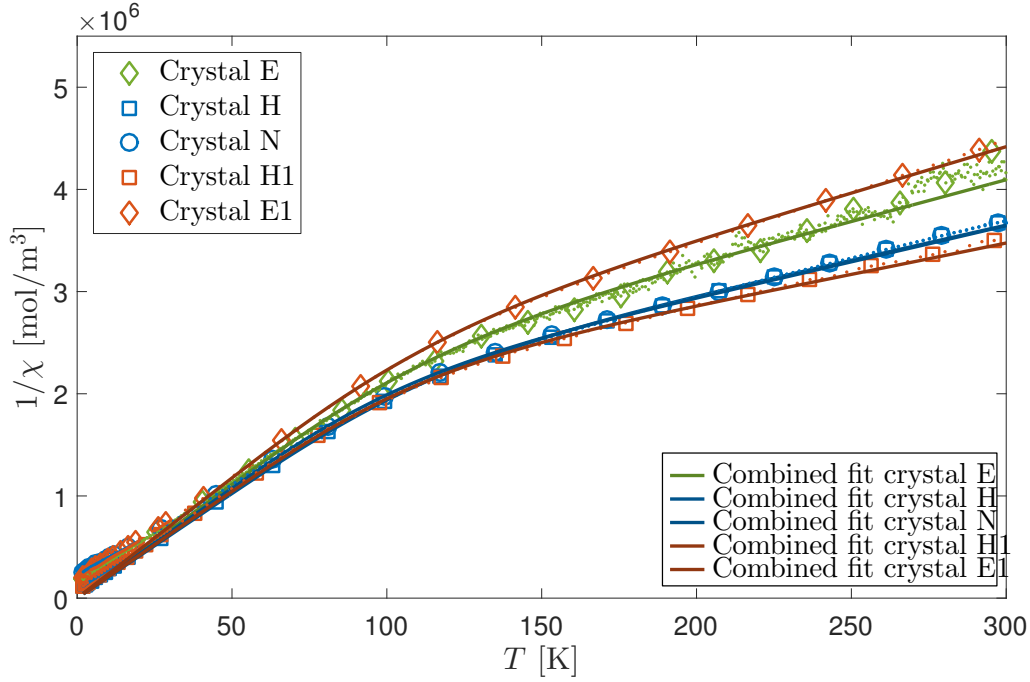
The paramagnetic contribution is found by fitting a combined triangle model and paramagnetic model according to equation (7.25), as shown in figure C.1.

After the paramagnetic contribution is found, it is subtracted from the raw data. The results of all fits are given in table C.1.

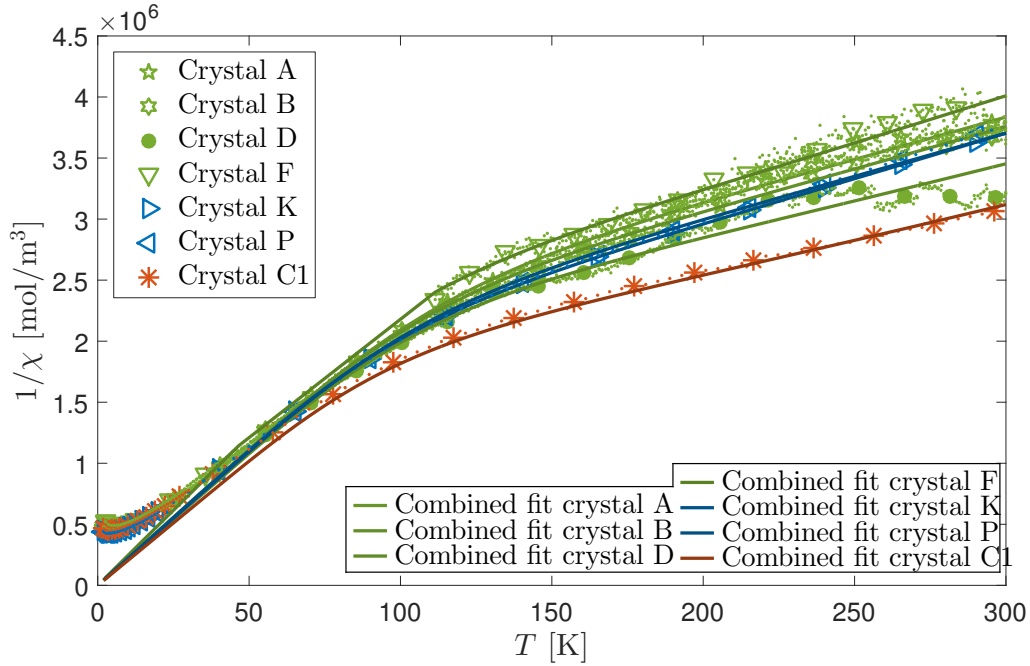
The data which has been adjusted for paramagnetic contribution is fitted with the CVT model. In figure C.2, the CVT model is fitted to each of the type 2 crystals' data where the paramagnetic contribution could be subtracted.

Type 1 susceptibility				Type 2 susceptibility			
Crystal	m [mg]	ρ	J_1 [meV]	Crystal	m [mg]	ρ	J_1 [meV]
E	403	0.102	22.7	A	355	0.038	23.2
H	226	0.065	23.2	B	424	0.037	22.1
N	245	0.054	21.1	D	605	0.000	21.9
H1	197	0.016	22.8	F	287	0.037	20.5
E1	137.1	0.124	22.5	K	263	0.062	19.9
S1	76.4	0.000	19.1	P	236	0.048	21.5
				C1	118.8	0.000	19.8
				P1	9.1	0.000	16.9
				M1	84.2	0.000	15.6

Table C.1: The crystal data and the fit parameters from fitting a combined model according to equation (7.25). The names of the crystals where the fitting of the combined paramagnetic and spin triangle model resulted in $\rho = 0$ are written in **bold**.



(a)



(b)

Figure C.1: Fitting a combined paramagnetic and triangle model. The fitting is shown for all samples that was measured at PSI and EPFL. The sample are separated into susceptibility type 1 (a) and susceptibility type 2 (b). Top legend shows the crystal names and bottom legend the fits. Parameters to the combined fits and the crystal masses are given in table C.1.

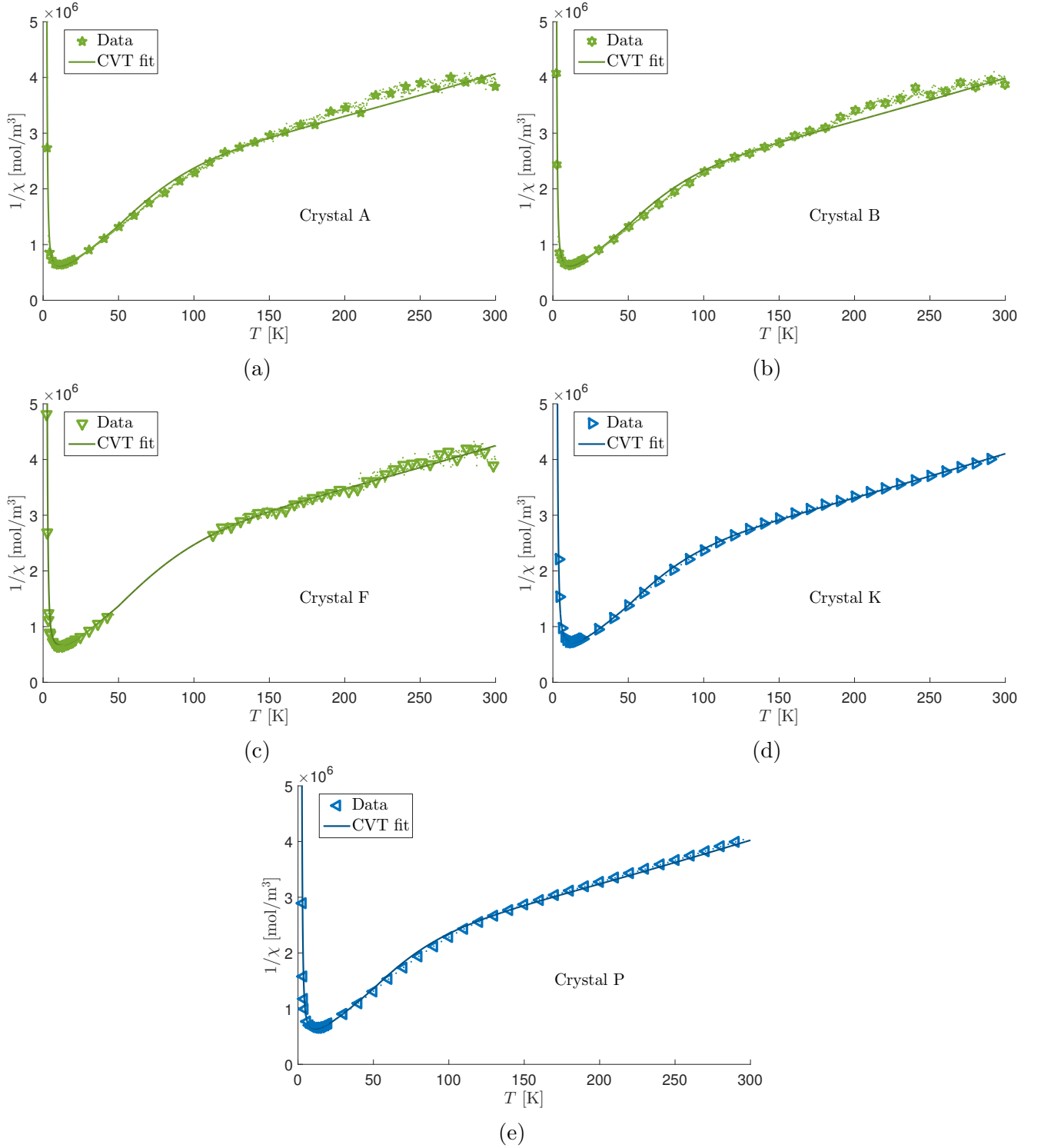


Figure C.2: Fitting the CVT model to the type 2 crystals' $1/\chi_{\text{adj}}$, found according to equation (7.26). Figure (a) to (e) show the $1/\chi_{\text{adj}}$ data from each crystal fitted with the CVT model (CVT fit). The crystal names are given in the figures. The result of the fits are given in table 7.3. The data color reflects the instrument used to measure the data, where green is PSI PPMS and blue is PSI MPMS. Only crystals where it was possible to fit the CVT model is included in this figure.

APPENDIX D

Acoustic phonon dispersion.

The acoustic phonon dispersion relation was identified to ensure that acoustic phonons did not show up when trying to identify low energy inelastic magnetic scattering.

Equation (5.34) shows that neutron scattering from phonons depend on the phonon polarization $\mathbf{e}_{d,s}$ along the phonon wave vector \mathbf{q}' . The polarization of phonons can be described by separated into two types [33].

- Longitudinal phonons have a polarization $\mathbf{e}_{d,s}$ pointing along \mathbf{q}' .
- Transverse phonons have $\mathbf{e}_{d,s}$ perpendicular to \mathbf{q}' . Generally, transverse phonons have less energy than longitudinal.

The above has a very large implication on how phonons are measured with neutrons, since the partial differential scattering cross section of phonons includes a $\mathbf{q} \cdot \mathbf{e}_{d,s}$ term. This shows that neutrons will not interact with transverse phonons when $\mathbf{q} \parallel \mathbf{q}'$, and with longitudinal phonons when $\mathbf{q} \perp \mathbf{q}'$.

To map the phonon dispersion relation in boelite, a $(h \ k \ k)$ scan was done around the $(0 \ 4 \ 4)$ r.l.u. Bragg peak at $T = 100$ K. A transverse and longitudinal acoustic phonon were identified in a scan around the Bragg peak at neutron energy transfer $\Delta E = 0.7$ meV, as seen in figure D.1a. The longitudinal phonon seems to have a much steeper dispersion relation than the transverse phonon. The longitudinal phonon is for $\Delta E = 0.7$ meV located at $|k| = 0.03$ r.l.u., and the transverse phonon is located at $|h| = 0.1$ r.l.u. The result is that the transverse phonon will have less energy at the Brillouin zone boundary $\mathbf{q}' = (0.5 \ 0 \ 0)$ than the longitudinal. It was therefore decided to follow the transverse phonon, and map its dispersion relation, to get a lower bound of the acoustic phonons dispersion relation.

The transverse phonon was located at $\Delta E = 1.0$ meV and $\Delta E = 1.5$ meV as shown in figure D.1b-c. The average scattering in RITA-II's central analyzer blades were fitted with Gaussian distribution function as shown in figure D.2. To locate the phonon at the Brillouin zone boundary, an energy scan was made at $(0.5 \ 4 \ 4)$ r.l.u., and the average scattering from all RITA-II's 9 analyzer blades was fitted with a Gaussian, as shown in figure D.3.

From the 3 scans in $(h \ k \ k)$ and the energy scan, the transverse phonon was identified in 5 different positions in the Brillouin zone. The 5 points was fitted with a simple phonon dispersion relation which fulfill equation (5.32)

$$\hbar\omega_s = \Delta E_0 \sin(q'\pi), \quad (\text{D.1})$$

which is valid for the phonon wave vector length q' in r.l.u. In this case the \mathbf{q} scans were done along the $(h \ 0 \ 0)$ direction at $(0 \ 4 \ 4)$ r.l.u. and so $q' = h$.

The fitted dispersion relation is shown in figure D.4, and showed that the transverse phonon dispersion relation's peak energy is $\hbar\omega_s(q' = 0.5) = \Delta E_0 = 2.15 \pm 0.06$ meV.

The result from this analysis of the phonon dispersion relation is that at a Brillouin zone boundary, the transverse phonon will have the least energy, with $\hbar\omega_s(q' = 0.5) = 2.15 \pm 0.06$ meV.

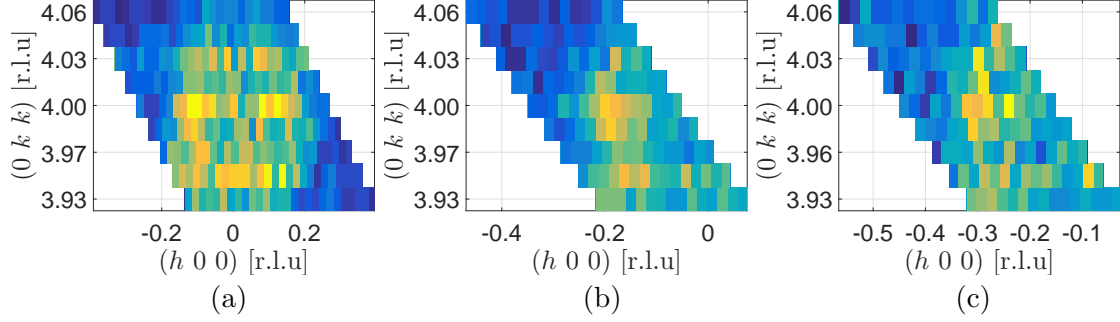


Figure D.1: Acoustic phonons at $T = 100$ K, in RITA-II $(h\ 0\ 0)$ scans around Brillouin zone center at $(h\ k\ k)=(0\ 4\ 4)$ r.l.u. for different energy transfers. RITA-II's 9 analyzer blades result in 9 lines at different values of $(0\ k\ k)$ for every $(h\ 0\ 0)$ position of the central blade 5. (a) $\Delta E = 0.7$ meV. A ring of higher intensity scattering is seen. The longitudinal phonon shows up in the $(0\ k\ k)$ direction with peak intensity around $k = \pm 0.03$ r.l.u., and the transverse phonon is seen in the $(h\ 0\ 0)$ direction with peak intensity around $h = \pm 0.1$ r.l.u. (b) Following the transverse phonon out along the $(h\ 0\ 0)$ direction as energy is increased to $\Delta E = 1.0$ meV. (c) At $\Delta E = 1.5$ meV the transverse phonon still shows up.

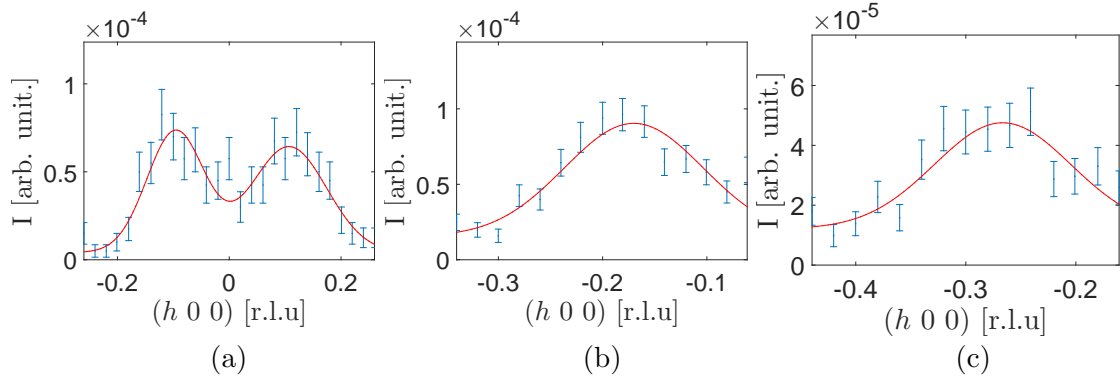


Figure D.2: Transverse acoustic phonon at $T = 100$ K in RITA-II central analyzer blades at different energies around $(0\ 4\ 4)$. The raw data are shown in figure D.1. (a) Inelastic scattering in RITA-II's analyzer blade number 5 at $\Delta E = 0.7$ meV around $(0\ 4\ 4)$ r.l.u. The data is fitted with two Gaussian functions. (b) Summed inelastic scattering from RITA-II analyzer blades number 4 to 6 at $\Delta E = 1.0$ meV around $(-0.2\ 4\ 4)$ r.l.u. The data is fitted with one Gaussian function. (c) Summed inelastic scattering from RITA-II analyzer blades number 4 to 6 at $\Delta E = 1.5$ meV around $(-0.3\ 4\ 4)$ r.l.u. The data is fitted with one Gaussian.

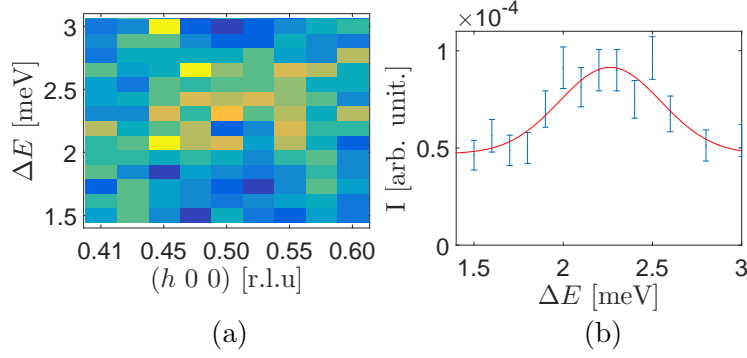


Figure D.3: Energy scan at $T = 100$ K at the Brillouin zone boundary $(0.5\ 4\ 4)$ r.l.u. RITA-II's 9 analyzer blades result in 9 values in $(h\ 0\ 0)$ (a) Raw data in false color plot. Transverse acoustic phonon is seen as higher intensity around $\Delta E = 2.3$ meV (b) Average analyzer blade intensity as function of energy fitted with a Gaussian.

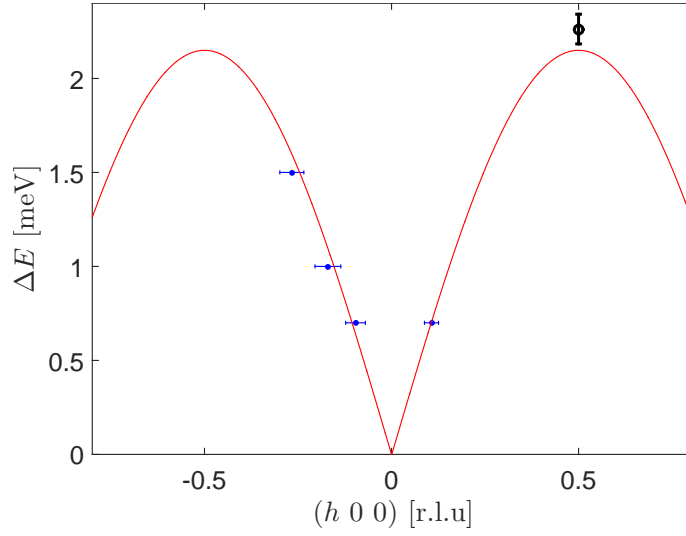


Figure D.4: Transverse acoustic phonon dispersion relation $\hbar\omega_s$ from equation (D.1) (red). The dispersion relation is fitted to the 4 identified positions of the transverse acoustic phonon from the 4 fitted Gaussians to the $(h\ 0\ 0)$ scan results in figure D.2 (blue), and the position of the phonon in the energy scan from figure D.3 (black). $\Delta E_0 = 2.15 \pm 0.06$ meV.